Ore Geology Reviews 126 (2020) 103748

Contents lists available at ScienceDirect

Ore Geology Reviews

journal homepage: www.elsevier.com/locate/oregeorev

Invited Review Article

A review of magnetite geochemistry of Chilean iron oxide-apatite (IOA) deposits and its implications for ore-forming processes

Gisella Palma[a,*], Fernando Barra[a,b], Martin Reich[a,b], Adam C. Simon[c], Rurik Romero[b]

[a] Department of Geology and Millennium Nucleus for Metal Tracing Along Subduction, FCFM, Universidad de Chile, Santiago, Plaza Ercilla 803, Chile
[b] Andean Geothermal Center of Excellence (CEGA), FCFM, Universidad de Chile, Santiago, Plaza Ercilla 803, Chile
[c] Department of Earth Sciences, University of Michigan, 1100 North University Ave, Ann Arbor, MI, USA

ARTICLE INFO

Keywords:
Magnetite textures
Magnetite geochemistry
Iron oxide-apatite deposits
IOA genetic models
Chile

ABSTRACT

Magnetite is the most important iron ore in iron oxide-apatite (IOA) deposits which represent the Cu-poor end-member of the iron oxide-copper–gold (IOCG) clan. Magnetite chemistry has been used as a petrogenetic indicator to identify the geological environment of ore formation and as a fingerprint of the source reservoir of iron. In this study, we present new textural and microanalytical EPMA and LA-ICP-MS data of magnetite from Carmen, Fresia, Mariela and El Romeral IOA deposits located in the Cretaceous Coastal Cordillera of northern Chile. We also provide a comprehensive summary and discussion of magnetite geochemistry from Andean IOAs including Los Colorados, Cerro Negro Norte, El Romeral (Chilean Iron Belt) and the Pliocene El Laco IOA deposit located in the Central Volcanic Zone of the Chilean Andes. Microtextures coupled with geochemical data were used to define and characterize the occurrence of different magnetite types. Magnetite exhibits a variety of textural features including oscillatory zoning, colloform banding, re-equilibration textures, exsolution lamellae and symplectites. The magmatic vs. hydrothermal origin of the different magnetite types and the evolution of IOA deposits can be assessed using diagrams based on compatible trace elements. However, magnetite is very susceptible to hydrothermal alteration and to both textural and compositional re-equilibration during magmatic and superimposed hydrothermal events. Based on the data presented here, we conclude that V and Ga are possibly the most reliable compatible elements in magnetite to trace ore-forming processes in the Andean IOA deposits. Magnetite chemistry reveals different conditions/events of formation for each IOA deposit ranging from high-temperature, low-oxygen fugacity (fO_2), purely magmatic (> 600 °C) conditions; to lower temperature and higher fO_2 magmatic-hydrothermal (300–600 °C) to low-temperature hydrothermal (< 200–300 °C) conditions. Specifically, a continuous transition from high-temperature, low- fO_2 conditions in the deepest portions of the deposits to low-temperature, relatively higher fO_2 conditions towards surface are described for magnetite from El Laco. The new and compiled magnetite data from IOA deposits from the Chilean Iron Belt and El Laco are consistent with a transition from magmatic to hydrothermal conditions. The *flotation model* plausibly explains such features, which result from the crystallization of magnetite microlites from a silicate melt, nucleation and coalescence of aqueous fluid bubbles on magnetite surfaces, followed by ascent of a fluid-magnetite suspension along reactivated transtensional faults or through fissures formed during the collapse of the volcanic structure (El Laco). The decompression of the coalesced fluid-magnetite aggregates during ascent promotes the continued growth of magnetite microlites from the Fe-rich magmatic-hydrothermal fluid. As with any general genetic model, the *flotation model* allows variation and the definition of different styles or subtypes of IOA mineralization. The deeper, intrusive-like Los Colorados deposit shows contrasting features when compared with the Cerro Negro Norte hydrothermal type, the pegmatitic apatite-rich deposits of Carmen, Fresia and Mariela, and the shallow, subaerial deposits of El Laco. These apparent differences depend fundamentally on the depth of formation, the presence of structures and faults that trigger decompression, the composition of the host rocks, and the source and flux rate of hydrothermal fluids.

* Corresponding author.
E-mail address: gipalma@ing.uchile.cl (G. Palma).

https://doi.org/10.1016/j.oregeorev.2020.103748
Received 15 November 2019; Received in revised form 30 July 2020; Accepted 27 August 2020
Available online 09 September 2020

1. Introduction

Magnetite (Fe_3O_4) is a common accessory mineral in igneous, metamorphic and sedimentary rocks and can form under a wide range of temperature and pressure conditions. It can also become concentrated in large quantities to form ore deposits such as banded iron formations (e.g., Angerer et al., 2012; Araújo and Lobato, 2019), magmatic Fe-Ti-V oxide (e.g., Zhou et al., 2005), iron skarns (e.g., Nadoll et al., 2014, 2015), iron oxide-copper–gold (IOCG) and Kiruna-type iron oxide-apatite (IOA) deposits (e.g., Williams et al., 2005).

Iron oxide-apatite deposits represent the Cu-poor end-member of the IOCG clan (Sillitoe, 2003) and are an important source of Fe. Iron oxide-apatite mineralization is dominated by low-Ti magnetite, which can be accompanied by variable amounts (1–50% modal) of apatite, actinolite, pyroxene, epidote and sulfides (Williams et al., 2005). On the other hand, IOCG deposits are mined for their Cu content, but in some cases Au, U, REE, P, Co, Bi and Nb are relevant by-products (Hitzman et al., 1992; Sillitoe, 2003; Williams et al., 2005; Groves et al., 2010; Barton, 2014). IOCG mineralization is characterized by Cu-Fe sulfides (chalcopyrite and minor bornite), Cu oxides and abundant iron oxides (magnetite and/or specular hematite). Hydrothermal alteration is represented by sodic-calcic (albite, actinolite, epidote) and potassic (biotite, orthoclase) assemblages with minor chlorite, sericite and late calcite. Regardless of the high concentration of iron oxides in IOCGs, they are rarely mined for Fe.

Both IOCG and IOA deposits occur globally with reported ages ranging from Archean (e.g., Carajás Province, Brazil; de Melo et al., 2017), early Proterozoic (e.g., Kiruna district, Sweden and Olympic Dam district, Australia; Westhues et al., 2017a, 2017b; Apukhtina et al., 2017), middle Proterozoic (e.g., Pea Ridge and Pilot Knob deposits, USA, and Cloncurry district, Australia; Rusk et al., 2010; Day et al., 2016; Childress et al., 2016), Cretaceous (e.g., Los Colorados, El Romeral, Candelaria and Mantoverde, Chile; Benavides et al., 2007; Rieger et al., 2010, 2012; Knipping et al., 2015a, 2015b; Rojas et al., 2018a) and Pliocene (e.g., El Laco, Chile; Maksaev et al., 1988; Nyström and Henríquez, 1994; Naranjo et al., 2010).

In Chile, most of the IOCG and IOA deposits occur spatially and temporally associated with one another in the Jurassic − Early Cretaceous Chilean Iron Belt (CIB) within the Coastal Cordillera of northern Chile between latitudes 25° and 31°S (Fig. 1). These deposits occur closely associated with coeval Mesozoic intrusions and are structurally controlled by the arc-parallel Atacama Fault System (AFS) (Sillitoe, 2003; Williams et al., 2005). As the youngest-known IOCG − IOA province in the world, mostly unaffected by metamorphism and deformation (Sillitoe, 2003), the CIB is an ideal area to study the processes involved in the formation of IOA and IOCG deposits and to refine the current genetic model. Noteworthy, the Pliocene El Laco Volcanic Complex (ELVC), located further north (23°48′S) in the high Andes, hosts the youngest, least altered, and best preserved IOA deposit discovered to date (Naranjo et al., 2010; Fig. 1). Within an area of ~ 35 km^2, six magnetite ore bodies have been described at El Laco (i.e., Laco Norte, Laco Sur, San Vicente Alto, Rodados Negros, Cristales Grandes and San Vicente Bajo). These ore bodies display remarkable volcanic and subvolcanic features that have fueled the controversy regarding a magmatic (immiscibility model) or metasomatic origin for IOA deposits (Frutos and Oyarzún, 1975; Nyström and Henríquez, 1994; Sillitoe and Burrows, 2002; Naranjo et al., 2010; Tornos et al., 2016; Velasco et al., 2016; Ovalle et al., 2018).

It is well known that IOCG deposits are mostly formed by hydrothermal processes (Sillitoe, 2003; Williams et al., 2005; Mumin et al, 2007; Groves et al., 2010; Barton, 2014). However, the origin of IOA deposits remains controversial and, historically, two contrasting "classic" hypotheses have been proposed. The first hypothesis comprises a purely magmatic origin involving the separation of an immiscible Fe-P-rich melt from a silicate melt with the subsequent intrusion and crystallization of an Fe-rich ore body at upper crustal levels (e.g., Nyström and Henríquez, 1994; Naslund et al., 2002; Chen et al., 2010; Velasco et al., 2016). The second hypothesis involves a purely hydrothermal origin where the magnetite ore is formed by metasomatic replacement of host rocks by Fe-rich fluids sourced from magmatic or non-magmatic sources (e.g., Rhodes and Oreskes, 1995, 1999; Sillitoe and Burrows, 2002; Barton and Johnson, 1996, 2004; Pollard, 2006; Dare et al, 2015; Westhues et al., 2016, 2017b; Westhues et al, 2017a). Most of the current debate regarding the origin of IOA deposits has been centered on El Laco, where some researchers have argued that the magnetite ore bodies preserve purely igneous/volcanic features, such as pahoehoe- and aa-like lava flows, different degrees of vesicularity, contorted flow layering, spherulitic and dentritic magnetite, and vertical structures interpreted as gas escape tubes (Nyström and Henríquez, 1994; Naslund, et al., 2002). However, others have interpreted these textures as relicts of the andesite lava flows that have been replaced by hydrothermal iron oxides, based on magnetite veins and breccias, and hydrothermal alteration assemblages observed around the magnetite bodies (Rhodes et al., 1999; Sillitoe and Burrows, 2002).

Over the past few years, and in light of a renewed interest in magnetite geochemistry studies, a novel genetic model was proposed by Knipping et al. (2015a) and Knipping et al. (2015b) to explain the formation of IOA deposits. By using a combination of field observations, trace element geochemistry and Fe and O stable isotopes composition in magnetite grains from Los Colorados, those authors propose that IOA deposits formed by a combination of igneous and magmatic-hydrothermal processes. In their *flotation model*, microlites of magnetite crystallized from a silicate melt triggering bubble nucleation, forming a magnetite-fluid suspension that transported magnetite to shallow depths through pre-existing fault structures that are reactivated by crustal extension. This new model not only reconciles the two opposing genetic hypotheses (liquid immiscibility vs. metasomatic replacement), but also provides a plausible explanation for the formation of spatially associated IOCG deposits as part of the same evolving system (Reich et al., 2016; Barra et al., 2017; Simon et al., 2018). A genetic connection between IOA and IOCG deposits of the Coastal Cordillera of northern Chile has been previously proposed, where IOA (sulfide-poor) deposits may represent the roots or deep portion of IOCG (sulfide-rich) systems (Espinoza et al., 1996; Sillitoe, 2003).

The current discussion about the genesis of IOA deposits is based on, among other proxies, the major and trace element geochemistry of magnetite, which is the modally dominant mineral in all IOA deposits. Both electron microprobe analysis (EMPA) and laser ablation inductively coupled plasma mass spectrometry (LA-ICP-MS) have been used to measure the chemical composition of major and trace elements in magnetite, respectively. While EMPA allows for a low-micron size beam (< 5 μm) to analyze a limited number of elements, e.g., Mg, Al, Ca, Ti, V, Cr and Mn at detection limits of tens to hundreds of ppm (e.g., Dupuis and Beaudoin, 2011), LA-ICP-MS allows in-situ measurements on 20–50 μm spots of a large number of trace elements (> 40) at ppm to sub-ppm levels. These analytical advances have resulted in a growing interest in the study of magnetite as a petrogenetic indicator and as tool to identify past geological environments of ore formation or as a fingerprint of mineral deposit types (Dupuis and Beaudoin, 2011; Dare et al., 2012, 2014; Nadoll et al., 2012, 2014; Huang et al., 2018, 2019; Huang and Beaudoin, 2019). In particular, Knipping et al. (2015a) and Knipping et al. (2015b) documented distinct chemical zoning in magnetite grains from Los Colorados IOA deposit, where cores are enriched in Ti, Al, Mn and Mg indicating crystallization from a silicate melt. In contrast, magnetite rims show a pronounced depletion in these elements, consistent with magnetite grown from a Fe-rich magmatic-hydrothermal aqueous fluid (Knipping et al., 2015b).

After Knipping et al. (2015a) and Knipping et al. (2015b), several geochemical and textural studies have been carried out on magnetite and other mineral phases (pyrite, actinolite, apatite) in the Andean IOCG and IOA deposits including: El Romeral (Rojas et al., 2018a, 2018b); Los Colorados (Bilenker et al., 2016; Reich et al., 2016;

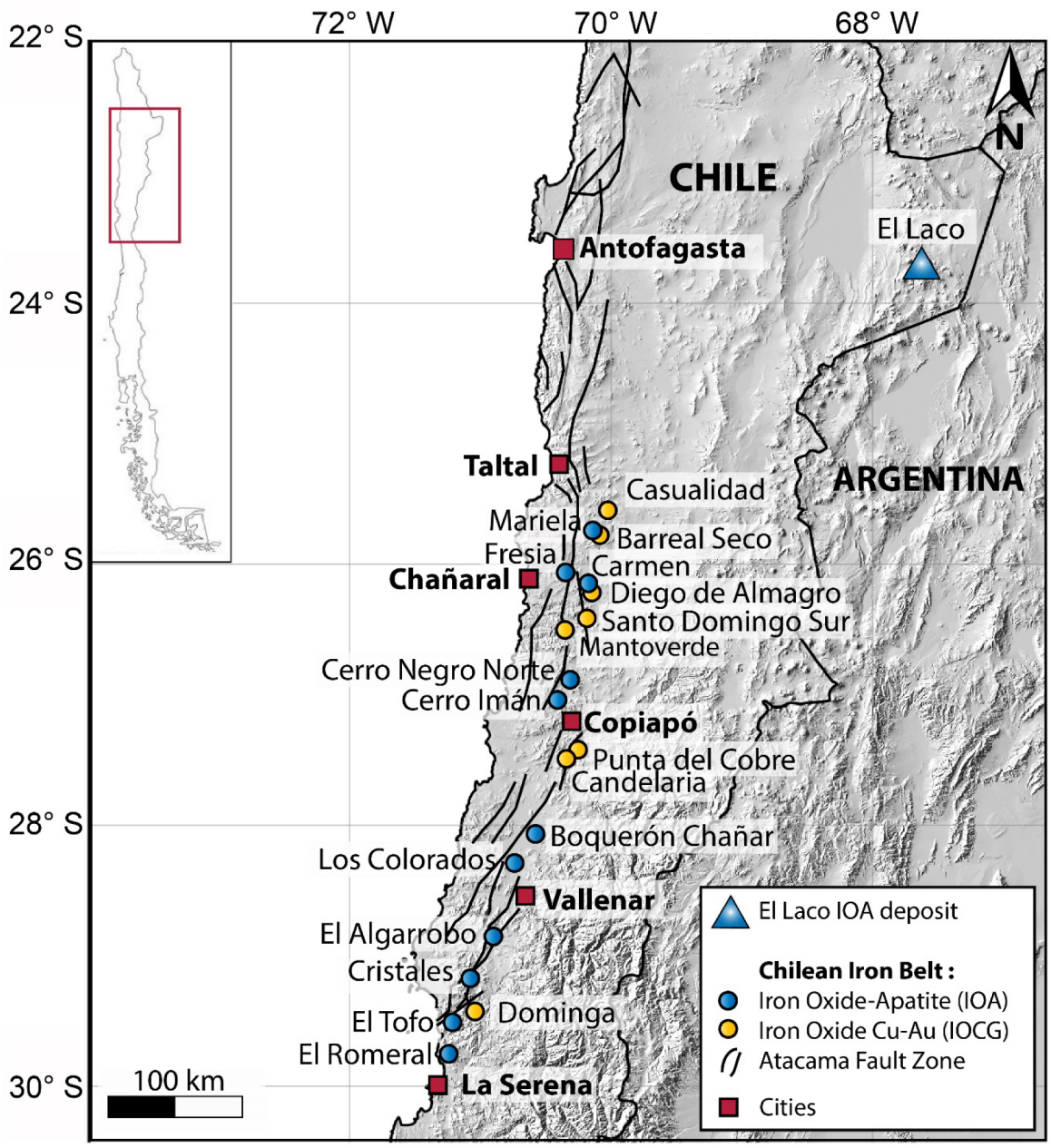

Fig. 1. Map showing the location of main IOCG and IOA deposits in the Jurassic–Early Cretaceous Central Andean IOCG Province of the Coastal Cordillera (25-31°S) and El Laco IOA deposit (23°48′S) in the high Andes of northern Chile. Modified after Barra et al. (2017).

Deditius et al., 2018; La Cruz et al., 2019; Knipping et al., 2019a); El Laco (Ovalle et al., 2018; La Cruz et al., 2019, 2020); Cerro Negro Norte (Salazar et al., 2020); Carmen, Fresia and Mariela (Palma et al., 2019); Candelaria (Rodriguez-Mustafa et al., 2020); Mantoverde (Childress et al., 2020). The chemical composition of magnetite grains from Cerro Negro Norte, El Romeral and El Laco deposits reflect their formation conditions, revealing systems that evolved from high-temperature purely igneous/magmatic conditions at depth to lower temperature magmatic-hydrothermal conditions at shallow depths (Ovalle et al., 2018; Rojas et al., 2018b; Salazar et al., 2020; La Cruz et al., 2020). The data presented in such studies have been described as consistent with the *flotation model* to explain the origin of Andean IOA deposits.

In this contribution we present a review of the extensive magnetite chemical data gathered during these last few years on Andean IOA and IOCG deposits. In addition, we present and discuss new micro-textural, EPMA and LA-ICP-MS data for magnetite from the Carmen, Fresia, Mariela and El Romeral IOA deposits. The trace element composition of magnetite, geochemical discrimination diagrams (e.g., Dupuis and Beaudoin, 2011; Nadoll et al., 2014) and Principal Component Analysis (PCA) are used here to fingerprint the texturally different magnetite types observed in each deposit and provide new constraints on the formation of these deposits. We also demonstrate how magnetite compositional data should be closely inspected and complemented with micro-textural observations to avoid misinterpretations. Finally, we propose a mechanism of formation for the apatite-rich (~20–50% modal), pegmatitic IOA subtype of Carmen, Fresia and Mariela.

2. Geological setting

2.1. The Chilean Iron Belt, Coastal Cordillera of northern Chile (25-31°S)

In the Chilean Iron Belt (CIB), IOCG and IOA deposits formed during

Table 1
Main geological features of studied IOA deposits and most important IOCG deposits.

Deposit	Tonnage	Host rock (Formation)	Related intrusive rocks	Main structures	Age (technique)	Mineralization style	Alteration	Mineralization	Data source
Iron oxide-apatite (IOA) deposits of the Chilean Iron Belt (25-31°S)									
Carmen	NR	Andesitic lava (La Negra Formation)	Diorite dike and quartz diorite pluton	EW and NE faults intersection (related to extensional strike-slip duplexes configuration)	131.0 ± 1.0 Ma (U-Pb on apatite); 130.0 ± 1.7 Ma (Lu-Hf on apatite)	Massive, dikes, veins, breccia	Act, Cl-ap, Chl, Qz, Ser, clays, Gyp	Mgt ± Hmt; Py-Cpy	Treloar and Colley (1993), Treloar and Colley (1996), Bonson et al (1997), Gelcich et al. (2005), Zhang et al. (2017), Palma et al. (2019)
Fresia	NR	Andesitic lava (Los Cerros Florida Formation)	Microgabbro to microdiorite dikes	Fault intersection zone trending at 80° and 65° (related to extensional strike-slip duplexes configuration)	132.8 ± 5.3 Ma (Lu-Hf apatite)	Massive, dikes, veins, breccia	Ep, Chl, Carb, Qz, Cl-ap, clays	Mgt ± Hmt	Treloar and Colley (1993), Treloar and Colley (1996), Bonson et al (1997), Zhang et al. (2017), Palma et al. (2019)
Mariela	NR	Granodiorite (Aeropuerto Formation)	Diorite	Breccia pipe developed in a NNE-orientation rhomboid bounded to the east by a NS-fault (related to extensional strike-slip duplexes configuration)	117.3 ± 0.4 Ma (Lu-Hf apatite)	Breccia pipe, tabular	Chl, Ep, Ttn, Gyp, Qz, Goe	Mgt ± Hmt; Py-Cpy; Chry ± At	Río Tinto internal report (2001), Zhang et al. (2017), Palma et al. (2019)
El Romeral	451 Mt@ 28.3% Fe	Andesite porphyry, metasedimentary rocks (La Liga Formation).	Diorite body, granodiorite pluton	Romeral fault (NS); NNE fault	129.0 ± 0.9 Ma (U-Pb on zircon); ~128 Ma ($^{40}Ar/^{39}Ar$ on actinolite)	Massive, veins, disseminated	Act, Ap, Bio, Chl	Mgt; Py-Cpy	Bookstrom (1977) , Emparan and Pineda (2005) , Rojas et al. (2018a,b)
Los Colorados	491 Mt @ 36.5% Fe	Basaltic andesite, andesite lava flows and volcanoclastic rocks (Punta del Cobre Formation)	Diorite-microdiorite pluton	N10-15E; NS-N10 W faults	110–115 Ma (radiometric K-Ar)	Massive, tabular, dikes, breccias	Act, Ap, Chl, K-feld, Turm, Ser,clays	Mgt ± Hmt; Py-Cpy	Pichon (1981) , Oyarzún and Frutos (1984), Knipping et al. (2015a) and Knipping et al. (2015b), Reich et al (2016), Pincheira et al., (1990)
Cerro Negro Norte	657.3 Mt@ 29.7% Fe	Volcanic breccias and andesite lavas (Bandurrias Formation)	Diorite and quartz-diorite stocks; monzodiorite to granodiorite dikes	NNE and EW fault	130.5 ± 0.7 Ma (U-Pb on zircon)	Massive, tabular to lobular; breccias, stockworks, disseminated	Act, Scap, Ap, Alb, Qz, Ttn, Ep, Bio, Carb, Tourm, Ser, Jar, Goe	Mgt ± Hem; Py-Cpy ± Bn; minor Cu-ox	Vivallo et al. (1995), Raab (2001), CAP Minería Annual Report (2016), Salazar et al. (2020)
El Laco IOA deposit, Chilean Altiplano (23° S)									
El Laco	733.9 Mt@ 49.2% Fe	Andesitic to dacitic lava flows and pyroclastic rocks (El Laco Volcanic Complex))	NR	NW and EW faults (related to the collapse of the volcanic building)	Between 5.3 ± 1.9 and 1.6 ± 0.5 Ma (whole-rock K-Ar); 2.1 ± 0.1 Ma (fission track apatite)	Lava-like flows (Laco Norte, Laco Sur and San Vicente Alto), tabular (Rodados Negros and Cristales Grandes) and dome-shaped bodies (San Vicente Bajo)	At depth: Scap, Di; steam-heated zones: Trd,Crs, Alu, Jar	Mgt ± Hmt	Maksaev et al. (1988), Nyström and Henríquez. (1994), Naranjo et al. (2010), CAP Minería Annual Report (2016)
Iron oxide Cu-Au (IOCG) deposits of the Chilean Iron Belt (25-31°S)									
Candelaria	470 Mt @ 0.95% Cu,	Volcanic, volcanoclastic and sedimentary units	Diorite to quartz monzonite bodies, dikes and sills	NE-trending antiform (Tierra Amarilla anticlinorium); El Bronce	115.2 ± 0.6 Ma (Re-Os molybdenite)	Veins, breccias, stratabound bodies	Mgt, Act, Bio, K-feld, Qz	Cpy-Py-Po ± Sp-Mo; Mgt ± Mush; poorly	Marschik et al. (2000), Marschik and Fontboté (2001),

(*continued on next page*)

Table 1 (*continued*)

Deposit	Tonnage	Host rock (Formation)	Related intrusive rocks	Main structures	Age (technique)	Mineralization style	Alteration	Mineralization	Data source
	0.22 g/t Au, 3.1 g/t Ag	(Punta del Cobre Formation)		SE-verging fold-thrust system; N-NW to NW sinistral transcurrent faults; N-, E-NE to NE-faults		(replacement-type), disseminated		developed Cu oxides, supergene enrichment zone	Mathur et al. (2002), del Real et al. (2018)
Mantoverde	42.7 Mt @ 0.58% Cu (oxides); 440 Mt @0.56% Cu (sulfides), 0.12 g/t Au	Basaltic andesite, andesite flows and volcanoclastic rocks (La Negra Formation)	Granodiorite, diorite	Mantoverde fault: N15-20 W/40-50E	128.9 ± 0.3 Ma (U-Pb zircon)	Veins, stockworks, breccias	K-feld, Bio, Tourm, Qz, Chl, Ser, Scap, Ep, Carb	Py-Cpy ± gold; Cu ox; Mgt-Hmt	Gelcich et al. (2002), Benavides et al. (2007), Rieger et al. (2010), Rieger et al. (2012)

Notes:
Abbreviations: NR = not reported; Act = actinolite; Alb = albite;Alu = alunite; Ap = apatite; At = atacamite; Bio = biotite; Bn = bornite; Carb = carbonate; Chry = chrysocolla; Cpy = chalcopyrite; Chl = chlorite; Crs = cristobalite; Di = diopside; Ep = epidote; Goe = goethite; Gyp = gypsum; Hmt = hematite;Jar = jarosite; K-feld = K-feldspar; Mgt = magnetite ; Mo = molybdenite; Mush = mushketovite; Po = pyrrhotite; Py = pyrite Qz = quartz; Scap = scapolite; Sp = sphalerite; Ser = sericite; Tourm = tourmaline; Ttn = titanite; Trd = trydimite.

the Late Jurassic to Early Cretaceous under an extensional tectonic regime (Mariana-type subduction) in response to subduction rollback at the retreating convergent margin (Mpodozis and Ramos, 1989; Grocott and Taylor, 2002). The extensional conditions during this period resulted in the formation of a subsiding trench-parallel magmatic arc and a sedimentary marine back-arc basin (Mpodozis and Ramos, 1989; Scheuber et al., 1994; Brown, 1995; Charrier et al., 2007; Ramos, 2010). The magmatic arc was dominated by tholeiitic basaltic magmas, gabbros and mafic dikes associated with calc-alkaline andesites and basaltic andesite flows (Mpodozis and Ramos, 1989; Scheuber et al., 1994; Oliveros et al., 2006). The plutonic complexes, emplaced into broadly contemporaneous arc and intra arc-volcanic products, comprise hornblende-biotite gabbros, diorites, tonalites, granodiorites and minor granites (Dallmeyer et al., 1996).

The dominant structural feature of the CIB is the Atacama Fault System (AFS), a > 1,000 km long, trench-parallel, strike-slip fault zone (Fig. 1) that resulted from the synchronous opening of the South Atlantic Ocean basin and oblique subduction beneath western South America (Uyeda and Kanamori, 1979; Scheuber and Andriessen, 1990; Brown et al., 1993; Scheuber and González, 1999). This fault system consists of a set of branches marked by prior ductile shear zones and later brittle faults with NNW-, N- and NNE-orientations (Brown, 1995; Dallmeyer et al., 1996; Scheuber and González, 1999; Grocott and Taylor, 2002). The AFS was characterized by a sinistral movement during the Jurassic to Early Cretaceous, followed by dextral shearing during the Late Cretaceous and final vertical displacements as a result of changes in the plate configuration and in the convergence vector of the subducting plate (Scheuber and Andriessen, 1990; Scheuber and González, 1999).

The Central Andean IOCG-IOA province of northern Chile and southern Peru formed over a period of ca. 65 Ma (Chen et al., 2013). The IOCG and IOA ore systems are apparently diachronous and both appear to have accompanied the eastward migration of arc magmatism (Sillitoe, 2003). Although IOCG mineralization began to develop during the Middle Jurassic (165–155 Ma), it was during the mid-Cretaceous (ca. 130–100 Ma) that most IOA deposits were formed (Oyarzún et al., 2003; Chen et al., 2013; Barra et al., 2017). Iron oxide-apatite deposits are usually hosted by mafic-to-intermediate sub-aerial volcanic units (e.g., La Negra Formation: Middle to Late Jurassic or Punta del Cobre Formation: Late Jurassic to Early Cretaceous) or broadly contemporaneous gabbro to granodiorite intrusions (Sillitoe, 2003). Most of the IOCG and IOA deposits of the Coastal Cordillera of northern Chile occur in the vicinity of the AFS usually related to second order faults (Sillitoe, 2003; Cembrano et al., 2005).

The Andean IOA deposits are characterized by the occurrence of massive magnetite ore bodies, veins, lens-like bodies, mantos and breccias with actinolite, minor apatite (usually < 1% modal) and traces of sulfides such as pyrite and chalcopyrite. About 50 IOA deposits, including seven large deposits (> 100 Mt high grade Fe-ore) occur within the Coastal Cordillera between 25 and 31°S (Nyström and Henríquez, 1994). Some deposits were mined in the past for iron (e.g., El Algarrobo, El Tofo, Carmen) or phosphates (Mariela) and only a few are currently under production (Los Colorados and Cerro Negro Norte). Some small IOA deposits including Carmen, Fresia and Mariela display pegmatitic, comb-like and breccia-like textures with ~20–40% modal apatite, pointing to high volatile/melt conditions in the apical parts of IOA deposits (Treloar and Colley, 1996; Palma et al., 2019). In some areas of the Carmen and Fresia deposits, large apatite crystals (up to 50 cm long) have crystallized perpendicular to the magnetite vein walls (Treloar and Colley, 1993, 1996; Palma et al., 2019). In the Mariela IOA deposit, apatite with minor actinolite and magnetite occurs as a breccia matrix around chlorite-epidote altered intrusive fragments (Palma et al., 2019). In the central and eastern part of Mariela, pegmatitic apatite and actinolite crystals can reach up to 3 m long (Río Tinto internal report, 2001).

Iron oxide-copper–gold (IOCG) mineralization comprises specular

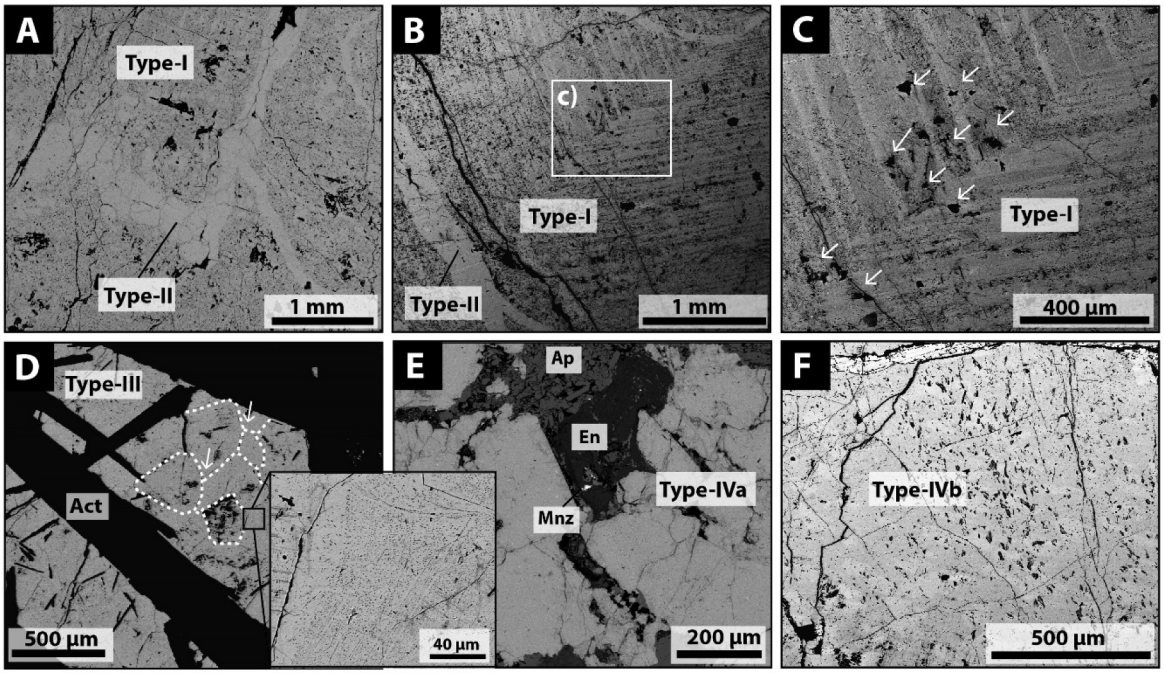

Fig. 2. Back-scattered electron images of magnetite types from the Carmen deposit. (A) Inclusion-rich Type-I magnetite crosscut by pristine, inclusion-free Type-II magnetite veinlets; (B) Type-I magnetite showing oscillatory zoning with alternating dark and light bands crosscut by Type-II magnetite veinlet; (C) Detail of oscillatory zoning in Type-I magnetite. The white arrows indicate mineral inclusions that are distributed preferentially within the dark bands; (D) Type-III magnetite intergrown with actinolite (Act) crystals. Early magnetite was recrystallized to fine-grained aggregates of Type-III magnetite in a mosaic texture with triple junctions (white dotted lines and arrows). The inset shows a magnetite grain with numerous nano- to micron-sized inclusions; (E) Inclusion-poor Type-IVa magnetite veinlet associated with Cl-rich apatite (Ap), monazite (Mnz) and enstatite (En). The veinlet crosscuts Type-III magnetite; (F) Type-IVb porous magnetite veinlet.

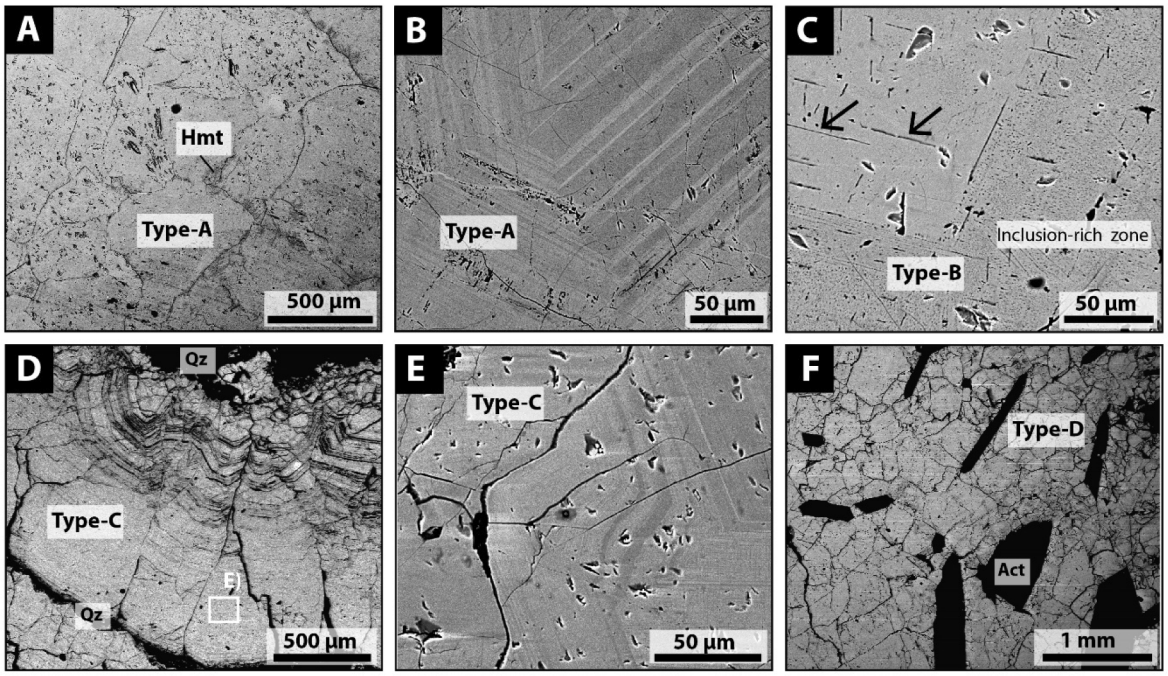

Fig 3. Back-scattered electron images of magnetite types from the Fresia deposit. (A) Recrystallized grains of Type-A magnetite. Note the presence of pores in some grains and the hematite (Hmt) replacement (BSE-dark) along rims; (B) Well-developed oscillatory zoning in Type-A magnetite. Note the absence of mineral inclusions and the presence of pores in some areas; (C) Type-B magnetite that exhibits exsolution lamellae of a Ti-bearing phase (black arrows) and numerous nano-inclusions oriented along magnetite crystallographic planes; (D) Crustiform-colloform banding in Type-C magnetite with quartz (Qz); (E) Detail from (D) showing the oscillatory zoning texture in Type-C porous magnetite; (F) Porous, recrystallized Type-D magnetite intergrown with large actinolite (Act) crystals in veinlet that crosscuts the altered host rock at the margin of the Fresia deposit.

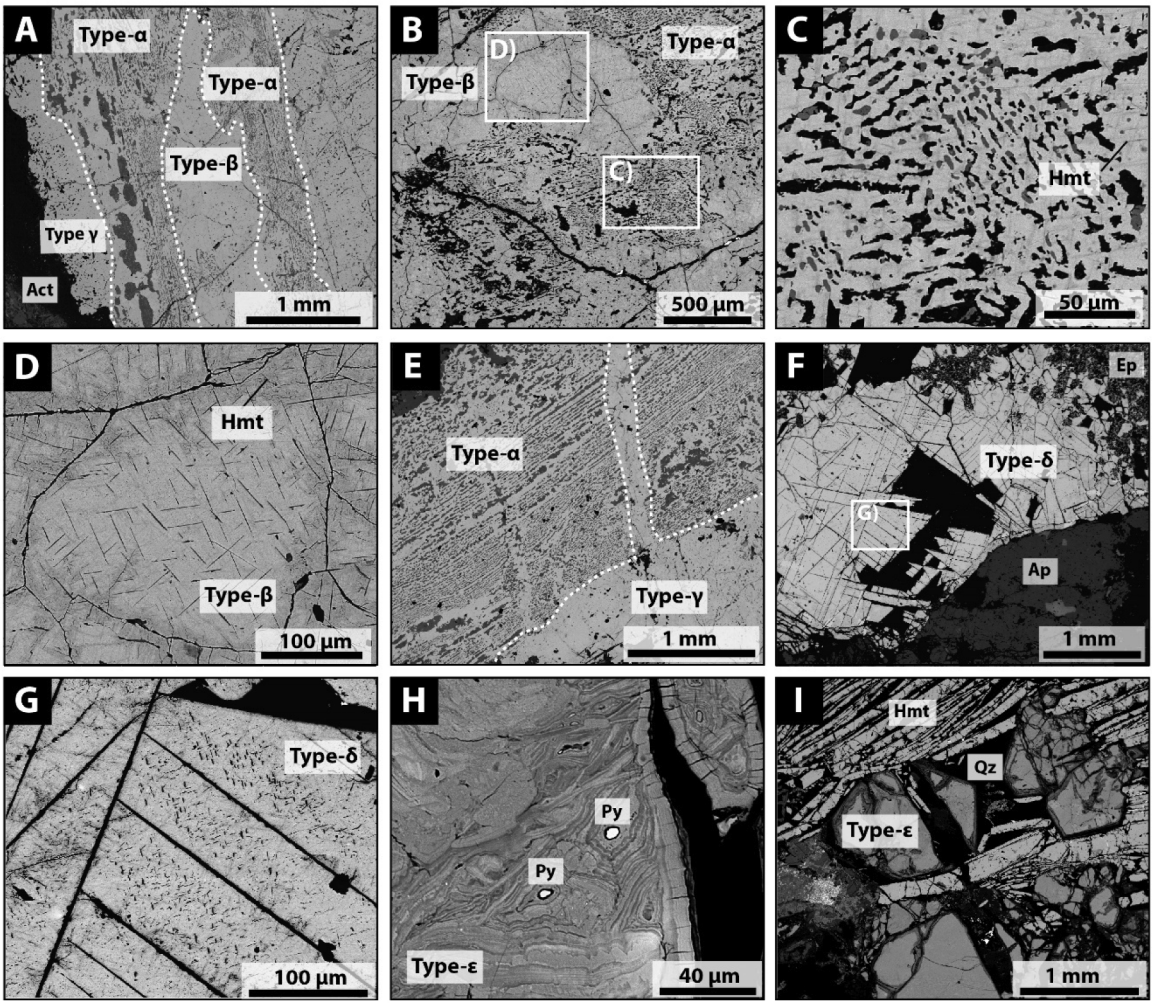

Fig. 4. Back-scattered electron images of magnetite types from the Mariela deposit. (A) General view of Type-α, -β and -γ magnetite in contact with actinolite (Act); (B) Type-α magnetite with symplectite texture and fractured Type-β magnetite. The white rectangles indicate the areas corresponding to Figures C and D. (C) Symplectite texture composed of interstitial magnetite and vermicular rutile (BSE-light grey) altered to titanite (BSE-black). Note that magnetite is replaced by hematite (Hmt) along crystallographic planes; (D) Type-β magnetite exhibiting ulvöspinel/ilmenite exsolution lamellae. Note that magnetite is replaced by hematite (Hmt) along fractures; (E) Type-α magnetite crosscut by a later veinlet of Type-γ magnetite; (F) Type-δ magnetite veinlet which displays a well-defined cubic cleavage associate with epidote (Ep) and Cl-rich apatite (Ap). The white rectangle indicates the area of Figure G; (G) Type-δ magnetite showing abundant ilmenite exsolution lamellae; (H) Type-ε magnetite grain exhibiting a fluidal texture with bands of different shades of gray, which represent variable Fe and Si contents. Note the small pyrite grains (Py) hosted within Type-ε magnetite. (I) Type-ε Si-rich magnetite intergrown with specular hematite (Hmt) and quartz (Qz).

hematite or magnetite massive ore bodies, veins, mantos, stockworks and breccia, with abundant chalcopyrite, pyrite and lesser bornite. Iron mineralization occurs accompanied by hydrothermal albite, K-feldspar, chlorite, sericite, epidote, carbonates, quartz, actinolite and minor scapolite (Hitzman et al., 1992; Sillitoe, 2003; Williams et al., 2005; Groves et al., 2010). The largest IOCG deposits in Chile are the Mantoverde (hematite rich-type) and Candelaria (magnetite rich-type) deposits, both with over 400 Mt of Cu with a 1% ore grade (Marschik et al., 2000; Marschick and Fontboté, 2001; Benavides et al., 2007; Rieger et al., 2010, 2012; del Real et al., 2018) (Fig. 1; Table 1).

The main geological features of the IOA deposits discussed in this study including Carmen, Fresia, Mariela, El Romeral, Los Colorados, Cerro Negro Norte and El Laco, and both Candelaria and Mantoverde IOCG deposits, are summarized in Table 1.

2.2. El Laco IOA deposit, Chilean Altiplano

The El Laco Volcanic Complex (ELVC) is located at elevations of 4,600–5,200 m above sea level in the Plio-Pleistocene volcanic arc of the Central Volcanic Zone of the Andes, northern Chile (Fig. 1). This volcanic complex comprises a cluster of andesitic to dacitic volcanic structures with NW-trending fissural emission centers and secondary craters associated with ring-shaped structures around Pico Laco (Naranjo et al., 2010). Within the ELVC the magnetite ore bodies occur interbedded between lava flows and pyroclastic rocks, spatially associated with the pre-existing subvertical annular collapse structures and with secondary craters (Frutos and Oyarzún, 1975; Naranjo et al., 2010). The El Laco IOA deposit is composed of six massive magnetite ore bodies including the lava-like flows of Laco Norte, Laco Sur and San Vicente Alto; the N-W-trending tabular bodies of Rodados Negros and Cristales Grandes; and the dome-shaped bodies of San Vicente Bajo (Nyström and Henríquez, 1994; Naranjo et al., 2010; Ovalle et al., 2018; Table 1). The magnetite ore bodies are mainly composed of magnetite (~98% modal)—with minor hematite-goethite formed by the supergene alteration of magnetite outcrops—apatite, diopside, scapolite, apatite, REE-rich and iron phosphates (Naranjo et al., 2010; Ovalle et al., 2018). Total estimated resources are 733.9 Mt with an average ore grade of 49.2% Fe (CAP Minería Annual Report, 2016),

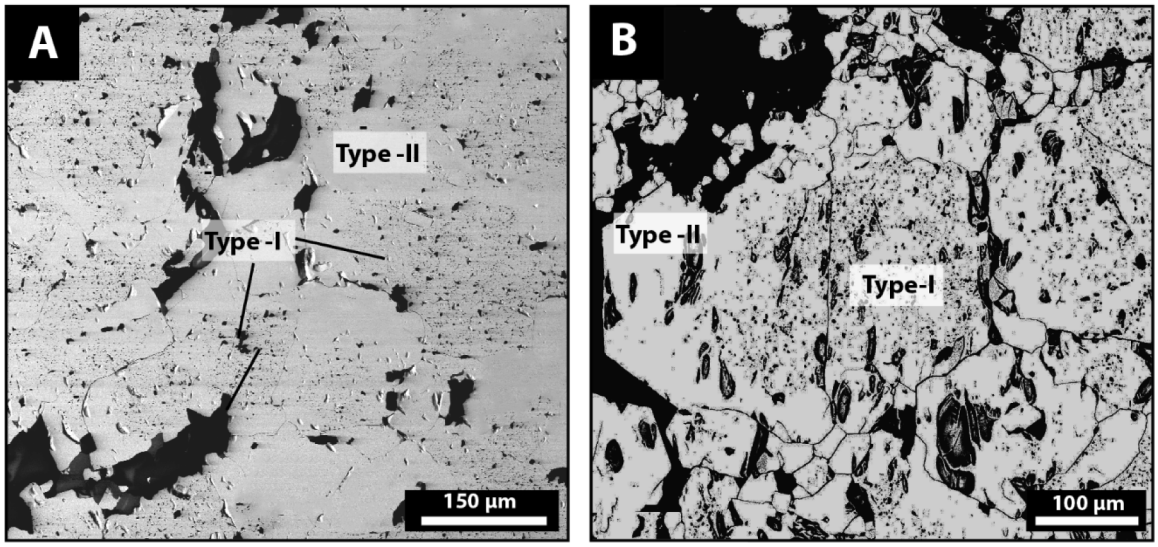

Fig. 5. Back-scattered electron images of inclusion-rich Type-I magnetite surrounded by inclusion-poor Type-II magnetite from El Romeral deposit. (A) Sample collected from the massive ore body at ~ 347 m depth. (B) Sample collected from the massive ore body at 10 m depth .The images correspond to the magnetite grains analyzed by EMPA and LA-ICP-MS (this study).

making it one of the largest Chilean iron deposits. Many textures and morphologies have been described for the massive magnetite ore bodies including vesicular textures mainly at shallow levels, breccia bodies with fragments of andesite and magnetite matrix, vertical chimney-like cavities lined with euhedral magnetite crystals and intergrown with diopside and apatite, and lava-like flows dominated by a pahoehoe and locally aa texture (Nyström and Henríquez, 1994; Naslund et al., 2002; Sillitoe and Burrows, 2002; Ovalle et al., 2018).

Recently, Ovalle et al. (2018) studied drill core samples from the Laco Norte, Laco Sur and Extension Laco Sur ore bodies, and reported a similar structure and clear relationship among ore bodies, breccias and hydrothermal alteration. The main part of the massive magnetite bodies correspond to the upper zone (~0–65 m) characterized by magnetite with lava-like textures (> 90% modal), minor diopside and scarce apatite. The surface part of this zone contains magnetite with vesicular textures and a high degree of hematite and goethite alteration, while the deepest part of this zone is dominated by the weakly to moderate magnetite replacement by hematite and late gypsum veinlets that crosscut and fill open spaces in massive magnetite. A transition zone (65–145 m) between shallow magnetite and magnetite breccias is characterized by massive magnetite with abundant coarse-grained diopside grains that vary in size from few tens of micrometers to a few millimeters. The deepest zone (150–200 m) comprises magnetite breccia bodies with andesite fragments replaced by fine-grained diopside within a magnetite-diopside matrix. In the Pasos Blancos area, high-temperature diopside-magnetite-quartz–rich contact metamorphic aureoles associated with the emplacement of the tabular magnetite ore bodies were reported by Vivallo et al. (1994) and, at depth, an alkali-calcic alteration assemblage is particularly well-developed. This alteration has been interpreted as the result of subvolcanic contact metasomatism (Rhodes et al., 1999; Naranjo et al., 2010) and comprises intense scapolitization and diopside formation that partially to pervasively replaced andesitic fragments immersed in a magnetite-diopside-scapolite matrix. The most visible expression of the hydrothermal alteration in the complex corresponds to steam-heated zones marked by a penetrative leaching of the andesite rocks and an alteration assemblage dominated by tridymite, cristobalite, alunite and jarosite, forming silicic vein-like structures and irregular hydrothermal breccia bodies (Vivallo et al., 1994; Sillitoe and Burrows, 2002; Table 1). Large exhalative deposits represented by gypsum-rich mounds, which appear to be fossil fumaroles, are located at discrete centers of emission spatially associated with NW-trending collapse structures that controlled the late hot-spring-like geothermal activity at ELVC (Vivallo et al., 1994).

3. Samples and methods

3.1. Sources of data and samples

This study is based on new micro-textural and geochemistry data of magnetite from the Carmen, Fresia, Mariela and El Romeral deposits, and previously published data from different deposits of the Chilean Iron Belt and El Laco. The magnetite chemical data compiled from the literature correspond only to EPMA in some cases, such as El Romeral (Rojas et al., 2018b), Mantoverde (Simon et al., 2018), Candelaria (Rodriguez-Mustafa et al., 2020); and both EPMA and LA-ICP-MS in other cases, such as Los Colorados (Knipping et al., 2015a, 2015b; Deditius et al., 2018), Cerro Negro Norte (Salazar et al., 2020) and El Laco (Ovalle et al., 2018; La Cruz et al., 2020).

Regarding the new microtextural and magnetite chemical data, a total of twelve magnetite-bearing samples from Carmen (Ca-2, Ca-7, Ca-8 and Ca-9), Fresia (F-2, F-5, Fre-4 and Fre-10) and Mariela (Ma-1, Ma-10, Ma-11 and Ma-21) were selected for SEM, EMPA and LA-ICP-MS analysis. Samples from Carmen and Fresia were collected from stockpiles, whereas those from Mariela were collected from inside the abandoned underground mine. The selected samples are representative of the main styles of mineralization observed in the magnetite ore bodies. A brief description of the main magnetite mineralization styles in each deposit is presented in the SM file and shown in Fig. SM1-3. In addition, two samples from El Romeral (Rom-094 and Rom-149), collected from drill cores, were also analyzed in this study. Sample Rom-094 represents the main magnetite ore body (Cerro Principal) at depth of ~ 347 m, whereas sample Rom-149 was collected from a contact zone between the magnetite ore body and the host andesite at shallow levels (~10 m). Both samples contain the main and most abundant textural magnetite types (Type-I and -II) identified in the deposit (Rojas et al., 2018b). These samples were studied to determine possible variations in the magnetite trace element composition with depth.

3.2. SEM and EPMA

Carbon coated polished sections were studied by using a FEI Quanta 250 SEM at the Andean Geothermal Center of Excellence (CEGA) in the

Table 2
Summary of the main magnetite types and observed microtextures in the Andean IOA deposits under study.

Sector/classification	Magnetite type	Main features/microtextures	Mineral inclusions	Data source	Geochemical analyses
Carmen					
Massive magnetite ore body (apatite-rich)	Type-I	Inclusion-rich magnetite. Some magnetite exhibit oscillatory zoning (bands of 5–70 μm wide). Ca-Mg-carbonates, apatite, monazite and titanite veinlets crosscut and fill open spaces (~50 modal %).	Abundant mineral inclusions (~30 μm to < 1 μm) aligned along magnetite crystallographic planes or randomly distributed. In grains with oscillatory zoning, inclusions are concentrated in darker bands: Mg, Al, Fe-bearig silicates, Ilm and Rt.	This study	EPMA and LA-ICP-MS
	Type-II	Inclusion-free, pristine magnetite veinlets that crosscut magnetite Type-I .		This study	EPMA and LA-ICP-MS
	Type-III	Large magnetite grains intergrown with coarse actinolite and apatite crystals. Some grains exhibit porosity or show recrystallization textures (fine-grained aggregates of magnetite exhibiting a mosaic texture) (~30 modal %).	Nano-inclusions/exsolution lamellae either oriented, randomly distributed or clustered in the grain cores.	This study	EPMA and LA-ICP-MS
	Type-IV	Late generation of inclusion-poor magnetite veinlets (few cm-tens cm) that crosscut magnetite Type-III . Type-IVa is associated with Cl-rich apatite, monazite and enstatite, whereas Type-IVb exhibits porosity.		This study	EPMA and LA-ICP-MS
Fresia					
Massive magnetite ore body (apatite-rich)	Type-A	Massive magnetite that exhibits a well-developed and clear oscillatory zoning. Some grains are recrystallized to subhedral porous aggregates of magnetite (foam-like triple junctions) (~40 modal %).	Scarce mineral inclusions.	This study	EPMA and LA-ICP-MS
	Type-B	Matrix of magnetite aggregates in which apatite and minor actinolite are intergrown. Some grains exhibit exsolution lamellae (~30 modal %).	Some grains exhibit submicrometer-sized inclusions mainly oriented along magnetite crystallographic planes.	This study	EPMA and LA-ICP-MS
	Type-C	Crustiform-colloform banding magnetite that forms succesive bands of magnetite, minor quartz and Cl-rich apatite. Some individual grains are recrystallized to fine-grained magnetite and/or exhibit porosity and oscillatory zoning. (~25 modal %).	Scarce mineral inclusions.	This study	EPMA and LA-ICP-MS
	Type-D	Late magnetite veinlets (centimetric), intergrown with actinolite crystals, which crosscut the altered host rock at the margin of the deposit. Porous and recrystallized magnetite grains are characterized by mosaic texture (~5 modal %).		This study	EPMA and LA-ICP-MS
Mariela					
Breccia pipe (apatite-rich)	Type-α	Magnetite with symplectite texture (interstitial magnetite and rutile-titanite ± ilmenite of vermicular morphology. Hematite replacement occurs along both grain boundaries and crystallographic planes (~40 modal %).		This study	EPMA and LA-ICP-MS
	Type-β	Magnetite with ulvöspinel/ilmenite exsolution lamellae. It occurs in sharp contact with Type-α. Replaced by hematite along grain boundaries and crystalographic planes (~5 modal %).	Nano-inclusions of Fe-Ti-oxides.	This study	EPMA and LA-ICP-MS
	Type-γ	Late generation of pristine magnetite. It occurs as an overgrown and as veinlets that crosscutType α (~30 modal %).	Act	This study	EPMA and LA-ICP-MS
	Type-δ	Subhedral magnetite that that occurs forming veinlets with minor apatite that crosscut the altered host rock. It is characterized by a well-defined cubic cleavage and exsolution lamellae (unspecific Fe-Mg-Al-O-bearing mineral). Titanite, rutile and an unspecified Mn-silicate occur along crystallographic planes (~10 modal %).		This study	EPMA and LA-ICP-MS
	Type-ε	Si-rich magnetite replacement with a colloform-banding texture, sometimes, surrounding pyrite grains (< 10 μm). It occurs intergrown with bladed specular hematite and quartz (~10 modal %).		This study	NA
El Romeral					

(*continued on next page*)

Table 2 (*continued*)

Sector/classification	Magnetite type	Main features/microtextures	Mineral inclusions	Data source	Geochemical analyses
Magnetite ore body (central and deep parts of the system)	Type-I	Early, inclusion-rich magnetite cores (~35 modal %).	Oriented or randomly distributed high-temperature polycrystalline and one-phase inclusions (50 μm-few nanometers). Large inclusions: Act, Ilm and Rt. Small inclusions: Rt, Ilm, Ttn, Chl, Phl, NaCl, Prg, Clc, Cal and Tr. At shallow depths (< 100 μm), Si-rich inclusions occur aligned along magnetite crystallographic planes.	This study; Rojas et al. (2018b)	EPMA and LA-ICP-MS
	Type-II	Pristine, inclusion-free magnetite rim. It occurs as an overgrowth on magnetite Type I (~60 modal %).		This study; Rojas et al. (2018b)	EPMA and LA-ICP-MS
Magnetite ore body (margin and shallow portions of the system)	Type-III	Inclusion-poor, chemically-zoned magnetite (~5 modal %).		Rojas et al. (2018b)	NA
Magnetite ore body (central and deep parts of the system)	Type-IV	Inclusion-poor magnetite veinlets that crosscut the massive magnetite (late event).		Rojas et al. (2018b)	NA
Los Colorados					
Massive magnetite Western dike	Type-1	Inclusion-rich magnetite cores.	Polycrystalline large inclusions (≥10 μm): Act, Cpx, Ttn, and an unspecified Mg-Al-Si-phase. Smaller inclusions often contain NaCl and KCl crystals.	Knipping et al. (2015a) and Knipping et al. (2015b)	EPMA and LA-ICP-MS
	Type-2	Pristine to inclusion-poor transition zone.		Knipping et al. (2015a) and Knipping et al. (2015b)	EPMA and LA-ICP-MS
	Type-3*	Inclusion-free rims.		Knipping et al. (2015a) and Knipping et al. (2015b)	EPMA and LA-ICP-MS
Late-stage magnetite veinlets in the diorite intrusion (hydrothermal)	Magnetite-X	Euhedral magnetite with oscillatory and sector zoning. Some magnetite is partly recrystallized to porous fine-grained (~5 μm) microcrystalline aggregates of Magnetite-X and silicates (e.g., amphibole).		Deditius et al. (2018)	EPMA
	Magnetite-Y	Magnetite with "tooth-like" texture and sector zoning (~500 μm size).	Di, Cen, Am, Mca, Usp and Ti-mgt.	Deditius et al. (2018)	EPMA
	Magnetite-Z	Coarsed-grained magnetite with oscillatory zoning. Volumetrically, the most abundant of the three types of the late-stage magnetite veinlets.	Si and Al form particles in trace element-rich bands of magnetite (zones enriched in Al, Mg, Si and Ca); Ti and Mn form particles in trace element-poor bands (zones depleted in Al, Mg, Si and Ca).	Deditius et al. (2018)	EPMA
Cerro Negro Norte					
Massive magnetite ore body	Type-I	Inclusion-rich magnetite cores.	Single or polycrystalline inclusions randomly distributed and/or arranged following crystallographic planes in magnetite (nano-meter size to a few tens of um): Act, Qz, Mg-Al-Si-phase, Rt, Ilm, Aug, Hy-En.	Salazar et al. (2020)	EPMA and LA-ICP-MS
	Type-II	Pristine, inclusion-free magnetite rims. It occurs as an overgrowth on Type I.		Salazar et al. (2020)	EPMA and LA-ICP-MS
	Type-III	Sub-to idiomorphic octahedral grains with an inclusion-poor core displaying a cryptic zonation towards the rim of the crystal.		Salazar et al. (2020)	EPMA and LA-ICP-MS
	Type-IV	Late magnetite vein event that crosscuts all the other magnetite types.	Randomly distributed inclusions and/or organized in repetitive sinous arrangements (micron-to sub-micron sized): Act, Qz, Aeg, Hy-En.	Salazar et al. (2020)	EPMA and LA-ICP-MS
El Laco-Laco Norte					
Massive magnetite ore body (shallow-surface outcrop)	Magnetite-S**	Magnetite (> 500 μm size) with abundant microporosity and pervasive replacement by hematite and goethite (grain boundaries, fractures and pores).		Ovalle et al. (2018)	EPMA and LA-ICP-MS

(*continued on next page*)

Table 2 (*continued*)

Sector/classification	Magnetite type	Main features/microtextures	Mineral inclusions	Data source	Geochemical analyses
Massive magnetite ore body (shallow-surface outcrop)	Magnetite-A, -S1 and -S2	Magnetite-A is defined as a Si-rich magnetite, whereas Magnetite-S1 (inclusion-rich) and -S2 (inclusion-poor) are defined based on their abundance of mineral inclusions.		La Cruz et al. (2020)	LA-ICP-MS
Massive magnetite ore body (shallow depths: < 65 m)	Magnetite-Z	Weakly to moderate oxidized magnetite with hematite formation along rims or through fractures. It forms aggregates of pristine, mostly euhedral crystals (~10–120 μm). Late gypsum veinlets crosscut and fill open spaces in massive Magnetite-Z.		Ovalle et al. (2018)	EPMA and LA-ICP-MS
Massive magnetite ore body (intermediate depths: 65–145 m)	Magnetite-X	Magnetite with pristine microcrystalline cores (~500 μm). Replaced by Magnetite-Y.		Ovalle et al. (2018)	EPMA and LA-ICP-MS
	Magnetite-Y	Magnetite with oscillatory texture (individual bands of ~ 4–100 μm)		Ovalle et al. (2018)	EPMA and LA-ICP-MS
	Magnetite-γ	It occurs as an overgrown on inclusion-rich relict cores of Magnetite-β.	Inclusions from 10́s to 100́s nanometers to a few micrometers	Ovalle et al. (2018)	EPMA and LA-ICP-MS
Breccia body (deep zone: ~150 m)	Magnetite-β	Coarse-grained euhedral crystals that contain inclusion-rich cores (Magnetite-β) surrounded by inclusion-free rims (Magnetite-β1). A third generation of smaller anhedral magnetite crystals associated with gypsum veinlets occurs at the outer rim of the inclusion-free magnetite (Magnetite- β2).		Ovalle et al. (2018)	EPMA and LA-ICP-MS
Breccia body (deep zone: > 150 m)	Magnetite-α	Aggregates of titano-magnetite crystals (~100–300 μm size) with well-developed ilmenite exsolution lamellae and oxidation zones along grain rims and fractures.		Ovalle et al. (2018)	EPMA and LA-ICP-MS

Notes:

* Magnetite Type-3 defined by Knipping et al. (2015a) and Knipping et al. (2015b) was later classified as Magnetite-X, -Y, and -Z by Deditius et al. (2018).

** Magnetite-S defined by Ovalle et al. (2018) was later redefined as Magnetite-A, -S1 and -S2 by La Cruz et al. (2020).

Abbreviations: NA = not analyzed, Act = actinolite, Aeg = aegirine, Am = amphinole, Aug = augite, Cal = calcite, Cen = clinoenstatite Chl = chlorite, Clc = clinochlore, Cpx = clinopyroxene, Di = diopside, En = enstatite, Hy = hyperthene, Ilm = ilmenite, Mca = mica, Phl = phlogopite, Prg = pargasite, Qz = quartz, Rt = rutile, Tr = tremolite, Ti-mgt = Ti-rich magnetite, Ttn = titanite,Usp = ulvöspinel.

Table 3
Data summary of EPMA analyses for magnetite types from Carmen, Fresia, Mariela, El Romeral, Los Colorados, Cerro Negro Norte and El Laco.

Magnetite type	Data source	N	Mg	n	Al	n	Si	n	Ca	n	Ti	n	V	n	Mn	n	Fe	O	Total
Carmen																			
Type-I	This study	30	0.02–0.40	0	BDL-0.11	5	0.01–0.59	0	BDL-0.29	3	BDL-0.13	19	0.16–0.32	0	BDL-0.13	6	69.1–73.1	26.2–27.9	96.4–102
			0.18		*0.05*		*0.13*		*0.04*		*0.07*		*0.25*		*0.07*		*70.5*	*26.9*	*98.3*
			Oscillatory zoning: light BSE bands																
		10	0.12–0.24	0	0.03–0.09	0	0.01–0.11	0	0.01–0.05	0	BDL-0.13	7	0.16–0.29	0	BDL-0.11	4	69.6–73.1	26.5–27.9	97.2–102
			0.17		*0.05*		*0.11*		*0.04*		*0.07*		*0.24*		*0.07*		*70.6*	*26.9*	*98.4*
			Oscillatory zoning: dark BSE bands																
		8	0.12–0.40	0	BDL-0.11	1	0.02–0.59	0	0.02–0.29	*0*	BDL-0.08	*3*	0.17–0.31	0	BDL-0.09	1	69.3–71.3	26.4–27.2	96.4–99.4
			0.23		*0.07*		*0.16*		*0.07*		*0.07*		*0.26*		*0.06*		*70.5*	*26.8*	*98.4*
Type-II	This study	18	0.02–0.21	0	BDL-0.10	6	BDL-0.03	4	BDL-0.03	11	BDL-0.07	16	0.18–0.37	0	BDL-0.15	2	69.8–72.07	26.6–27.5	97–100
			0.09		*0.05*		*0.02*		*0.02*		*0.06*		*0.25*		*0.07*		*71.06*	*27.1*	*98.8*
Type-III	This study	28	BDL-0.27	1	0.01–0.08	0	0.01–0.56	0	BDL-0.09	1	BDL-0.11	21	0.18–0.35	0	0.02–0.18	0	66.6–72.0	25.3–27.4	93.1–100
			0.10		*0.04*		*0.20*		*0.04*		*0.08*		*0.26*		*0.10*		*69.1*	*26.3*	*96.3*
Type-IVa	This study	23	BDL-0.22	2	BDL-0.22	4	BDL-9.25	2	BDL-0.06	8	BDL-0.29	16	0.11–0.35	0	0.03–0.19	0	67.7–71.0	25.7–27.1	94.3–98.9
			0.07		*0.07*		*0.06*		*0.02*		*0.14*		*0.25*		*0.10*		*69.3*	*26.4*	*96.5*
Fresia																			
Type-A	This study		*Oscillatory zoning: light BSE bands*																
		10	0.11–0.43	0	0.09–0.25	0	0.49–0.93	0	0.13–0.29	0	BDL-0.1	1	BDL-0.16	1	BDL-0.09	3	67.6–70.1	25.5–26.5	95.2–98.0
			0.23		*0.16*		*0.73*		*0.20*		*0.10*		*0.09*		*0.05*		*68.7*	*26.0*	*96.4*
			Oscillatory zoning: dark BSE bands																
		10	0.15–0.52	0	0.3–0.46	0	1.09–1.29	0	0.35–0.51	0	0.15–0.28	0	0.04–0.13	0	0.03–0.1	0	66.4–67.8	24.8–25.3	94.0–95.6
			0.28		*0.39*		*1.22*		*0.39*		*0.22*		*0.10*		*0.06*		*66.9*	*25.0*	*94.8*
Type-B	This study	10	BDL-0.16	4	0.1–0.21	0	BDL-0.26	2	BDL-0.11	4	BDL-0.15	3	0.13–0.3	0	BDL-0.13	3	69.1–70.4	26.3–26.8	96.0–97.9
			0.05		*0.12*		*0.06*		*0.04*		*0.10*		*0.22*		*0.06*		*69.8*	*26.5*	*97.1*
Type-C	This study	24	0.03–0.56	0	BDL-0.24	5	0.19–1.4	0	BDL-0.5	1	BDL-0.07	22	BDL-0.13	15	BDL-0.13	12	67.7–72.2	25.4–27.4	95.1–100
			0.19		*0.06*		*0.74*		*0.22*		*0.06*		*0.05*		*0.07*		*70.1*	*26.5*	*98.0*
			Oscillatory zoning: light BSE bands																
		5	0.05–0.26	0	BDL-0.04	2	0.19–0.54	0	BDL-0.1	1	BDL-BDL	5	BDL-0.13	3	BDL-0.04	3	70.3–72.2	26.7–27.4	98.1–100
			0.13		*0.02*		*0.34*		*0.07*				*0.07*		*0.04*		*71.5*	*27.2*	*99.4*
			Oscillatory zoning: dark BSE bands																
		6	0.13–0.56	0	BDL-0.09	1	0.58–1.4	0	0.14–0.5	0	BDL-BDL	6	BDL-0.04	3	BDL-0.13	4	68.8–71.4	25.8–27.0	97.0–99.6
			0.46		*0.03*		*1.08*		*0.31*				*0.04*		*0.11*		*69.6*	*26.2*	*98.0*
Type-D	This study	11	0.15–0.4	0	0.05–0.12	0	0.46–0.97	0	0.09–0.19	0	BDL-0.15	7	0.03–0.24	0	BDL-0.05	6	66.6–68.4	25.1–25.8	93.2–95.5
			0.25		*0.07*		*0.74*		*0.14*		*0.11*		*0.15*		*0.03*		*67.4*	*25.5*	*94.5*
Mariela																			
Type-α	This study	23	BDL-0.23	2	0.01–0.13	0	BDL-0.54	0	BDL-0.14	1	BDL-0.98	0	0.63–2.28	0	BDL-0.22	4	62.0–69.3	23.4–26.3	87.3–97.7
			0.1		*0.05*		*0.17*		*0.06*		*0.45*		*1.62*		*0.11*		*67*	*25.3*	*94.8*
Type-β	This study	9	0.18–0.37	0	0.05–0.15	0	0.10–0.50	0	0.03–0.25	0	BDL-0.18	1	1.64–2.11	0	BDL-0.09	3	65.0–66.5	24.6–25.2	92.4–94.6
			0.22		*0.11*		*0.25*		*0.11*		*0.13*		*1.92*		*0.06*		*65.6*	*24.9*	*93.5*
Type-γ	This study	28	BDL-0.15	1	BDL-0.06	3	0.01–0.45	0	BDL-0.20	6	BDL-0.18	15	0.38–0.85	0	BDL-0.80	6	63.1–70.6	23.9–26.9	88.6–98.6
			0.08		*0.03*		*0.08*		*0.04*		*0.08*		*0.69*		*0.10*		*67.7*	*25.8*	*94.7*
Type-δ	This study	20	BDL-0.11	2	0.15–0.46	0	BDL-0.18	1	BDL-0.13	8	BDL-0.28	10	0.89–1.19	0	BDL-0.16	3	66.4–69.1	25.2–26.2	93.5–95.9
			0.03		*0.25*		*0.04*		*0.03*		*0.14*		*1.06*		*0.08*		*68.3*	*25.9*	*95.9*
El Romeral																			
Type-I (deep)	Rojas et al. (2018b)	60	BDL-1.91	23	0.005–0.30	0	0.01–3.47	*0*	0.006–0.94	0	0.005–0.81	0	0.24–0.28	0	0.01–0.15	0	66.5–73.0	27.1–29.0	97.8–102
			0.19		*0.04*		*0.26*		*0.10*		*0.10*		*0.26*		*0.04*		*71.0*	*27.8*	*99.7*
Type-II (deep)	Rojas et al. (2018b)	51	BDL-0.59	41	0.005–0.46	0	BDL-1.19	*11*	BDL-0.10	22	0.005–1.14	0	0.23–0.33	0	0.01–0.04	0	69.3–73.0	27.4–28.5	99.1–102
			0.08		*0.04*		*0.06*		*0.02*		*0.06*		*0.26*		*0.02*		*72.3*	*27.9*	*101*
Type-I (shallow)	This study	21	BDL-0.02	14	BDL-0.06	2	BDL-0.31	9	BDL-0.24	3	BDL-0.23	17	0.09–0.21	0	BDL-0.14	2	71.7–74.0	27.2–28.2	100–103
			0.01		*0.02*		*0.05*		*0.03*		*0.09*		*0.15*		*0.05*		*73.1*	*27.9*	*101*

(*continued on next page*)

Table 3 (*continued*)

Magnetite type	Data source	N	Mg	n	Al	n	Si	n	Ca	n	Ti	n	V	n	Mn	n	Fe	O	Total
Type-II (shallow)	This study	20	BDL-0.02 *0.01*	13	BDL-0.03 *0.02*	4	BDL-0.07 *0.02*	8	BDL-0.05 *0.02*	13	BDL-0.14 *0.07*	18	0.04–0.20 *0.14*	0	BDL-0.08 *0.06*	4	72.4–74.3 *73.1*	27.6–28.3 *27.9*	101–103 *101*
Los Colorados																			
Type-1*	Knipping et al. (2015a) and Knipping et al. (2015b)	20	0.18–0.78 *0.49*	0	0.12–0.7 *0.48*	0	BDL-0.66 *0.36*	6	BDL-0.3 *0.15*	6	0.3–0.75 *0.44*	0	0.49–0.68 *0.62*	0	0.09–0.23 *0.14*	0	65.2–68.6 *67.2*	26.8–27.8 *27.4*	96.5–98.0 *97.2*
Type-2*	Knipping et al. (2015a) and Knipping et al. (2015b)	41	0.08–0.48 *0.19*	0	0.04–0.35 *0.17*	0	BDL-0.39 *0.05*	*7*	BDL-0.08 *0.03*	7	0.03–0.39 *0.12*	0	0.27–0.68 *0.35*	0	0.06–0.19 *0.12*	0	67.8–71.0 *70.2*	26.4–27.9 *27.4*	95.0–100 *98.6*
Type-3*	Knipping et al. (2015a) and Knipping et al. (2015b)	12	0.06–0.23 *0.13*	0	BDL-0.06 *0.03*	7	BDL-0.09 *0.05*	*8*	BDL-0.05 *0.02*	2	0.01–0.24 *0.03*	0	0.05–0.36 *0.21*	0	0.08–0.11 *0.095*	0	69.5–70.6 *69.9*	26.8–27.4 *27.0*	97–98.8 *97.5*
All Data**	Knipping et al. (2015a) and Knipping et al. (2015b)	551	BDL-6.96 *0.29*	4	BDL-1.82 *0.21*	8	BDL-4.18 *0.15*	42	BDL-3.64 *0.08*	61	BDL-9.0 *0.24*	21	0.05–0.68 *0.30*	0	0.02–2.23 *0.13*	0	43.8–72.5 *70.6*	25.2–31.4 *27.8*	86.2–103 *99.7*
Magnetite-X	Deditius et al. (2018)	49	0.05–0.81 *0.24*	0	0.19–1.10 *0.46*	0	0.04–1.34 *0.48*	0	0.01–0.37 *0.14*	0	0.07–0.85 *0.14*	0	0.26–0.27 *0.26*	0	0.03–0.27 *0.07*	0	66.4–71.6 *70.0*	25.3–27.3 *26.7*	96.3–99.8 *98.6*
Magnetite-Y	Deditius et al. (2018)	50	0.01–0.93 *0.23*	0	0.18–1.21 *0.50*	0	BDL-2.18 *0.43*	4	BDL-0.91 *0.19*	6	0.08–5.49 *0.27*	0	0.22–0.27 *0.26*	0	0.04–5.10 *0.20*	0	60.7–72.3 *70.0*	23.2–27.6 *26.7*	95–101 *99.0*
Magnetite-Z	Deditius et al. (2018)	94	0.01–2.06 *0.30*	0	0.13–1.18 *0.42*	0	0.009–1.83 *0.40*	0	0.01–0.59 *0.16*	0	0.06–1.27 *0.15*	0	0.21–0.24 *0.23*	0	0.02–0.23 *0.10*	0	65.2–72.2 *70.0*	24.9–27.5 *26.7*	96.4–100 *98.6*
Cerro Negro Norte																			
Type-I	Salazar et al. (2020)	41	BDL-0.11 *0.06*	2	BDL-0.43 *0.06*	17	BDL-0.50 *0.08*	22	BDL-0.19 *0.05*	20	BDL-0.36 *0.08*	29	0.17–0.30 *0.21*	0	BDL-0.06 *0.06*	39	68.9–71.4 *70.7*	26.5–27.7 *27.2*	96.0–99.2 *98.2*
Type-II	Salazar et al. (2020)	36	BDL-0.03 *0.03*	35	BDL-0.20 *0.66*	2	BDL-0.17 *0.09*	22	BDL-9.16 *0.05*	31	BDL-0.15 *0.10*	28	0.16–0.30 *0.21*	0	BDL *BDL*	36	68.9–71.4 *70.8*	26.5–27.4 *27.2*	95.7–99.2 *98.3*
Type-III	Salazar et al. (2020)	110	BDL-0.40 *0.12*	16	BDL-0.84 *0.09*	14	BDL-2.23 *0.20*	77	BDL-0.37 *0.13*	95	BDL-0.73 *0.08*	77	BDL-0.21 *0.13*	*34*	BDL-0.058 *0.06*	109	63.8–72.3 *70.6*	26.3–27.7 *27.2*	95.2–99.1 *99.6*
Type-IV	Salazar et al. (2020)	62	BDL-0.82 *0.18*	52	BDL-0.30 *0.10*	34	BDL-2.82 *0.22*	*30*	BDL-1.76 *0.15*	35	BDL-0.04 *0.04*	61	BDL-0.14 *0.09*	*23*	0.060 *0.06*	61	62.6–72.0 *70.6*	26.7–27.6 *27.1*	95.8–99.8 *98.1*
El Laco																			
Magnetite-S	Ovalle et al. (2018)	324	BDL-2.04 *0.56*	279	BDL-1.37 *0.12*	157	BDL-1.93 *0.32*	0	BDL-0.55 *0.14*	67	0.005–0.03 *0.006*	0	BDL-0.18 *0.06*	3	BDL-0.17 *0.04*	90	64.7–72.7 *69.1*	26.4–28.5 *27.7*	95.0–101 *97.6*
Magnetite-Z	Ovalle et al. (2018)	33	0.1–0.89 *0.73*	*0*	0.09–0.22 *0.18*	0	0.01–0.09 *0.05*	0	BDL-0.06 *0.1*	29	0.09–0.18 *0.13*	0	0.16–0.2 *0.19*	0	BDL-0.06 *0.04*	14	67.8–70.9 *70.2*	26.8–28.1 *27.8*	95.7–100 *99.3*
Magnetite-X	Ovalle et al. (2018)	38	0.44–1.24 *0.64*	*0*	0.18–0.91 *0.44*	0	0.01–0.39 *0.07*	0	BDL-0.2 *0.05*	20	0.12–0.56 *0.24*	0	0.16–0.22 *0.19*	0	BDL-0.09 *0.04*	5	69.0–71.1 *70.5*	27.4–28.8 *28.1*	98.1–102 *100*
Magnetite-Y	Ovalle et al. (2018)	42	0.56–1.75 *0.9*	42	0.39–0.98 *0.52*	0	0.04–1.71 *0.5*	0	BDL-0.66 *0.2*	1	0.17–0.75 *0.29*	0	0.16–0.20 *0.18*	0	BDL-0.10 *0.05*	3	65.2–70.6 *69.1*	28.0–29.1 *28.3*	98.2–101 *100*
Magnetite-γ	Ovalle et al. (2018)	12	BDL-0.65 *0.35*	4	0.08–0.42 *0.19*	0	0.01–0.81 *0.29*	0	BDL-0.08 *0.04*	8	0.04–0.19 *0.12*	0	0.20–0.39 *0.25*	0	0.01–0.01 *0.01*	12	66.9–69.6 *68.5*	26.7–27.1 *26.9*	95.6–96.5 *96.5*
Magnetite-α	Ovalle et al. (2018)	28	0.07–0.75 *0.29*	0	0.21–0.82 *0.5*	0	0.01–0.96 *0.1*	0	BDL-0.30 *0.12*	21	0.38–1.66 *0.76*	0	0.21–0.32 *0.26*	0	0.01–0.03 *0.01*	0	66.7–71.2 *69.9*	27.7–28.3 *27.3*	98.4–100 *99.7*
Magnetite β, β1, β2	Ovalle et al. (2018)	24	0.16–0.96 *0.60*	0	0.07–0.58 *0.41*	0	0.01–0.61 *0.09*	0	BD-0.43 *0.14*	*13*	0.06–1.54 *0.57*	0	0.01–0.29 *0.26*	0	0.01–0.1 *0.03*	24	67.9–71.3 *69.5*	27.1–28.4 *27.9*	97.4–100 *99.7*

Notes:

The range indicates the minimum and maximum concentration. The average is shown in italics.

N = number of analyses, n = number of analyses BDL (below detection limit) for Mg, Al, Si, Ca, Ti , V and Mn.

* Representative concentrations for magnetite Type-1, −2 and −3 from Los Colorados drill-core LC-05–129. Many magnetite grains do not exhibit Type-3 and in many cases the concentrations of Type-1 and −2 overlap.

** Concentrations calculated from all data from Knipping et al. (2015a) and Knipping et al. (2015b). Data not sorted by magnetite type.

Table 4
Data summary of the most relevant trace elements (in ppm) determined by LA-ICP-MS spot analyses in magnetite types from Carmen, Fresia, Mariela, El Romeral and Cerro Negro Norte.

	Carmen						Fresia						Mariela					
Data source	This study						This study						This study					
Element	n	Type I (N = 40)	n	Type II (N = 10)	n	Type III (N = 44)	n	Type A (N = 35)	n	Type B (N = 44)	n	Type C (N = 34)	n	Type α (N = 39)	n	Type β (N = 23)	n	Type γ (N = 40)	n
Mg	0	1990–57-10 *3842*	0	1213–22-40 *2811*	1	BDL-1666 *965*	0	1061–39-40 *2214*	0	39.2–198-0 *460*	0	635–4297 *2019*	3	BDL-2970 *617*	0	864–3990 *2049*	0	271–8340 *1695*	0
Al	0	299–1770 *1036*	0	460–925 *744*	0	196–1223 *560*	0	309–4680 *1710*	0	682–2549 *1824*	0	38.5–121-5 *305*	0	196–1045 *435*	0	211–1036 *728*	0	114–571 *250*	0
Ti	0	445–2510 *1108*	0	437–2240 *1032*	0	131–4120 *794*	0	206–2106 *893*	0	414–9100 *2921*	6	BDL-523 *63.7*	20	BDL-6850 *1038*	0	383–990-00 *11,151*	0	159–4760 *680*	0
V	0	1900–21-60 *2013*	0	1930–20-96 *2010*	1	BDL-2710 *2411*	0	435–828 *595*	0	1659–18-79 *1756*	0	18.3–405 *146*	0	4790–15-230 *9049*	0	11570–1-6800 *13,908*	0	4760–68-10 *5874*	0
Cr	40	BDL-BDL	10	BDL-BDL	44	BDL-BDL	34	BDL-5.5 *5.5*	44	BDL-BDL	34	BDL-BDL	1	BDL-51.2 *23.7*	4	BDL-38.5 *10.8*	25	BDL-18.7 *11.2*	6
Mn	0	376–691 *500*	0	274–610 *375*	0	906–1248 *1077*	0	230–468 *321*	0	399–1160 *559*	0	245–778 *395*	0	133–8400 *745*	0	198–3390 *604*	0	152–1628 *651*	0
Co	0	108–127 *115*	0	106–130 *116*	0	93.4–105 *99.3*	0	19.8–46.3 *27.7*	0	15.3–63.4 *28.4*	0	17.5–64 *34.3*	5	BDL-14 *6.45*	0	3.39–29.7 *15.2*	0	3.51–259 *35.3*	0
Ni	0	265–338 *305*	0	293–327 *309*	0	250–303 *283*	0	153–184 *165*	0	242–283 *260*	0	110–164 *144*	0	123–266 *204*	0	176–268 *225*	0	150–402 *283*	0
Cu	26	BDL-73.5 *9.47*	8	BDL-23 *12*	39	BDL-2.7 *1.74*	34	BDL-1.45 *1.45*	28	BDL-35.6 *8.14*	15	BDL-50.7 *17.8*	0	1.22–116-1 *315*	0	4.5–580 *143*	0	31.3–162-0 *723*	29
Zn	0	19.3–136 *64.2*	0	17.7–108 *43.7*	0	16–165 *58.6*	0	6.4–48 *20.5*	0	16.6–163 *69.7*	0	10.9–74 *32.9*	0	4.2–103 *27.6*	0	7.4–35.7 *17.4*	0	7.7–57 *20.3*	0
Ga	0	29.3–43.5 *38.5*	0	31.5–36.8 *34.9*	0	28.8–42.9 *33.4*	0	24.6–51.9 *35.0*	0	17.3–42.7 *31.9*		9.83–21.8 *14.9*	0	21.7–46.9 *39.4*	0	34.3–51.8 *45*	0	32.1–52.7 *40.2*	0
Sn	0	1.15–5.26 2.83	0	1.15–2.75 *1.83*	0	0.26–3.57 *1.21*	0	2.09–4.69 *3.25*	2	BDL-2.79 *0.94*	0	5.07–18.0 *9.85*	18	BDL-17.4 *3.86*	0	0.39–5.03 *1.12*	37	BDL-0.37 *0.28*	9

	Mariela	El Romeral								Cerro Negro Norte							
Data source	This study	This study								Salazar et al. (2020)							
		Deep (~347 m)				Shallow (~10 m)											
Element	Type δ (N = 30)	n	Type I (N = 26)	n	Type II (N = 13)	n	Type I (N = 26)	n	Type II (N = 24)	n	Type I (N = 28)	n	Type II (N = 26)	n	Type III (N = 37)	n	Type IV (N = 55)
Mg	135–1750 *465*	0	82–7130 *3361*	0	53.2–764-0 *2243*	0	71–1620 *676*	0	26.2–159-0 *347*	0	32.6–405-0 *1405*	0	17.2–185-0 *419*	0	44.1–269-0 *724*	0	8.54–4-360 *913*
Al	443–3680 *2367*	1	BDL-2290 *1384*	0	156–1470 *763*	0	86.8–105-0 *562*	0	84.9–190-0 *323*	0	130–3010 *924*	0	180–1910 *669*	0	481–2650 *1406*	0	67.3–1-290 *280*

(*continued on next page*)

Table 4 (*continued*)

Data source	Mariela	El Romeral								Cerro Negro Norte						
	This study	This study								Salazar et al. (2020)						
		Deep (~347 m)				Shallow (~10 m)										
Element	Type δ (N = 30)	n	Type I (N = 26)	n	Type II (N = 13)	n	Type I (N = 26)	n	Type II (N = 24)	n	Type I (N = 28)	n	Type II (N = 26)	n	Type III (N = 37)	n	Type IV (N = 55)
Ti	446–3870	0	103–3920	0	65–1020	0	71–1220	0	45–1100	0	70–1990	0	54.7–936	0	101–870	22	BDL-509
	1316		*803*		*342*		*571*		*222*		*330*		*327*		*340*		*72.8*
V	9120–99-10	0	3.5–2792	0	2500–28-64	0	1017–14-95	0	1045–14-93	0	1247–20-90	0	1230–21-13	0	887–1370	0	8.38–5-62
	9384		*2489*		*2683*		*1261*		*1277*		*1398*		*1737*		*1099*		*215*
Cr	BDL-24.7	25	BDL-218.3	0	BDL-BDL	26	BDL-BDL	26	BDL-BDL	27	BDL-6,7	26	–	37	–	53	BDL-9.20
	14		*218.3*								*6.7*		–		–		*6.60*
Mn	227–2250	0	45.6–357	0	186–308	0	416–561	0	441–598	0	37.5–230	0	18.9–195	0	33.2–214	0	54.7–1-53.8
	552		*272*		*238*		*510*		*499*		*134*		*107*		*110*		*82.4*
Co	14.7–32.8	0	40.4–57.5	0	40.5–51.8	0	16.5–25.3	0	13.6–24.7	0	18.3–37.1	0	18.4–33.5	0	20.6–43.7	0	9.18–1-29
	24.3		*45.6*		*51.8*		*21*		*19.3*		*25.7*		*25.5*		*27.9*		*21.9*
Ni	224–338	0	0.3–64.7	0	48.9–92	0	68.6–123	0	79.5–144	0	53.5–178	0	58.4–176	0	26.2–145	0	18.7–4-28
	292		*54.7*		*60.1*		*92.6*		*112*		*96.2*		*99*		*61.0*		*105*
Cu	BDL-10	4	BDL-9.5	10	BDL-4.6	23	BDL-2.47	22	BDL-2300	13	BDL-7.47	22	BDL-1.88	22	BDL-228	33	BDL-203
	10		*4.81*		*3.55*		*2.04*		*1151*		*3.19*		*1.17*		*41.7*		*15.7*
Zn	5.5–63.4	4	BDL-53.3	10	BDL-13	0	8.3–31.5	6	BDL-29	9	BDL-31.3	18	BDL-13.9	23	BDL-15.4	25	BDL-19.1
	24		*12.4*		*9.9*		*19.4*		*14.4*		*12.1*		*9.15*		*9.34*		*7.9*
Ga	21.4–68.3	1	BDL-60.2	0	49.9–60.9	0	17.09–20-.7	0	17.1–30.3	0	29.1–59.0	0	27.9–53.1	0	21.1–42.9	0	11.2–2-6.5
	48.5		*54.3*		*54.1*		*18.86*		*20.1*		*39.2*		*37.0*		*27.9*		*15.3*
Sn	BDL-1.16	6	BDL-4.4	6	BDL-25.6	4	BDL-2.55	18	BDL-2.27	22	BDL-2.45	24	BDL-0.87	31	BDL-1.02	45	BDL-1.11
	0.6		*1.56*		*5.89*		*1.47*		*0.70*		*1.19*		*0.87*		*0.90*		*0.80*

Department of Geology, Universidad de Chile. The SEM was used to characterize different microtextures, mineral inclusions and exsolutions in magnetite, and to select sites for both EPMA and LA-ICP-MS analyses. Backscattered-electron (BSE) images were obtained using a filament current of 80 μA, an accelerating voltage of 15 and 20 kV, a beam intensity of ~1 nA, a spot size of 5 μm, and a working distance of 10 mm.

Major and minor element concentrations in magnetite from Carmen, Fresia, Mariela and El Romeral were determined by using a JEOL JXA-8230 Superprobe at the LAMARX Laboratory of the Universidad Nacional de Cordoba, Argentina. EPMA data for El Romeral sample Rom-094 was previously reported in Rojas et al. (2018b). Magnesium, Al, Si, Ca Sc, Ti, V, Cr, Fe, Mn, Co, Zn and Nb concentrations were quantified in the magnetite grains. Operation conditions included an accelerating voltage of 15 kV, a beam current of 20 nA and a counting time of 20 s for each element. A focused beam of ~1 μm was used to avoid hitting any mineral inclusion or exsolution lamellae within magnetite grains. X-ray lines, crystals and standards used for the analyses are summarized in Table SM0. In addition to quantitative spot analyses, qualitative wavelength dispersive X-ray maps (WDS) of Mg, Al, Si, Ca, Ti, V, Fe and Mn were obtained for magnetite grains from Carmen, Fresia and Mariela by using an accelerating voltage of 15 kV, a beam current of 150 nA and a counting time of 30–40 ms/point. Interference corrections were carried out for V concentrations since Ti Kβ affects the V Kα signal.

Single-spot microanalyses were also undertaken in some Fe-Ti oxides intergrown with magnetite from Mariela, in order to properly identify these mineral phases. Analysis was performed using the same analytical conditions and standards as for magnetite, with the only exception of Ti for which a titanite standard was used (Table SM0).

3.3. Laser ablation ICP-MS

LA-ICP-MS measurements were carried out on selected magnetite grains from Carmen, Fresia, Mariela and El Romeral by using a Teledyne-Photon Machines Analyte G2 193-nm ArF excimer laser ablation coupled to a Thermo Fisher Scientific iCAP-Q quadrupole mass spectrometer at the CEGA Mass Spectrometry Laboratory, Department of Geology, Universidad de Chile. Thick sections (200 μm) were first examined by using SEM, followed by EPMA of major elements. The mass spectrometer was tuned for maximum sensitivity, low-oxide formation rate (ThO/Th $<$ 0.005) and low double-charged ion formation ($^{22}M^{+}/^{44}Ca^{++}$ $<$ 0.0005). Considering that He gas was used as a carrier and Ar as a plasma gas, interferences with these elements were evaluated when choosing representative isotopes for each element. Thus, although ^{56}Fe is more abundant than ^{57}Fe, the latter was measured to determine the iron content because ^{56}Fe has an isobaric interference with ArO.

Each spot involved a 60 s ablation time and 20 s background measurement using a laser repetition rate of 8 Hz, a fluence of 4.0–6.0 J/cm2 and a 30–40 μm spot diameter. The dwell time was 0.01 s for all the monitored isotopes: ^{23}Na, ^{24}Mg, ^{27}Al, ^{29}Si, ^{31}P, ^{39}K, ^{44}Ca, ^{45}Sc, ^{52}Cr, ^{55}Mn, ^{59}Co, ^{60}Ni, ^{63}Cu, ^{66}Zn, ^{73}Ge, ^{85}Rb, ^{88}Sr, ^{51}Y, ^{90}Zr, ^{93}Nb, ^{95}Mo, ^{107}Ag, ^{111}Cd, ^{120}Sn, ^{121}Sb, ^{138}Ba, ^{139}La, ^{140}Ce, ^{208}Pb, ^{232}Th and ^{238}U with the exception of ^{51}V, ^{49}Ti and ^{69}Ga that was 0.02 s.

The concentration of Fe in magnetite grains, determined by EPMA, was used as the internal standard for calibration. The USGS GSE-1G reference material was used for magnetite analysis and the USGS GSD-1G as a secondary standard. The USGS GSD-1G standard (Jochum et al., 2005) was used as an unknown sample to determine analytical accuracy and precision. Thirty-seven analyses were performed on the GSD standard (Table SM1) in which the trace element concentrations obtained present a small relative difference (up to 15.9%) with those reported by Jochum et al. (2005). The analytical precision determined using the GSD standard is within 2 to 5% for most analytes. LA-ICP-MS analyses were carried out using the sample-standard bracketing method with measurements of the NIST-610 glass (x 1), GSE-1G (x 2), GSD-1G (x 1), and then 20–25 unknowns, followed by measurements of GSD-1G (x 1), GSE-1G (x 2) and NIST-610 glass (x 1). Data reduction was performed by using the Iolite software (Paton et al., 2011), which calculates detection limits after Longerich et al. (1996). Heterogeneities in signal profiles due to the possible presence of micro- to nanometer-sized mineral inclusions within magnetite zones were avoided.

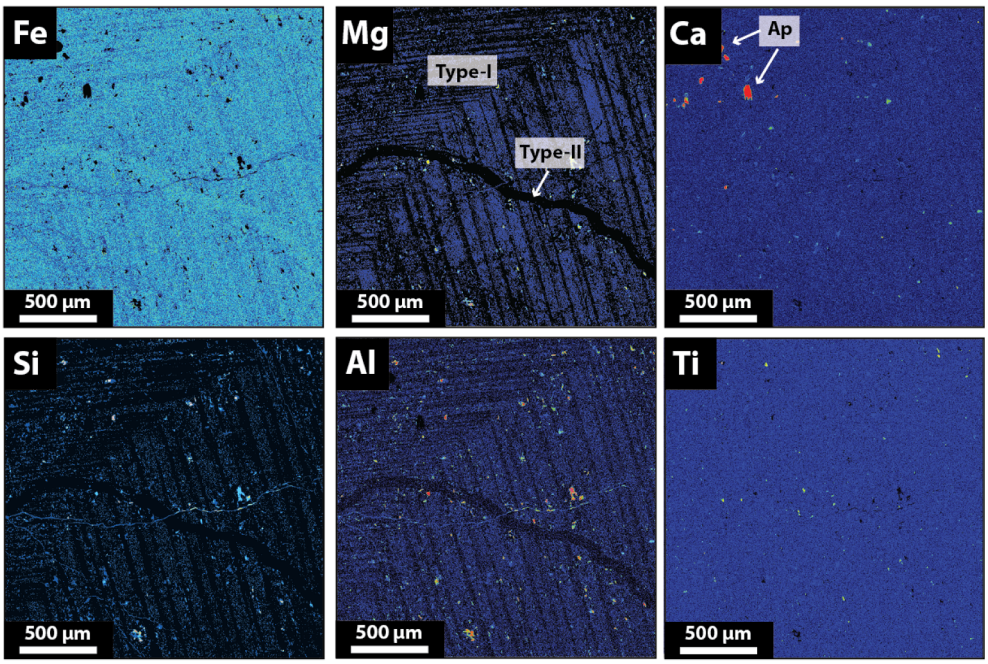

Fig. 6. WDS maps for selected elements in Type-I and -II magnetite from the Carmen deposit. Note the oscillatory zoning and the presence of scarce apatite (Ap) inclusions.

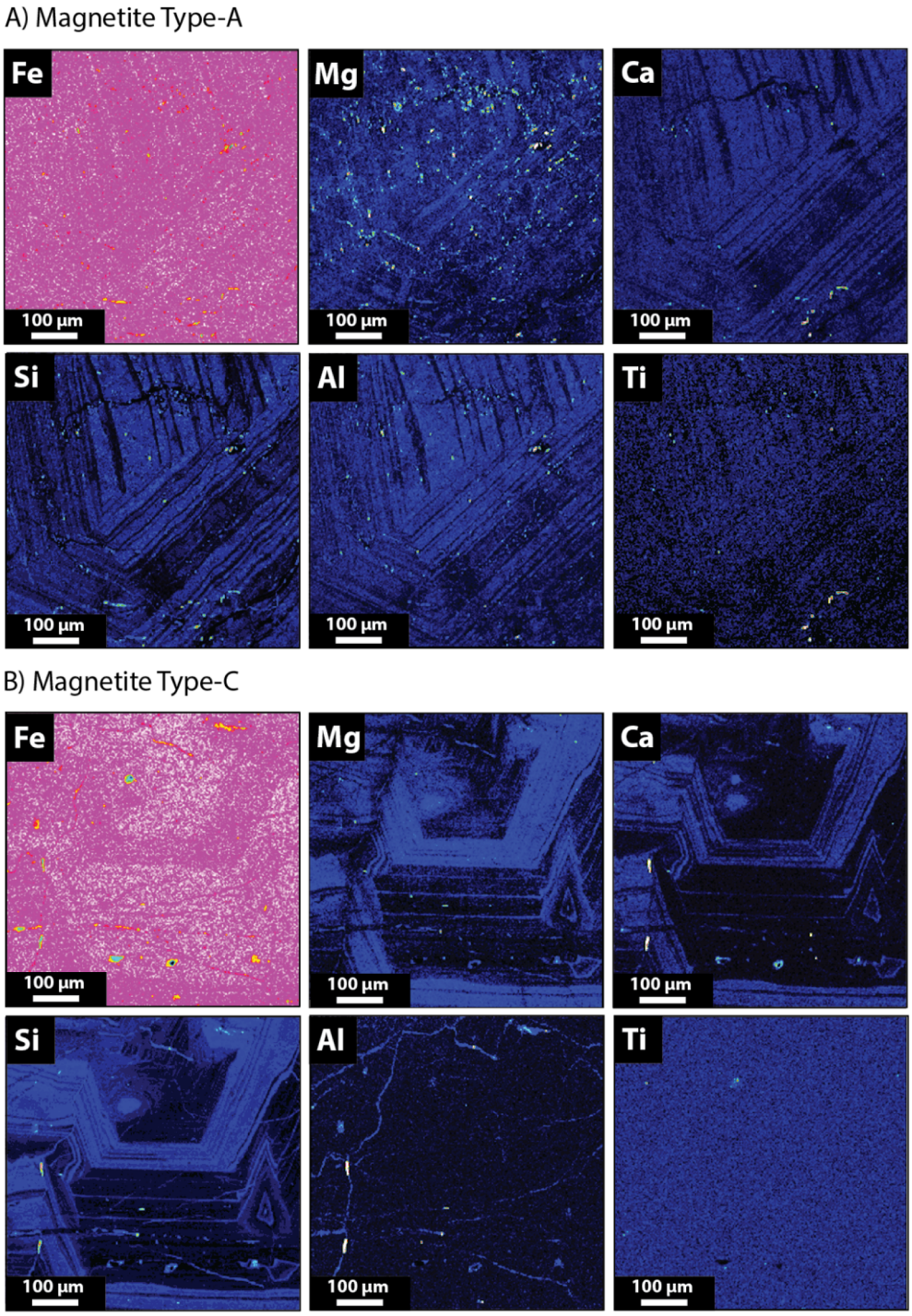

Fig.7. WDS maps for selected elements in Type-A (same as Fig. 4B) and Type-C magnetite from the Fresia deposit. Note the oscillatory zoning and the presence of abundant Mg-rich inclusions in Type-A magnetite.

4. Results

4.1. Magnetite microtextures

Magnetite in Andean IOA deposits usually shows diverse types of textures that reflect their formation conditions or post-crystallization events. Below we describe the different magnetite types identified in the Carmen, Fresia, Mariela and El Romeral deposits based on SEM observations (Figs. 2–5). In addition, the main magnetite types described at Los Colorados (Knipping et al., 2015a, 2015b; Deditius et al., 2018); El Romeral (Rojas et al., 2018b and this study); Cerro Negro Norte (Salazar et al., 2020), and El Laco (Ovalle et al., 2018) are summarized in Table 2 and described in detailed in the SM file.

4.1.1. Carmen

There are four types of magnetite in the massive magnetite ore bodies from Carmen, identified here as Type-I to –IV (Table 2). Type-I magnetite is volumetrically dominant (~50 modal%), followed by Type-III magnetite (~30 modal%). Type-I magnetite contains abundant mineral inclusions ranging in size from ~30 µm to < 1 µm and aligned along magnetite crystallographic planes or randomly distributed (Fig. 2A). Some grains exhibit oscillatory zoning (Fig. 2B,C), in which

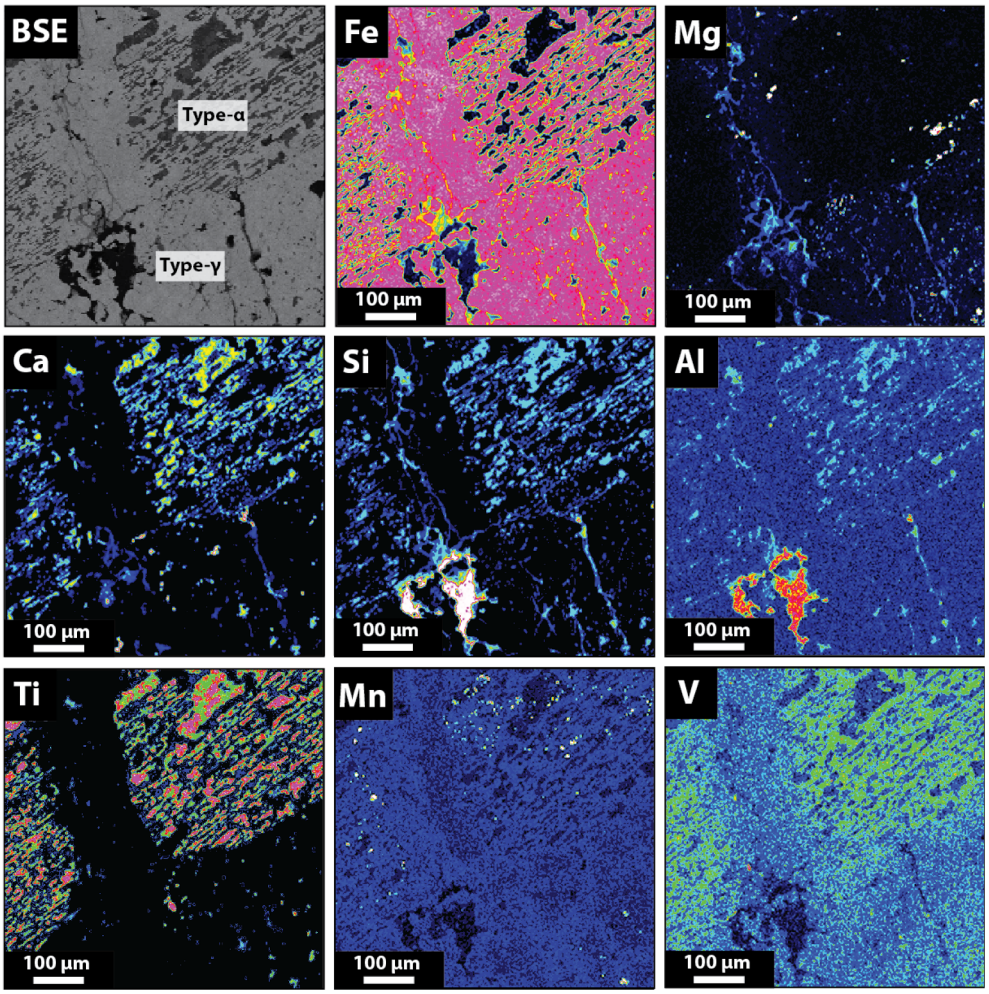

Fig.8. Back-scattered electron (BSE) image and WDS maps for selected elements in Type-α and -γ magnetite from the Mariela deposit.

inclusions are more concentrated in darker bands (Fig. 2C). The individual bands vary in width between 5 and 70 µm. Some larger inclusions are composed of Mg, Al, Fe-bearing silicates and Fe-Ti oxides such as ilmenite and rutile. Quartz, Ca-Mg-carbonates, apatite, monazite and titanite occur filling fractures and open spaces. Type-I magnetite is crosscut by pristine, inclusion-free Type-II magnetite veinlets of variable thickness (Fig. 2A,B). Type-III magnetite is defined as large magnetite grains intergrown with coarse actinolite and apatite crystals. Large apatite and actinolite crystals grew with a non-uniform distribution or perpendicular to vein walls of magnetite Type-III (Fig. 2D). This magnetite type is texturally diverse and is characterized by the occurrence of nano-inclusions/exsolution lamellae either oriented, randomly distributed or clustered in the grain cores (Fig. 2D). Some grains exhibit porosity or show recrystallization textures characterized by fine-grained aggregates of magnetite grains exhibiting a mosaic texture with 120° triple junctions (Fig. 2D). Type-IV magnetite is recognized as a late event and occurs as inclusion-poor magnetite forming veinlets that range from a few cm to tens of cm in thickness. Some of these magnetite veinlets crosscut Type-III magnetite and are associated with Cl-rich apatite, monazite and enstatite (Type-IVa; Fig. 2E), or exhibit porosity (Type-IVb; Fig. 2F).

4.1.2. Fresia

Four textural types of magnetite were identified at Fresia, including Type-A (~40 modal%), -B (~30 modal%), -C (~25 modal%) and -D (~5 modal%) (Table 2). In general, these magnetite types are partially to completely recrystallized to subhedral aggregates of porous magnetite (Fig. 3A) or display well-developed zonation, oscillatory zoning or a mosaic texture. Hematite (dark grey in BSE images) occurs as irregular patches replacing magnetite along rims and fractures (Fig. 3A). Type-A magnetite exhibits well-developed oscillatory zoning, and scarce mineral inclusions (Fig. 3B). Type-B magnetite occurs as the matrix of aggregates in which apatite and minor actinolite are intergrown. Notably, some grains of Type-B magnetite contain exsolution lamellae of a Ti-bearing mineral phase and several submicrometer-sized inclusions, mainly oriented along magnetite crystallographic planes (Fig. 3C). Type-C magnetite corresponds to a texturally crustiform-colloform banded magnetite. Successive bands of magnetite, minor quartz and fine-grained Cl-rich apatite display a rhythmic colloform texture. The width of the magnetite bands is variable, and some are altered to hematite (Fig. 3D). Recrystallization to fine grained-magnetite, porosity and/or oscillatory zoning are recognized in individual grains of the magnetite bands (Fig. 3E). Finally, Type-D magnetite forms part of cm-sized magnetite veinlets that crosscut the altered host rock at the margin of the deposit. In this type, the porous and recrystallized magnetite grains are characterized by a well-developed mosaic texture (Fig. 3F) and are intergrown with actinolite crystals that are oriented and distributed perpendicular to the walls of the veinlets.

4.1.3. Mariela

The magnetite microtextures of Mariela (Type-α, -β, -γ, -δ and -ε) are distinctly different from those described for the other deposits studied here, and reported in the cited literature (Table 2). In general, magnetite occurs in close association with ilmenite, rutile, titanite and

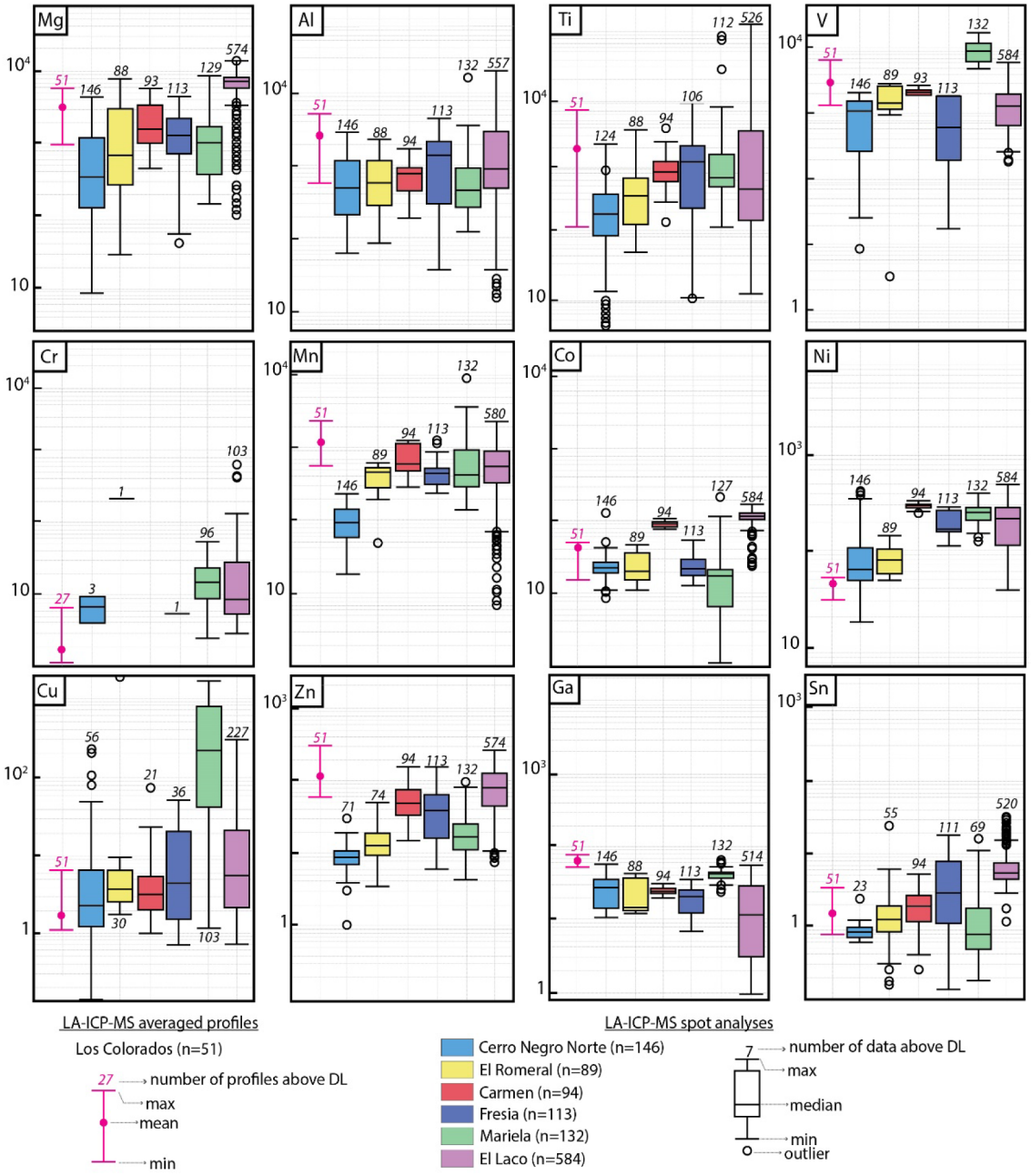

Fig. 9. Statistical summary of the most important trace element concentrations (per deposit) in magnetite from Carmen, Fresia, Mariela (this study); El Romeral (Rojas et al., 2018b and this study); Los Colorados (Knipping et al., 2015a, 2015b); Cerro Negro Norte (Salazar et al., 2020) and El Laco (La Cruz et al., 2020) determined by using LA-ICP-MS. Data in ppm.

ulvöspinel. Type-α magnetite is the most abundant textural type (~40 modal%) and is characterized by a symplectite texture composed of interstitial magnetite and rutile-titanite ± ilmenite of vermicular morphology (Fig. 4A–C). Rutile is the most abundant phase in the symplectite, whereas ilmenite is less abundant. Both rutile and ilmenite are replaced by titanite. Type-β magnetite (~5 modal%) occurs in sharp contact with Type-α magnetite (Fig. 4A,B), displays ulvöspinel/ilmenite exsolution lamellae and is replaced by hematite along grain boundaries and crystallographic planes (Fig. 4D). A late generation of pristine magnetite (Type-γ; ~30 modal%) occurs as an overgrowth (Fig. 4A) and as veinlets that crosscut Type-α magnetite (Fig. 4E). In some areas, Type-γ magnetite presents actinolite inclusions (Fig. 4A). Type-δ magnetite (~10 modal%) is subhedral and occurs forming veinlets with minor apatite that crosscut the altered host rock. This magnetite type is characterized by a well-defined cubic cleavage (Fig. 4F) and exsolution lamellae (Fig. 5G) consisting of an unspecific Fe-Mg-Al-O-bearing mineral. Titanite, rutile and an unspecified Mn-silicate occur along the magnetite crystallographic planes. Locally, early magnetite types can be replaced by a Si-rich magnetite (Type-ε; ~10 modal%) with a colloform-banding texture sometimes surrounding small (< 10 μm) pyrite grains (Fig. 4H). Bladed specular hematite (Fig. 4I) is also observed as a late phase intergrown with quartz and magnetite.

4.1.4. El Romeral

At El Romeral, four types of magnetite (Type-I to -IV) were identified (Table 2; Rojas et al., 2018b). Type-I and -II dominate over the other types of magnetite with 35 and 60 modal% abundance, respectively (Rojas et al., 2018b). These magnetite types are similar to Type-1 and −2 from both Los Colorados (Knipping et al., 2015a, 2015b) and Cerro Negro Norte (Salazar et al., 2020) with inclusion-rich cores

Table 5
Data summary of the most relevant trace elements (in ppm) determined by LA-ICP-MS spot analyses in magnetite types from El Laco.

	Cristales Grandes		Rodados Negros		San Vicente Alto		Laco Norte				
	Outcrop		Drill core		Drill core		Outcrop		Drill core		
Element	n	Magnetite-S (N = 118)	n	Magnetite-S (N = 105)	n	Magnetite-S (N = 67)	n	Magnetite-S (N = 29)	n	Magnetite-α (N = 9)	n
Mg	0	4120–14-600 *9141*	0	6100–11-490 *7706*	0	180–8580 *3623*	0	503–148-00 *9795*	0	881–4490 *2534*	0
Al	0	604–6140 *2419*	0	155–3620 *1067*	0	64.4–974 *488*	2	BDL-717 *255*	0	4870–69-60 *6128*	0
Ti	0	99–7650 *2526*	0	60–1840 *452*	0	17.7–350 *173*	21	BDL-191 *125*	0	6540–20-200 *11,537*	0
V	0	1397–21-00 *1781*	0	311–1499 *1104*	0	532–1095 *913*	0	370–842 *578*	0	2580–36-90 *2978*	0
Cr	89	BDL-57.9 *18.7*	94	BDL-30.7 *BDL*	67	BDL-BDL	28	BDL-3.8 *3.8*	4	BDL-42.7 *8.13*	9
Mn	0	411–1420 *857*	0	723–1520 *1055*	0	38.7–746 *336*	0	55.3–496 *278*	0	55.6–186 *115*	0
Co	0	617–154 *105*	0	100–166 *132*	0	78.6–156 *123*	0	60.5–168 *122*	0	141–174 *160*	0
Ni	0	39.9–147 *82.8*	0	96.8–150 *123*	0	175–293 *244*	1	175–253 *220*	0	402–476 *440*	0
Cu	68	BDL-48.2 *13.5*	99	BDL-20.8 *BDL*	34	BDL-93.4 *20.1*	16	BDL-34.3 *12.9*	3	BDL-9.40 *1.93*	16
Zn	0	51.9–201 *130*	0	89.7–266 *154*	0	18.5–95.4 *58.8*	0	15.6–20.2 *47.7*	0	64.2–90.6 *74.1*	0
Ga	0	9.2–47.5 *29.2*	0	6.5–19.4 *11.2*	5	BDL-4.07 *2.48*	5	BDL-5.9 *3.37*	0	29.2–38.5 *34.5*	0
Sn	0	3.6–29.4 *10.7*	0	3.9–8.5 *5.43*	0	2.85–5.64 *3.87*	0	5.72–24.3 *13.1*	0	3.26–6.28 *4.93*	20

	Laco Norte					Laco Sur						
	Drill core					Outcrop + Drill core		Drill core				
Element	Magnetite-β (N = 20)	n	Magnetite-X and -Y (N = 21)	n	Magnetite-Z (N = 14)	n	Magnetite-S (N = 130)	n	Deep (N = 34)	n	Intermediate depths (N = 21)	n	Shallow depth (N = 17)
Mg	5610–10-130 *8125*	0	5750–14-240 *9442*	0	5520–97-40 *7422*	10	BDL-12170 *6747*	0	2570–10-680 *5396*	0	1333–13-270 *5853*	0	6270–9-060 *7464*
Al	5086–63-50 *5864*	0	3660–91-00 *6492*	0	1562–26-70 *2069*	22	BDL-2280 *664*	0	2050–52-80 *3386*	0	1929–21-060 *5803*	0	546–13-48 *849*
Ti	7680–98-70 *8654*	0	2040–52-40 *3363*	0	BDL-2040 *1411*	37	BDL-1165 *255*	0	1790–11-2000 *15,322*	0	3160–10-100 *6099*	0	226–65-3 *406*

(*continued on next page*)

Table 5 (*continued*)

	Laco Norte					Laco Sur							
	Drill core					Outcrop + Drill core		Drill core					
Element	Magnetite-β (N = 20)	n	Magnetite-X and -Y (N = 21)	n	Magnetite-Z (N = 14)	n	Magnetite-S (N = 130)	n	Deep (N = 34)	n	Intermediate depths (N = 21)	n	Shallow depth (N = 17)
V	2690–3400	0	1688–2590	0	1830–2410	0	179–1360	0	1480–2930	0	2400–5810	0	2182–2580
	2957		*2028*		*2159*		*846*		*2129*		*3281*		*2335*
Cr	BDL-10.0	18	BDL-6.8	12	BDL-5.20	128	BDL-3.9	6	BDL-495	9	BDL-151	16	BDL-3.29
	4.69		*BDL*		*BDL*		*3.9*		*68.4*		*35.6*		*3.29*
Mn	441–872	0	313–829	0	122–677	4	BDL-488	0	299–2290	0	93.2–781	0	34.9–432
	607		*562*		*428*		*274*		*753*		*403*		*163*
Co	121–171	0	144–170	0	89.0–162.0	0	24.7–144	0	80.4–137.4	0	41.3–140	0	108–118
	149		*155*		*138*		*101*		*116*		*107*		*112*
Ni	344–428	0	272–338	0	278–350	0	140–319	0	157–354	0	242–492	0	327–371
	392		*306*		*305*		*251*		*300*		*351*		*349*
Cu	BDL-2.68	21	BDL-BDL	14	BDL-BDL	71	BDL-305	13	BDL-48		BDL-10.1	5	BDL-2.81
	BDL		*BDL*		*BDL*		*45.4*		*5.25*		*4.23*		
Zn	65.4–127	0	21.1–112	0	41.5–107	10	BDL-98	0	59.9–183	0	33.3–145	0	30.3–88.7
	93.6		*47.8*		*70.4*		*39.5*		*115*		*73.8*		*48.5*
Ga	39.7–50.5	0	34.2–57.5	0	25.0–30.2	51	BDL-4.3	0	12.8–37.9	0	20.8–37.2	0	6.39–9.93
	45.5		*46.3*		*27.3*		*2.06*		*27.0*		*26.7*		*7.57*
Sn	3.49–5.80	0	4.58–8.10	0	4.03–7.20	0	1.22–124	0	1.88–72.6	0	4.30–397	0	4.58–6.48
	4.56		*6.00*		*5.44*		*11.7*		*8.30*		*32.1*		*5.53*

Notes:
The range indicates the minimum and maximum concentration. The average is shown in italics.
N = number of analyses, n = number of analyses BDL (below the detection limit).
The data correspond to La Cruz et al. (2020).
In order to simplify the data analysis, all surface samples including Type-A, -S1 and -S2 magnetite are reported as Type-S (see Table 2). Trace element concentrations for each type are reported separately in Table SM5.

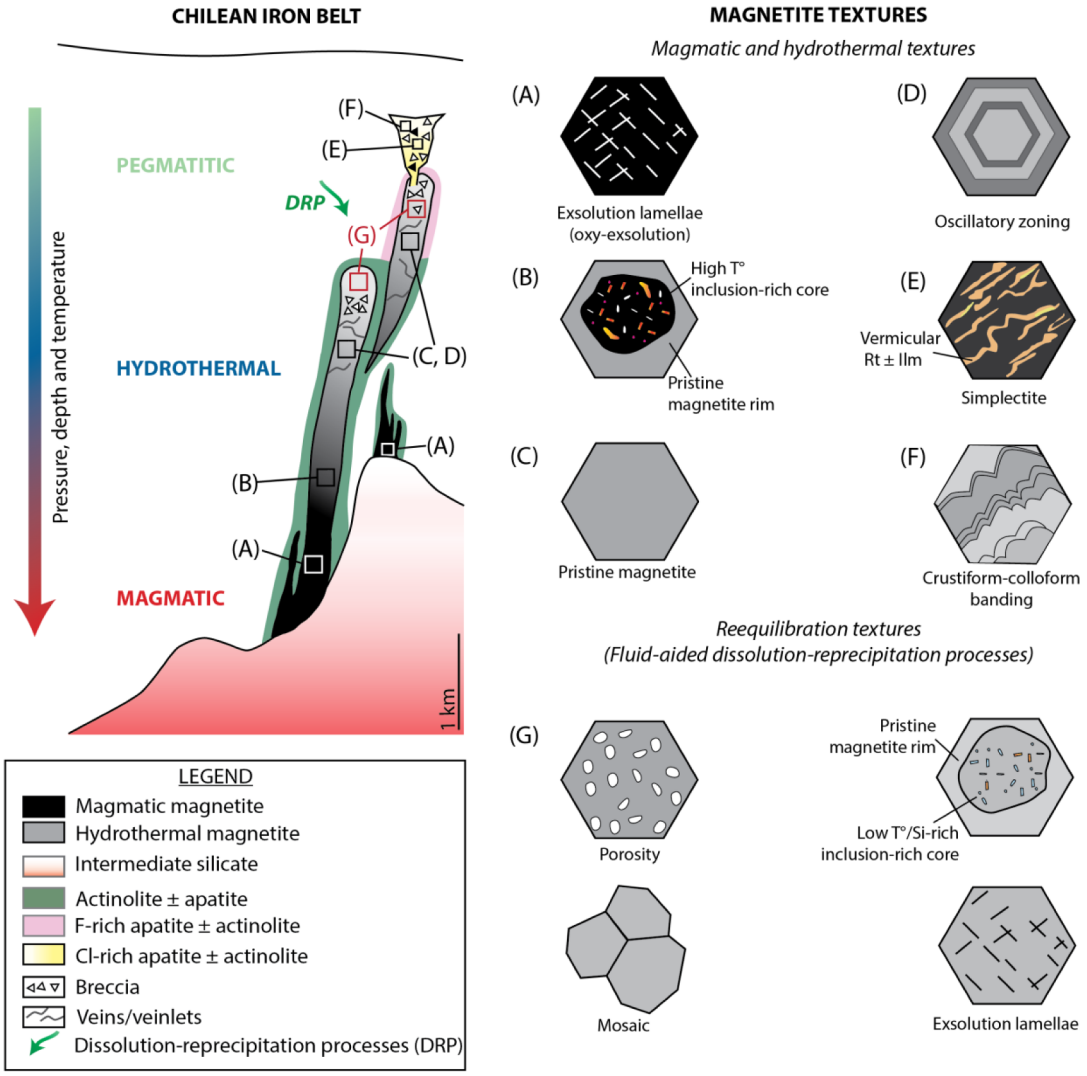

Fig. 10. Schematic figure illustrating representative IOA ore bodies from the Chilean Iron Belt (left). The figure shows the transition from pegmatitic, hydrothermal to magmatic mineralization from shallow levels to depth. Pegmatite-like bodies such as Carmen and Fresia are characterized by hydrothermal magnetite, F-rich apatite and minor actinolite, reflecting the apical and volatile-rich IOA bodies. Breccia pipe types such as Mariela, is characterized by a Cl-rich apatite matrix and magmatic magnetite fragments. In hydrothermal and magmatic-hydrothermal iron bodies the association of magnetite-actinolite becomes more dominant at the deepest parts of the system. IOA bodies are also characterized by breccia and veins/veinlets mineralization. Some iron bodies are affected by multiple dissolution-reprecipitation processes triggered by the infiltration of fluids. Also shown are representative magnetite microtextures in IOA bodies (right; A-G) and their relative location: (A-F) Magmatic and hydrothermal textures; (G) Reequilibration textures. See text for discussion.

(Type-I) surrounded by inclusion-poor rims (Type-II) (Table 2; Fig. 5; Fig. SM5A). Several polycrystalline and one-phase inclusions 50 μm to a few nm in size occur oriented or randomly distributed in magnetite Type-I. The compositions of these inclusions were determined by using SEM-EDS and micro-Raman spectroscopy. In magnetite samples from El Romeral, inclusions > 10 μm were identified as actinolite, ilmenite and rutile, whereas smaller inclusions correspond to rutile, ilmenite, titanite, chlinoclore, calcite, phlogopite, tremolite, NaCl and pargasite (Rojas et al., 2018b). At shallow depths (< 100 m), Si-rich inclusions occur aligned along magnetite crystallographic planes. The El Romeral samples studied here (samples Rom-094, ~347 m; Rom-149, ~10 m) are texturally different. In sample Rom-094, magnetite Type-I predominates over Type-II, whereas at shallow depths (sample Rom-149) Type-II predominates over Type-I (Fig. 5) and can occur associated with pyrite and chalcopyrite filling fractures in the magnetite. Type-III magnetite is represented by an inclusion-poor chemically-zoned magnetite. A late magnetite vein event (Type-IV) was identified and crosscuts all previous magnetite types (Rojas et al., 2018b).

4.2. Magnetite chemistry

The new EPMA data from, Carmen, Fresia, Mariela and El Romeral (sample Rom-149) are reported in Tables SM2 and SM3. A statistical summary of EPMA analyses (Mg, Al, Si, Ca, Ti, V, Mn, Fe and O) for each magnetite type identified in Carmen, Fresia, Mariela (this study); El Romeral (this study and Rojas et al., 2018b); Los Colorados (Knipping et al., 2015a, 2015b; Deditius et al., 2018); Cerro Negro Norte (Salazar et al., 2020); and El Laco (Ovalle et al., 2018) is reported in Table 3.

The concentration of trace elements was determined by using LA-ICP-MS in the most abundant magnetite types from El Romeral (Type-I and -II; samples Rom-094 and Rom-149), Carmen (Type-I, -II and -III), Fresia (Type-A, -B and -C), and Mariela (Magnetite-α, -β, -γ and -δ). A total of 430 analyses for 34 elements, e.g., Na, Mg, Al, Si, P, K, Ca, Sc, Ti, V, Cr, Mn, Co, Ni, Cu, Zn, Ga, Ge, Rb, Sr, Y, Zr, Nb, Mo, Ag, Cd, Sn, Sb, Ba, La, Ce, Pb, Th and U were carried out. All LA-ICP-MS data are reported in Tables SM6 and SM7. A summary of all analyzed trace elements from Los Colorados (Knipping et al., 2015b), Cerro Negro

Norte (Salazar et al., 2020), and El Laco (Broughm et al., 2017, La Cruz et al., 2020) are reported in Table SM4. It should be noted that the LA-ICP-MS data correspond to spot analyses with the exception of Los Colorados in which transects or profiles in magnetite were performed (Knipping et al., 2015b). Minimum, maximum and average concentrations for each of these elements found in the most relevant magnetite types are reported in Table 4.

The main features of the magnetite chemical compositional dataset from Andean IOA deposits are outlined below.

4.2.1. Carmen, Fresia and Mariela

4.2.1.1. WDS X-ray maps. Elemental (Fe, Mg, Ca Si, Al, Ti, Mn and V) WDS X-ray maps for magnetite grains from Carmen, Fresia and Mariela are shown in Figs. 6–8, respectively. These maps correspond to representative magnetite textures identified and illustrated in Figs. 2–4, i.e., Type-I magnetite from Carmen; Type-A and -C magnetite from Fresia; Type-α and -γ magnetite from Mariela.

Type-I magnetite from Carmen (Fig. 6) exhibits a distinct oscillatory zoning of Mg, Si and Al, which is less pronounced for Fe. Magnesium, Si and Al form particles in the dark bands of Type-I magnetite. Both Ca and Ti are homogeneously distributed, with no oscillatory zoning and only a few, micro-particles with Ca and Ti. A thin magnetite veinlet (Type-II) crosscuts Type-I magnetite, and is more depleted in Mg, Si and Al and slightly more enriched in Fe than Type-I magnetite.

In magnetite grains from Fresia, a distinct oscillatory zoning for Mg, Ca, Si and Al but less pronounced for Fe and Ti is observed in Type-A magnetite (Fig. 7A). Magnesium, Al, Si and Fe also occur forming abundant particles, whereas Ca-Ti-bearing particles are scarce. On the other hand, a pronounced oscillatory zoning of Mg, Ca and Si, and a less distinct for Fe is observed in Type-C magnetite (Fig. 7B). Both Al and Ti WDS X-ray elemental maps are consistent with low Al and Ti concentrations (0.01–0.02 wt%), which are close to the detection limit (Table 3). Aluminum appears slightly enriched in some fractures in Type-C magnetite.

WDS maps of magnetite grains from Mariela reveal the elemental distribution related to the symplectite texture observed in these samples (Fig. 8). In particular, Types-α and -γ magnetite show similar concentrations of Fe, but Type-α is more enriched in Ca, Al, Si, Ti and V than Type-γ. High concentrations of Ca, Mg, Si and Al in Type-γ magnetite are related to silicate particles and microfracture fillings. It should be noted that the vermicular Fe and Ti oxide minerals (rutile, titanite and ilmenite) that are intergrown with Type-α magnetite forming the symplectite, are depleted in Fe, Mg and V, and slightly enriched in Ca, Si Al, Ti and Mn. Specifically, the Ca-rich domains and the Mn-rich particles within the vermicular Fe-Ti oxide mineral phases are related to titanite and ilmenite, respectively.

4.2.1.2. EPMA and LA-ICP-MS spot analyses.

EPMA data for magnetite from Carmen, Fresia and Mariela are presented in Table 3 and a statistical summary of trace element concentrations (Mg, Al, Ti, V, Cr, Mn, Co, Ni, Cu, Zn, Ga and Sn) determined by LA-ICP-MS for each deposit is presented in Fig. 9.

The major compositional variations occur for Mg, Al, Si, Ca, Ti, V, Fe and Mn, whereas Sc, Cr, Zn and Nb concentrations are below or close to the detection limit (Table 3; Table SM2). For some magnetite types (Fresia: Type-A and -D; Mariela: Type-α,- β, -γ and -δ), totals are relatively low (~95% on average) probably related to the presence of numerous micropores associated with dissolution-reprecipitation processes (Fresia) and the occurrence of Ti-Fe oxides exsolution lamellae from titano-magnetite (Mariela). For magnetite types characterized by oscillatory zoning (Carmen: Type-I; Fresia: Type-A and -C) analyses were carried out on both light and dark BSE bands (Table 3).

For the Carmen deposit, EPMA analyses reveal that magnetite Type-I has the highest average concentration of Mg and Ca of all magnetite types in this deposit (Table 3). The maximum and average concentrations of Mg, Al, Si and Ca are higher in the dark BSE bands than in light BSE bands. The higher concentrations of Ca detected in the dark BSE bands (average 0.07 wt%) compared to light BSE bands (average 0.04 wt%) are probably due to the presence of some Ca-bearing particles. Titanium, Fe and Mn concentrations are similar between dark and light BSE bands. The Ti concentration is low (average 0.07 wt%; Table 3) in both dark and light BSE bands. On the other hand, Type-III and -IV magnetite have a higher Ti concentration (average 0.08–0.14 wt%) than both Type-I and-II (average 0.07 wt%). It should be noted that V is homogeneously distributed throughout all magnetite types (average 0.23–0.25 wt%). LA-ICP-MS analyses reveal that Type-I magnetite has the highest average Mg and Al concentration, i.e., 3,842 and 1,036 ppm, respectively, followed by Type-II magnetite (average 2,811 ppm Mg; 744 ppm Al) and Type-III (average 965 ppm Mg; 560 ppm Al) (Table 4). Gallium displays the same distribution between the different magnetite types (Type-I > Type-II > Type-III), but variations in concentration are not significant (average values between 33.4 and 38.5 ppm). Titanium, V, Co and Ni show similar concentrations in Type-I and -II magnetite, whereas Type-III has a wide range of concentrations of Ti, V and Co than Type-I and -II. Manganese concentrations are higher in Type-III magnetite (average 1,077 ppm).

In Fresia, Type-A and -C magnetite are characterized by oscillatory zoning (Fig. 3A,B,D,E) in which dark BSE bands are more enriched in Mg, Al, Si and Ca than light bands (Table 3). In addition, Ti concentrations are detectable in dark BSE bands of Type-A magnetite (average 0.22 wt%), whereas for Type-C magnetite, Ti is below the detection limit (< 0.06 wt%). LA-ICP-MS analyses of Type-A magnetite show high concentrations of Mg and Ga, i.e., 2,214 and 35 ppm on average, respectively, whereas the Type-C variety contains the lowest concentrations of Al, Ti, V, Ni and Ga, but the highest concentrations of Co (average 34.3 ppm) and Cu (average 17.8 ppm) in comparison with all other magnetite types from Fresia. Finally, Type-B magnetite grains display the highest concentrations of Al, Ti, V, Mn and Ni (average: 1,824 ppm Al; 2,921 ppm Ti; 1,756 ppm V; 559 ppm Mn; 260 ppm Ni; Table 4).

Magnetite from Mariela is characterized by a high concentration of V (up to 2.28 wt%; Table 3) and Ti (up to 0.98 wt%, Table 3). The V concentrations reported for Mariela magnetite grains are the highest reported for any Andean IOA deposit, whereas Ti concentrations are the second highest after some magnetite types from El Laco (Magnetite-α and Magnetite-β, -β1, -β2; Ovalle et al., 2018) (Tables 3 and 5; Fig. 9). LA-ICP-MS and EPMA analyses yielded contrasting results for Ti and V (Tables 3 and 4). The highest Ti and V concentrations determined by EPMA were found in Type-α magnetite (Table 3), whereas LA-ICP-MS data showed the highest concentrations in Type-β magnetite (Table 4). These differences are probably due to the presence of Fe-Ti oxides exsolution lamellae (Fig. 4D) and nano-inclusions in Type-β magnetite that were most likely affected by the large spot size of the laser (~40 μm spot diameter). In addition, LA-ICP-MS analyses revealed that Type-α magnetite has the highest concentration of Cr and Mn (51.2 ppm Cr and 8,400 ppm Mn; Table 4) reported so far for Andean magnetites. It should be noted that together with El Laco, Mariela is the only IOA deposit studied here that shows detectable concentrations of Cr in magnetite (Table 4). Type-γ magnetite has the lowest average concentration of Ti, V and Al, but the highest content of Co and Cu. Copper concentrations in magnetite are much higher than in any other deposit studied here, reaching concentrations up to ~1,620 ppm in this magnetite type (Table 4). Gallium contents are similar between the different magnetite types (~40 ppm on average), but Type-δ magnetite contains slightly higher concentrations (average 48.5 ppm). EPMA analyses of Fe-Ti oxides including rutile, titanite and minor ilmenite, which are intergrown with magnetite Type-α of the symplectite are presented in Table SM4.

4.2.2. Los Colorados

EPMA analyses reported by Knipping et al. (2015a) and Knipping et al. (2015b) reveal that magnetite cores (Type-1) are enriched in Ti, V,

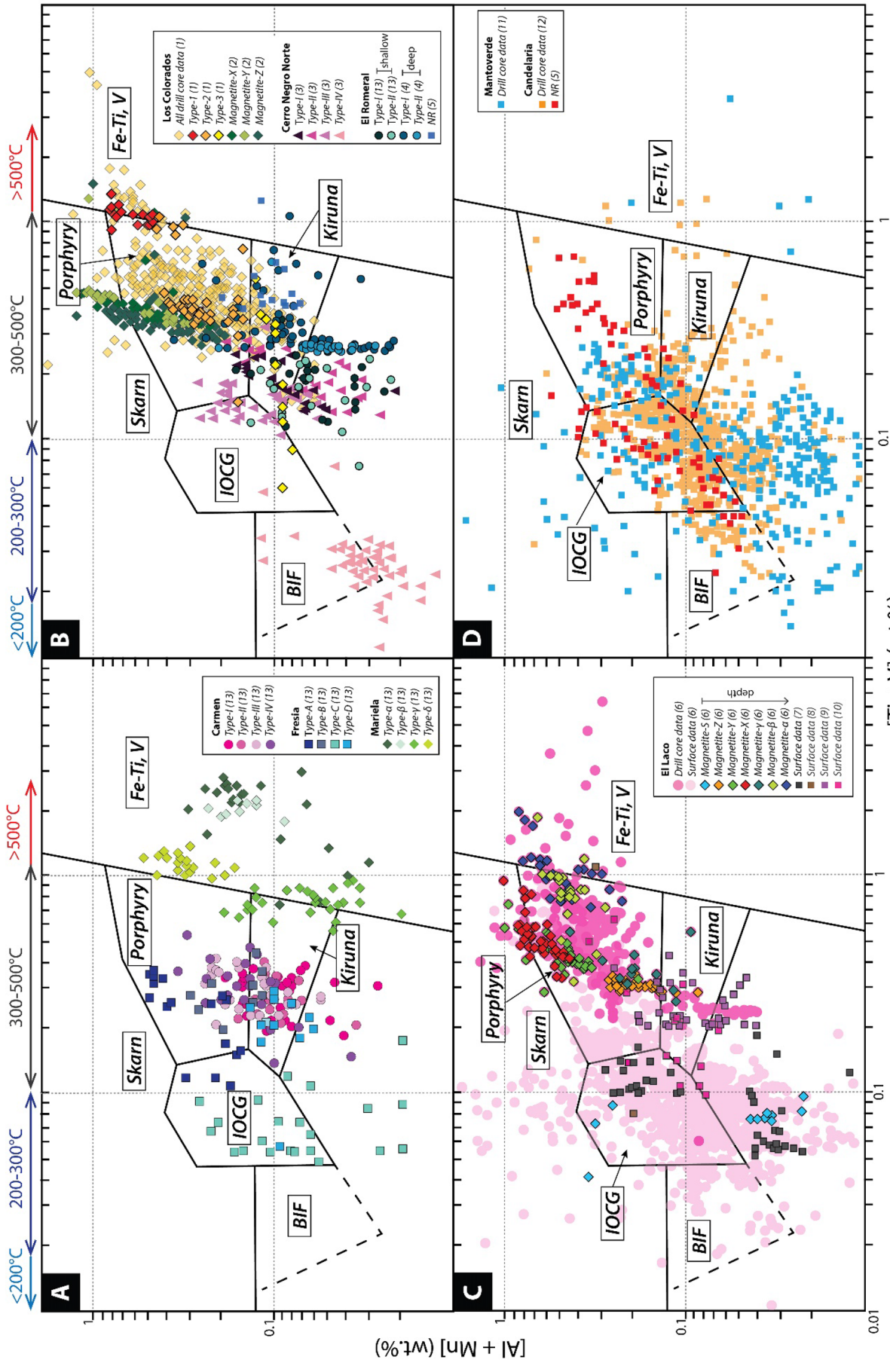

Fig. 11. Chemical discrimination diagram after Dupuis and Beaudoin (2011) and modified by Nadoll et al. (2014) for all magnetite types from Andean IOA deposits and the Candelaria and Mantoverde IOCG deposits. (A) Carmen, Fresia and Mariela; (B) Los Colorados, Cerro Negro Norte and El Romeral; (C) El Laco; (D) Candelaria and Mantoverde. Data source: (1) Knipping et al. (2015a) and Knipping et al. (2015b); (2) Deditius et al. (2018); (3) Salazar et al. (2020); (4) Rojas et al., (2018b); (5) Huang and Beaudoin (2019); (6) Ovalle et al. (2018); (7) Broughm et al. (2017); (8) Velasco et al. (2016); (9) Dare et al. (2015); (10) Nyström and Henríquez (1994); (11) Simon et al. (2018); (12) Rodriguez-Mustafa et al. (2020); (13) This study; ND (not determined).

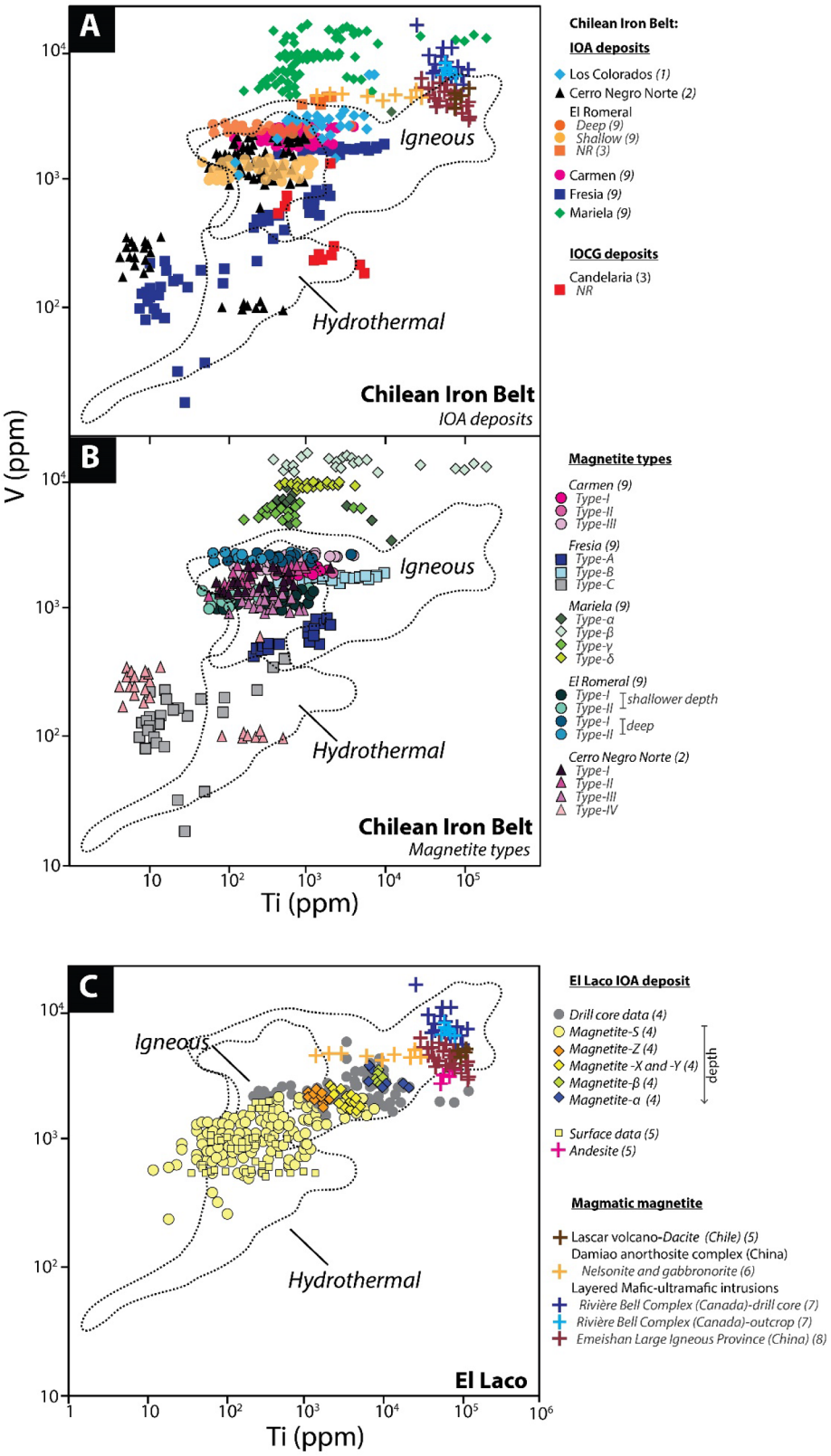

Fig. 12. Concentration of Ti vs. V in magnetite from (A) Chilean Iron Belt (per deposit); (B) Chilean Iron Belt (magnetite types from Carmen, Fresia, Mariela, El Romeral and Cerro Negro Norte) and (C) El Laco. Magmatic magnetite data from the literature is also shown. The igneous and hydrothermal fields are from Nadoll et al. (2014). Note the overlapping area between the igneous and hydrothermal field. Data source: (1) Knipping et al. (2015a) and Knipping et al. (2015b); (2) Salazar et al. (2020); (3) Huang and Beaudoin (2019); (4) La Cruz et al. (2020); (5) Broughm et al. (2017); (6) He et al. (2016); (7) Polivchuk (2017); (8) Liu et al. (2014); (9) This study. ND (not determined).

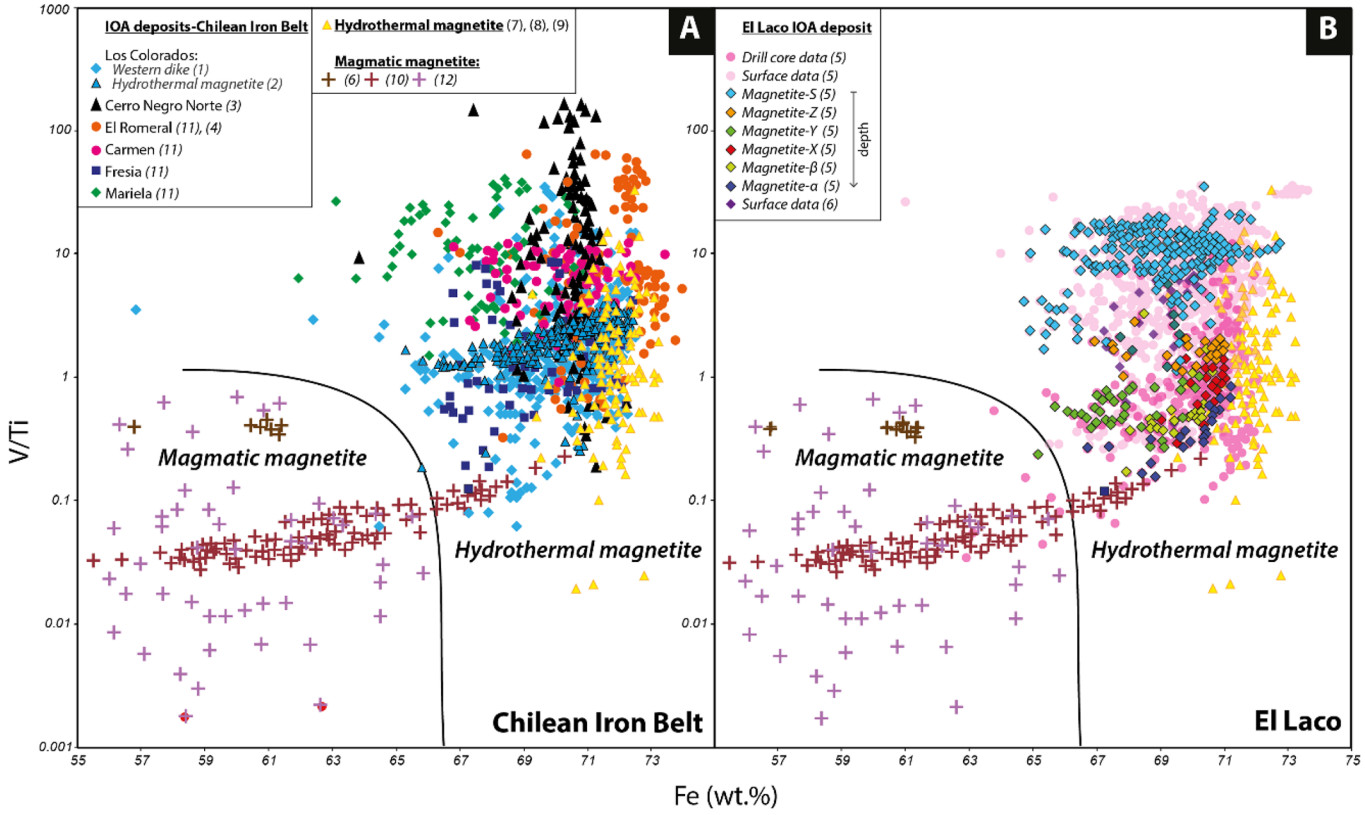

Fig. 13. Fe vs. V/Ti discrimination diagram (Wen et al., 2017) for the Chilean Iron Belt (A) and El Laco (B). Data from magmatic and hydrothermal magnetite reported in the literature are also plotted. Data source: (1) Knipping et al. (2015a) and Knipping et al. (2015b); (2) Deditius et al. (2018); (3) Salazar et al. (2020); (4) Rojas et al. (2018b); (5) Ovalle et al. (2018); (6) Broughm et al. (2017); (7) Nadoll (2011); (8) Nadoll et al. (2014); (9) Nadoll et al. (2015); (10) Liu et al. (2014); (11) This study; (12) References of igneous data in Wen et al. (2017).

Al and Mn (average: 0.44 wt% Ti; 0.62 wt% V; 0.48 wt% Al; 0.14 wt% Mn) in comparison with magnetite rims (Type-2 and −3) (average: ≤0.12 wt% Ti, ≤0.35 wt% V, ≤0.17 wt% Al, ≤0.12 wt% Mn; Table 3). Notably, X-ray maps of magnetite from the massive magnetite ore body display a clear Ti zonation with a Ti-rich, inclusion-rich core (Type-1), a Ti-poor transition zone (Type-2), and an inclusion-free rim depleted in Ti (Type-3) (Fig. SM7A). LA-ICP-MS traverses and elemental X-ray maps also reveal that magnetite cores (Type-1) are enriched in Si-, Al-, Mn- and Mg-bearing inclusions (Knipping et al., 2015a, 2015b). On the other hand, late-stage hydrothermal magnetite veinlets, i.e., Type-X, -Y and -Z, have a similar chemical composition and lower concentrations of Mg, Al, Si, Ti, V and Mn, with average values that vary between 0.23 and 0.3 wt% Mg, 0.42–0.48 wt% Si, 0.14–0.27 wt% Ti, 0.23–0.26 wt% V, and 0.07–0.2 wt% Mn (Deditius et al., 2018; Table 3) than the massive magnetite body (All data, Type-1 and -2; Table 3). Trace element concentrations in magnetite Type-3 are slightly lower than concentrations in Magnetite-X and -Z (Table 3). The major difference between Magnetite-X, -Y and -Z is the Ti concentration, with Magnetite-Y having the highest contents (average: 0.14 wt% Ti for Magnetite-X, 0.27 wt% Ti for Magnetite-Z and 0.15 wt% Ti for Magnetite-Z; Table 3). Elemental (Al, Si, Ca, Ti, Mn and Mg) X-ray maps for Magnetite-Z reveal an oscillatory zoning with alternating element-rich and depleted bands. In particular, Ti is present as Ti-rich particles in element-depleted bands but is homogeneously distributed in some enriched bands (Deditius et al., 2018; Fig. SM7B).

4.2.3. El Romeral and Cerro Negro Norte

In general, magnetite grains from El Romeral (Type-I and -II; Rojas et al., 2018b and this study) and Cerro Negro Norte (Types I–IV; Salazar et al., 2020) and contain lower concentrations of trace elements than magnetite from Los Colorados (Knipping et al., 2015a, 2015b) (Fig. 9; Table 3).

EPMA analyses of magnetite from El Romeral (Table 3) reveal that Type-I has higher concentrations of Si and Ca than Type-II in the deep sample (~347 m; Rojas et al., 2018b), whereas the concentrations of Mg, Al, Si, Ca, Ti, V and Mn are very similar in both types in the shallow sample (~10 m; this study). Notably, the V concentration is similar in Type I and Type II magnetite, both in the shallow (average 0.15 wt%) and deep sample (average 0.26 wt%). On the other hand, LA-ICP-MS analyses show that Mg, Al, V, Co and Ga concentrations are higher at depth than at shallow levels, whereas Mn, Ni and Zn are higher in the shallow sample (Table 4). Overall, both at depth and at shallow levels, Mg, Al and Ti average concentrations are higher in Type-I than in Type-II magnetite; Zn and Mn average concentrations are similar, but slightly higher in Type-I than in Type-II; Ni concentrations are slightly higher in Type-II, and Co and V concentrations are similar in Type-I and -II.

Most of the EPMA magnetite analyses from Cerro Negro Norte were below the detection limit with the exception of Fe, V, Si and Al (Table 3). Notably, both Type-I and -II magnetite have similar and higher concentrations of V (average 0.21 wt%), but lower Si (average 0.09 wt%), when compared to Type-III and -IV magnetite (0.13 wt% V and 0.20 wt% Si on average). The WDS X-ray maps revealed that Type-I magnetite (inclusion-rich cores) is enriched in Mg, Al, Ca, Mn and Ti relative to Type-II magnetite (rims) (Salazar et al., 2020; Fig. SM7C). LA-ICP-MS analyses showed that Type-I magnetite displays the highest concentrations of Mg, Mn, Zn and Ga (average: 1,405 ppm Mg, 134 ppm Mn, 12.1 ppm Zn and 39.2 ppm Ga) (Table 4 and Table SM5); Type-I and -II magnetite contain similar concentrations of Ni and Co (96.2 ppm Ni and 25.7 ppm Co; 99 ppm Ni and 25.5 ppm Co, respectively). Type-III magnetite has the highest concentration of Cu (average 41.7 ppm Cu), whereas Type-IV magnetite has the lowest concentrations of Ti, V, Al, Mn, Zn and Ga (average values: 72,8 ppm Ti, 215 ppm V, 280 ppm

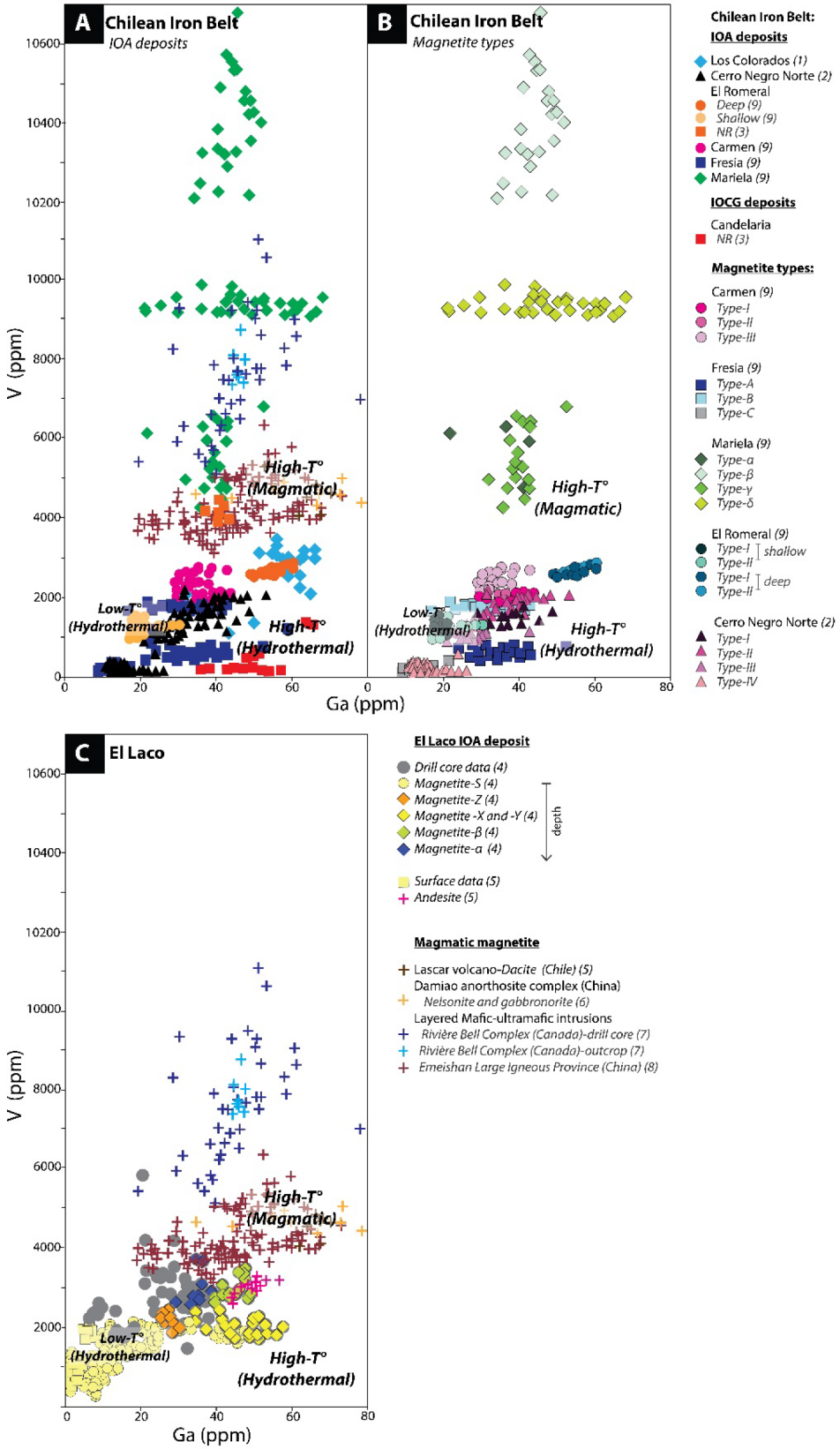

Fig. 14. Concentration of Ga vs. V in magnetite from (A)Chilean Iron Belt (per deposit); (B) Chilean Iron Belt (magnetite types from Carmen, Fresia, Mariela, El Romeral and Cerro Negro Norte) and (C) El Laco. Data source: (1) Knipping et al. (2015a) and Knipping et al. (2015b); (2) Salazar et al. (2020); (3) Huang and Beaudoin (2019); (4) La Cruz et al. (2020); (5) Broughm et al., (2017); (6) He et al. (2016); (7) Polivchuk (2017); (8) Liu et al. (2014); (9) This study. ND (not determined). See text for discussion.

Al, 82.4 ppm Mn, 7.9 ppm Zn and 15.3 ppm Ga), but the highest in Ni and Co (average: 105 ppm Ni and 21.9 ppm Co). It should be noted that the average concentrations of Ti are similar in Type-I, -II and -III magnetite (~330 ppm Ti), but Type-I has the highest Ti concentration (up to ~1,990 ppm; Table 4).

4.2.4. El Laco

The EPMA data in surface and drill core samples from El Laco Norte (Table 3) reported by Ovalle et al. (2018) reveal that Ti, V and Al concentrations increase with depth (Magnetite-S < −Z < −X < −Y < −γ < −α < −β, −β1, −β2; Fig. SM6). Manganese concentrations are low, close to the detection limit (average 0.01–0.04 wt %), and decrease slightly with depth (Ovalle et al., 2018). It should be noted that Ti concentrations in Magnetite-α (average 0.76 wt%) and Magnetite-β, -β1, -β2 (average 0.57 wt%) are among the highest reported so far in Andean IOA deposits (Table 3).

La Cruz et al. (2020) performed LA-ICP-MS in magnetite samples from the different magnetite ore bodies from El Laco including Cristales Grandes, Rodados Negros, San Vicente Alto, Laco Norte and Laco Sur.

LA-ICP-MS analyses from Laco Norte reveal that Ti, V and Cr concentrations increase with depth and where the highest concentrations are found in Type-α and -β magnetite (Table 4). Manganese is highest in Type-β magnetite, and is higher in Type-X and -Y than in Type-α magnetite (Table 5). The highest Al concentration was found in Type-X and -Y, followed by Type-α, -β and -Z magnetite. The highest Ga concentration was determined in Type-X, -Y and -β, followed by -α and -Z. The Co concentration is consistent in all magnetite types ranging from 105 to 160 ppm on average. At Laco Sur, LA-ICP-MS analyses were performed on samples from different depths (surface, shallow level, intermediate depth, and deep; Table 5). The results show that Ti, Cr, Mn and Zn increase progressively with depth, while the highest Al and V concentrations occur at intermediate depths. Magnesium increases towards the surface and the average Ga concentration is similar between the intermediate and deep levels. However, the highest Ga concentration was measured in magnetite from the deepest samples (27 ppm on average).

5. Discussion

5.1. Magnetite microtextures and their link to physico-chemical processes

Previously published data and new analyses from Andean Kiruna-type IOA deposits show a wide variety of magnetite textures (Figs. 2–5, SM4, SM5, SM6; Table 2). The observed microtextures, chemical zoning and distribution of various mineral inclusion types (Table 2) provide evidence of the geological processes involved in the formation and evolution of these deposits. We stress that a detailed textural characterization of magnetite grains must be undertaken in order to avoid misinterpretations of the geochemical dataset. Key aspects include a precise determination of the magnetite paragenesis in each deposit, and a careful evaluation of chemical zoning features and the presence of micro- to nano-sized mineral inclusions. Furthermore, the effects of hydrothermal overprinting are critical to evaluate the impact of re-equilibration processes on the composition of primary magnetite.

A schematic representation of IOA ore bodies from the Chilean Iron Belt showing a vertical zonation from deep to shallow formation conditions is shown in Fig. 10. Observed magnetite microtextures for each zone or IOA subtype, i.e., pegmatitic (e.g., Carmen, Fresia and Mariela; Palma et al., 2019), hydrothermal (e.g., Cerro Negro Norte; Salazar et al., 2020) and magmatic (e.g., Los Colorados; Knipping et al., 2015a, 2015b) are also presented. The microtextural styles described for the Laco Norte IOA deposit is presented in Fig. SM6 (Ovalle et al., 2018). A description and interpretation of the observed microtextures is presented below.

5.1.1. Mineral inclusions

Different types of mineral inclusions, both oriented and randomly distributed, single or polycrystalline, were identified in the studied IOA deposits (Table 2). The massive magnetite ore in Los Colorados, Cerro Negro Norte and El Romeral is characterized by magnetite grains with inclusion-rich cores surrounded by pristine, inclusion-poor or inclusion-free rims (Fig. 5; 10B; SM4A; SM5A,B). The magnetite cores, usually interpreted as magmatic in origin and labeled as Type-1, contain numerous polycrystalline mineral inclusions. In Los Colorados, Type-1 magnetite inclusions include Mg-rich clinopyroxene, magnetite, titanite and an unknown Mg-Al-Si-phase, all of them interpreted as formed at high-temperatures based on the temperature at which some inclusions re-homogenize to silicate melt (> 950 °C) (Knipping et al., 2015b, 2019b). At El Romeral, on the other hand, mineral inclusions of Ti-pargasite were identified in the magnetite inner cores, while titanite, rutile, ilmenite and clinochlore were identified as inclusions in the outer portions of the magnetite cores (Rojas et al., 2018b). Both pargasite and clinochlore breakdown at ~200 MPa, suggest formation temperatures between 800 and 1020 °C for the magnetite inner cores and < 780 °C for the outer cores (Jenkins, 1983; Staudigel and Schreyer, 1977).

It is likely that the presence of high-temperature mineral inclusions indicates a high formation temperature for the magnetite host if both were formed at the same time. However, Rojas et al. (2018b) interpreted that the Si-rich (α-quartz) inclusions, aligned along magnetite crystallographic planes in shallow samples at El Romeral may indicate exsolution processes related to slow cooling rates. The presence of Si-rich inclusions may be relevant because most Si-rich domains in magnetite have been attributed to the presence of Si in solid-solution and/or small silicate inclusions (Newberry et al., 1982; Huberty et al., 2012). However, those authors did not rule out the hydrothermal crystallization of quartz along microfractures and/or as inclusions during cooling. More recently, Huang and Beaudoin (2019) studied a few deep magnetite samples from El Romeral and described inclusion-rich cores with abundant quartz, chlorite, albite, titanite and chalcopyrite mineral inclusions, mainly of hydrothermal origin, that formed after magnetite crystallization. They suggest that a fluid-assisted alteration mechanism could explain the incorporation of cations with a small ionic radius (e.g., Si^{4+}) within magnetite (Hu et al., 2014). It follows that a part of the pristine, inclusion-free magnetite rims could be formed by dissolution and reprecipitation of inclusion-rich magnetite (Huang and Beaudoin, 2019; Fig. 10G).

In addition, inclusion-rich magnetite cores from Cerro Negro Norte are dominated by actinolite, an unspecified Mg-Al-Si phase, rutile, ilmenite, clinopyroxene, orthopyroxene, titanite and chlinoclore (Salazar et al., 2020). Many of these mineral inclusions were also observed in magnetite from the El Romeral deposit (Rojas et al., 2018b). However, inferring the temperature of formation of the magnetite host based on the presence of mineral inclusions must be performed with caution because some of these inclusions could have been incorporated (or exsolved) at a lower temperature and hence, not necessarily represent the temperature conditions at which magnetite crystallized.

5.1.2. Oscillatory zoning and colloform banding

Oscillatory zoning textures, characterized by alternating trace element-rich and trace element-poor bands separated by sharp compositional boundaries (Fig. 10D) were observed in magnetite grains from Los Colorados (magnetite from the diorite intrusion and Magnetite-Z; Knipping et al., 2015a, 2015b; Deditius et al., 2018; Fig. SM4D), Carmen (Type-I; Fig. 2B,C), Fresia (Type-A and -C; Fig. 3B,E) and El Laco (Magnetite-Y; Ovalle et al., 2018; Fig. SM6C). Oscillatory textures have been also described in Si-rich magnetite from hydrothermal Fe skarns (Shimazaki, 1998; Dare et al., 2014; Hu et al., 2014) and in many other mineral phases such as sulfides, oxides, halides, carbonates and phosphates in various ore-forming environments (e.g., Shore and Fowler, 1996; Deditius et al., 2009; Reich et al., 2013; Tardani et al.,

2017). In the particular case of sulfide minerals, oscillatory textures are interpreted to reflect crystallization from fluids of fluctuating elemental composition, for instance, related to periodic influxes of magmatic vapor (e.g., Reich et al., 2013) and/or compositional changes in the fluid driven by tectonically induced decompression and boiling (e.g., Peterson and Mavrogenes, 2014; Román et al., 2019; Sanchez-Alfaro et al., 2016).

Locally, Type-C magnetite from Fresia exhibits crustiform-colloform banding (Figs. 3D; 10F), whereas Si-rich Type-ε magnetite from Mariela displays colloform banding textures (Fig. 4I). These textures have been interpreted in the literature as related to open fissures or fluid-filled voids and formation at relatively low temperatures, possibly < 250 °C (Morrison et al., 1990; Moncada et al., 2012). Thus, the occurrence of oscillatory zoning is consistent with magnetite growth during fluctuating fluid compositions or under a changing physico-chemical regime (Craig and Vaughan, 1981; Shimazaki, 1998; Holten et al., 2000), whereas colloform textures are possibly related to formation under low temperature and steady physico-chemical conditions.

5.1.3. Re-equilibration textures

Several magnetite grains from Carmen (Type-III and -IV), Fresia (Type-C and -D) and El Laco (Magnetite-X) show microtextural evidence of re-equilibration, most likely due to dissolution-reprecipitation processes (DRP) (Table 2; Fig. 10G, SM6C). Re-equilibration processes in magnetite have been reported in skarns (Hu et al., 2014, 2015; Yin et al., 2017), IOA deposits (Heidarian et al., 2016), banded iron formation (Araújo and Lobato, 2019) and in hydrothermally altered igneous magnetite from granitic plutons (Wen et al., 2017). It has been widely reported that textures and the trace element composition of primary and hydrothermal magnetite could be significantly modified by various stages of re-equilibration (Hu et al., 2014, 2015; Heidarian et al., 2016; Wen et al., 2017; Yin et al., 2017; Huang et al., 2018; Huang and Beaudoin, 2019).

Both the porosity of magnetite grains from Carmen and Fresia (Figs. 2F; 3A,F; 10G), and the sinuous and reabsorbed edges in Magnetite-X from El Laco (Fig. SM6C) are key features of DRP (Putnis, 2009). In addition, Ti originally dissolved in magnetite, can form secondary titanite or rutile by DRP. Fluoride has been shown to effectively mobilize Ti in a fluid and consequently, Ti should not always be regarded as immobile in geological fluids (e.g., Audétat and Keppler, 2005; Tanis et al., 2016). Abundant titanite fractures are recognized in magnetite grains from Carmen, Fresia and Mariela, in which these fractures provide conduits for hydrothermal fluids and could accelerate the dissolution-reprecipitation processes in magnetite.

Some magnetite grains from Carmen and Fresia also display a mosaic texture characterized by well-defined 120° triple junctions (Figs. 2D; 3F; 10G). A mosaic texture is also evidence of textural re-equilibration, resulting from the annealing and recrystallization of magnetite (Ciobanu and Cook, 2004; Nold et al., 2013; Huang and Beaudoin, 2019). It has been proposed that the mosaic texture could be formed by fluid-assisted recrystallization process in an open system in skarns (Hu et al., 2015) or by the simultaneous recrystallization and annealing of inclusion-rich magnetite in IOCG and IOA deposits (Huang and Beaudoin, 2019).

Textural and geochemical evidences of DRP are also recorded in apatite grains from Carmen and Fresia including high porosity, a sharp replacement front between F-rich (magmatic) and Cl-rich (hydrothermal) apatite domains, and the formation of secondary monazite inclusions (Palma et al., 2019). The infiltration of mixed basinal brines and meteoric waters that already dissolved evaporites could trigger dissolution-reprecipitation reactions in magnetite from skarns (Hu et al., 2014, 2015; Huang et al., 2018) and IOA deposits (Heidarian et al., 2016). Accordingly, these externally derived fluids could contribute to an increase in salinity and Cl^- contents of late fluids, enhancing Fe solubility and consequently leading to disequilibrium between the precipitated magnetite and evolving fluids (Chou and Eugster, 1977; Ilton and Eugster, 1989).

5.1.4. Exsolution lamellae and symplectite textures

Both exsolution lamellae and symplectites of Fe-Ti oxides are common textures in Ti-rich magnetite from magmatic Fe-Ti,V deposits and mafic–ultramafic igneous rocks (Buddington and Lindsley, 1964; Frost and Lindsley, 1991; Pang et al., 2008, 2010; Wang et al., 2008; Song et al., 2013; Liu et al., 2015; Tan et al., 2015; Tan and Liu, 2016).

Well-developed exsolution lamellae are observed in Type-B magnetite (Fresia; Fig. 3C), Type-β and -δ (Mariela; Fig. 4D,G) and Magnetite-α (El Laco; Fig. SM6F). The composition of these lamellae was only determined in Type-β magnetite (ilmenite-ulvöspinel) and Magnetite-α (ilmenite) by using SEM and LA-ICP-MS analyses due to the small size (< 10 μm) of these exsolution lamellae. The exsolution of different Fe-Ti oxides are indicative of the physico-chemical conditions of the host Ti-rich magnetite and of the different mechanisms of formation (Buddington and Lindsley, 1964; Lattard, 1995; Mücke, 2003; Tan and Liu, 2016). The composite ilmenite-ulvöspinel exsolution lamellae observed in Type-β magnetite (Fig. SM8) suggest that the exsolution was probably controlled by oxidation of an original magnetite-ulvöspinel solid solution during cooling. At relatively oxidizing conditions, the ulvöspinel component in the ulvöspinel-magnetite solid solution (SS) series could be oxidized at a temperature < 600 °C (SS solvus) and exsolved directly as ilmenite (Buddington and Lindsley, 1964). The ilmenite lamellae are also possibly formed by the direct exsolution from cation-deficient $spinel_{SS}$ through the substitution of Fe^{2+} by Ti^{4+} at low oxygen fugacity and high-temperature conditions or the subsolidus re-equilibration of coexisting Fe-Ti oxides (Tan and Liu, 2016).

Hu et al. (2015) reported that during the main stage of mineralization in iron skarn deposits, Ti-bearing magnetite (up to 1.27 wt% Ti) originally formed at high-temperatures under relatively reducing conditions was subsequently re-equilibrated through exsolution lamellae of Fe-Ti-Al-oxides in response to increasing fO_2 and decreasing temperatures. We interpret the exsolution lamellae in magnetite grains from Mariela (Fig. 10A), and probably from El Laco (Fig. SM6F), to have formed by oxy-exsolution processes, whereas it is more likely that

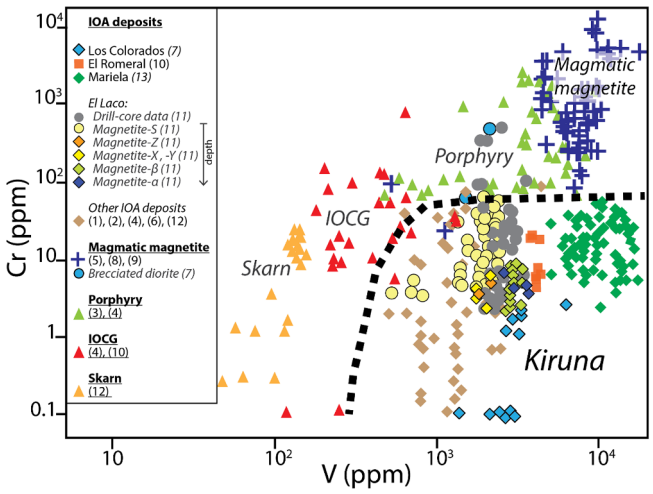

Fig. 15. Concentration of V vs. Cr discrimination diagram modified from Knipping et al. (2015b). Magnetite from IOA deposits can be distinguished from other deposits such as porphyry, IOCG, skarn and magmatic magnetite. Higher V concentrations in magnetite indicate in general a more significant magmatic source. Data source: (1) Loberg and Horndahl (1983); (2) Nyström and Henríquez (1994); (3) Core (2004); (4) Dupuis and Beaudoin (2011); (5) Dare et al. (2014); (6) Dare et al. (2015); (7) Knipping et al. (2015a) and Knipping et al. (2015b); (8) He et al. (2016); (9) Polivchuk (2017); (10) Huang and Beaudoin (2019); (11) La Cruz et al. (2020); (12) Sun et al. (2019); (13) This study.

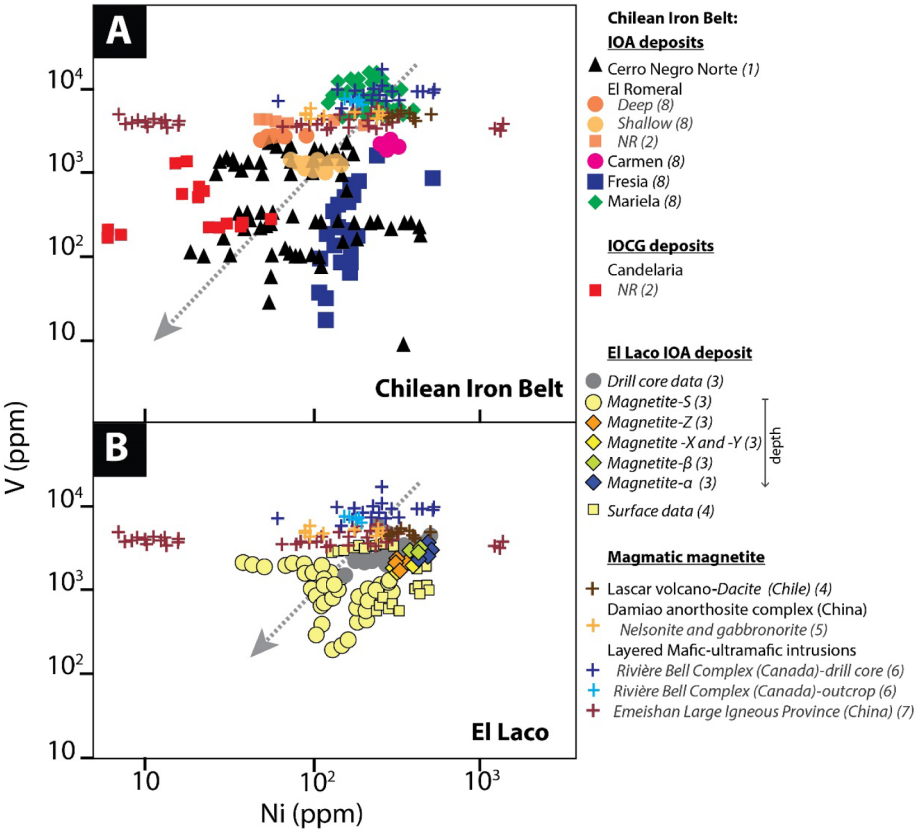

Fig. 16. Concentration of Ni vs. V in magnetite from the Chilean Iron Belt (A) and El Laco (B). Data source: (1) Salazar et al. (2020); (2) Huang and Beaudoin (2019); (3) La Cruz et al. (2020); (4) Broughm et al. (2017); (5) He et al. (2016); (6) Polivchuk (2017); (7) Liu et al. (2014); (8) This study.

the exsolution lamellae observed in magnetite from Fresia (Type-B) formed by re-equilibration processes (Fig. 10G) based on the hydrothermal chemical signature of magnetite (Figs. 11A; 12A,B; 14A,B).

On the other hand, the symplectite texture forms by the breakdown of unstable minerals (2 or more) that are intergrown as straight, curved or vermicular lamellae as a result of changing chemical and/or physical factors (e.g., Mongkoltip and Ashworth, 1983; Claeson, 1998). This texture is well-documented in the literature and various mechanisms of formation including rapid cooling, decompression, oxidation and infiltration of aqueous fluids have been proposed (Moseley, 1984; Claeson, 1998; Hippertt and Valarelli, 1998; Field, 2008; Dégi et al., 2010; Elardo et al., 2012; Tan et al., 2015; Regan et al., 2019). Indeed, symplectite intergrowth of magnetite-rutile ± ilmenite as seen in Mariela (Figs. 4A–C,E, 8, 10E) are reported in certain mafic–ultramafic layered intrusions (e.g., Von Gruenewaldt et al., 1985; Claeson, 1998; Tan et al., 2015). According to Tan et al. (2015), the magnetite-rutile symplectite hosted by ilmenite from the Xinjie Fe-Ti oxide-bearing mafic–ultramafic layered intrusion (SW China) was formed by the subsolidus oxidation of the ilmenite-hematite SS, under relatively oxidizing conditions, controlled by the composition and proportion of interstitial fluids (Buddington and Lindsley, 1964). Although the mineralogical assemblage of both symplectites is similar, in Mariela the host or precursor mineral is a Ti-rich magnetite and it is more likely formed by decompression as evidenced by the breccia-pipe structure observed in Mariela (Fig. 10E).

5.2. Magnetite chemistry and temperature trends: [Ti + V] vs. [Al + Mn] plots

Discrimination diagrams based on minor and trace elements concentrations in magnetite have been proposed by several authors to constrain ore-forming environments (e.g., Dare et al., 2014; Dupuis and Beaudoin, 2011; Knipping et al., 2015b; Nadoll et al., 2012, 2014). Fig. 11 shows the widely used [Ti + V] versus [Al + Mn] discrimination diagram (Dupuis and Beaudoin, 2011; Nadoll et al., 2014) for all magnetite types from the Andean IOA and IOCG deposits discussed here. The plots illustrate the geochemical signature of the different magnetite types recognized in Carmen, Fresia, Mariela, El Romeral, Los Colorados, Cerro Negro Norte from the Chilean Iron Belt (Fig. 11A,B), El Laco (Fig. 11C) and the Candelaria and Mantoverde IOCG deposits (Fig. 11D). The EPMA dataset was used for these plots except for Cerro Negro Norte in which the LA-ICP-MS data were used, because of their very low Ti concentration that could not be measured by EPMA (Table 3).

Overall, the magnetite data for the studied deposits configure consistent cooling trends from high-temperature, magmatic-hydrothermal conditions (> 600 °C) to lower temperature hydrothermal conditions (< 600 °C) (Nadoll et al., 2014). In the next paragraphs, we discuss and compare the chemical composition of major elements in magnetite (Ti, V, Al, Mn) for the studied deposits, in relation with its inferred temperature of formation. It is important to highlight that the temperature trends discussed here, as noted by Nadoll et al. (2014), should be interpreted with care and correspond to broad and qualitative estimations based on magnetite chemistry, coupled to mineralogical observations of the different mineralization styles.

All magnetite types from the Carmen deposit (i.e., Type-I to -IV) show a very similar range of [Ti + V] and [Al + Mn] concentrations (Fig. 11A). Notably, magnetite types I, II, III, IV plot mostly in the *Kiruna field* and in the *Porphyry field*, and to a lesser extent below the *Kiruna field*, distributed as a cluster of points in which no trend is recognized. At Fresia, magnetite types A, B and D display similar [Ti + V] concentrations as Carmen (Fig. 11A). Type-A magnetite has a higher [Al + Mn] concentration plotting mostly in the upper part of the *Porphyry field* and in the *IOCG field*. On the other hand, Type-C magnetite

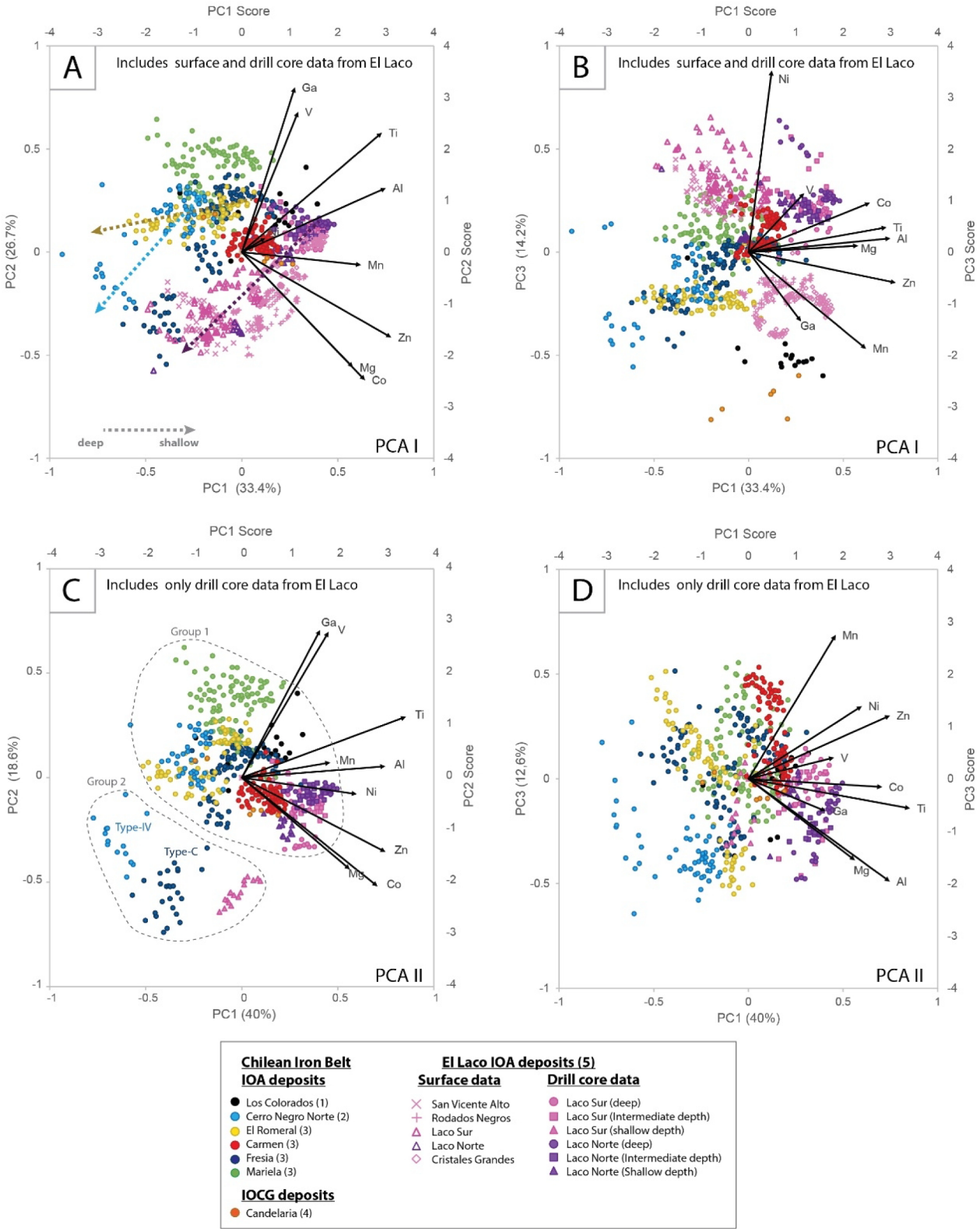

Fig. 17. Biplots for Principal Component Analysis (PCA) of logarithm-transformed magnetite concentrations from Andean IOA-IOCG deposits. Magnetite LA-ICP-MS data on Mg, Al, Ti, V, Mn, Co, Ni, Zn and Ga were used. Bottom and left axes in each plot display the loadings of the Principal Components (PC). The percentage shown on the axes represents the total variance explained by that component. Top and right axes show the scores of the PCs, which are associated with the points (individual analyses). (A) and (B) show a PCA where surface and drill core data from El Laco were included, and (C) and (D) show a PCA where El Laco surface data were discarded. In both PCA, > 70% of the total variance can be represented with the extraction of three PCs (A and C) PC1 vs. PC2; (B and D) PC1 vs. PC3. In biplot A, trends (from shallow levels to depth) that resemble the direction of Ti, Al, Ga and V arrows were recognized in IOA deposits with available drill core data (El Laco, Cerro Negro Norte and El Romeral). In biplot C, two groups (Groups 1 and 2) are observed after PCA analysis. See text for discussion.

plots mostly within the *IOCG field*. The distribution of these magnetite types from *Porphyry field* (Type-A and -B) to *Kiruna field* (Type-D) to *IOCG field* (Type-C) display a cooling trend from magmatic-hydrothermal conditions (~300–500 °C) to low temperature hydrothermal conditions (~200–300 °C). However, the occurrence of re-equilibration textures in these magnetites from Carmen and Fresia (Figs. 2D,F, 3A,F; 10G) indicate that the original trace element geochemistry of primary magnetite was significantly modified. Therefore, we conclude that these magnetite ores were formed by re-equilibration of previously formed magnetite via dissolution-reprecipitation processes. These processes could have been triggered by the infiltration of externally derived hydrothermal fluids of moderate (300–500 °C) to low (200–300 °C) temperatures, similar to those related to magnetite formation in porphyries and IOCG deposits, respectively.

Most magnetite data points from Mariela plot in the magmatic *Fe-Ti, V field* or at the boundary between the *Fe-Ti, V* and *Porphyry fields* (Fig. 11A). The igneous affinity of magnetite from Mariela (*Fe-Ti,V field*) is confirmed by both the formation of symplectite and the well-developed ilmenite ± ulvöspinel exsolution lamellae (see Section 5.1; Fig. 4D, 10A,E) consistent with temperatures above 500° C. We highlight that the Ti concentrations measured in the magnetite Type-α and Type-β are lower than in primary magmatic magnetite due to the formation of exsolution lamellae and symplectite, respectively, which resulted in the loss of Ti from magnetite into exsolved ilmenite, ulvöspinel and rutile. It should be noted that magnetite Type-δ and Type-γ plot more to the left in the *Fe-Ti, V field*, which might reflect a slight decrease in magmatic temperatures. In addition, the lower Mn content in magnetite Type- γ is consistent with formation at lower temperatures (~500 °C) and possibly related to dissolution-reprecipitation processes (Fig. 4A,E).

At Los Colorados, and as described by Knipping et al. (2015a) and Knipping et al. (2015b), most of the data from the magnetite (western) dike from Los Colorados plot in the *Porphyry field* with a few data points in the *Fe-Ti, V field* and *Kiruna field* (Fig. 11B). Type-1, -2 and -3 (Table 3) are also shown in Fig. 11B. The cores of magnetite grains (Type-1) have the highest trace element concentration and overlap with magnetite formed in magmatic Fe-Ti,V deposits, followed by Type-2 magnetite (rim) that plot mostly in the *Porphyry field*. Type-3 magnetite (outer rim), which correspond to the rims of magnetite grains, plot in the *Kiruna* and *IOCG fields*. Based on Nadoll et al. (2014), Knipping et al. (2015a) and Knipping et al. (2015b) interpreted the above described trend as a result of cooling from dominantly high-temperature, magmatic-hydrothermal conditions (> 600 °C) to lower temperature hydrothermal conditions (< 500 °C). A similar trend is observed for magnetite compositions in samples from Cerro Negro Norte and El Romeral (Fig. 11B). At Cerro Negro Norte, both Type-I (magnetite cores) and Type-II (magnetite rims) have similar [Ti + V] concentrations, but Type-I has slightly higher [Al + Mn] concentrations than Type-II (Salazar et al., 2020). Both magnetite types plot mostly within (and below) the *Kiruna field*. Type-III magnetite plots in the *IOCG* and *Kiruna fields*, whereas Type-IV magnetite (late magnetite vein event) plots within (and below) the *BIF field* (Fig. 11B). Even though no magmatic magnetite was identified in Cerro Negro Norte (e.g., plotting in the *Fe-Ti,V field*), a cooling trend similar to the one described for Los Colorados was recognized (Fig. 11B). Similarly, both Type-I and -II from El Romeral plot mostly within and below the *Kiruna field* (Fig. 11B). Only a few points plot in the low part of the *Porphyry field* and near the boundary between the *IOCG* and *Kiruna fields*. It should be noted that the data corresponding to the deepest drill core sample at El Romeral (Type-I and -II; ~347 m) present slightly higher [Ti + V] and [Al + Mn] concentrations than magnetite from shallow levels (Type-I and -II; ~10 m), reflecting a higher formation temperature of magnetite at depth (Fig. 11B). At the deepest section of the deposit, Type-I magnetite shows a more dispersed distribution of data points and slightly higher [Ti + V] and [Al + Mn] concentrations than Type-II magnetite, whereas at shallow depths Type-I and -II data are equally dispersed (Fig. 11B). Therefore, based on the chemistry of magnetite types, we infer that the Cerro Negro Norte and El Romeral deposits were formed under relatively lower temperature conditions than Los Colorados (~300–500 °C; within and below the *Kiruna field*), with slightly lower temperatures recognized in Cerro Negro Norte when compared to El Romeral. At Cerro Negro Norte, a late low-temperature magnetite formation event (< 300 °C; *BIF field*) was also recognized.

Fig. 11C, modified from Ovalle et al. (2018), depicts the chemical variation of drill core and surface outcrop data in magnetite from the El Laco Norte deposit. In general, a distinctive trend is recognized from magmatic (*Fe-Ti,V field*) at depth to moderate-, low-temperature hydrothermal conditions (200–300 °C) towards the surface (Magnetite-Z to Magnetite-α; Fig. 11C). It should be pointed out that Magnetite-α, which plots mostly in the *Fe-Ti,V field*, displays well-developed ilmenite exsolution lamellae further confirming its magmatic origin (Fig. SM6F). Furthermore, surface samples display lower [Ti + V] concentrations than drill core samples, plotting in all fields, even below the *IOCG field* and *BIF field*, but not in the *Fe-Ti,V field*. This points to magnetite growing from moderate- to low-temperature hydrothermal fluids or that magnetite was chemically re-equilibrated by lower temperature fluids after mineralization as evidenced by dissolution-reprecipitation textures observed in Magnetite-X (Fig. SM6C).

Finally, the data from the Candelaria and Mantoverde IOCG deposits display a wide range of [Ti + V] and [Al + Mn] values that plot in all fields, but only a few scattered analyses plot in the Fe-Ti,V field (Fig. 11D). The average value of the Candelaria and Mantoverde data plots in the *IOCG field*. The large amount of data that plot in the *BIF field* and below the *Kiruna field* reflect the comparatively low trace element concentration in hydrothermal magnetite from IOCG deposits. This can be interpreted as magnetite in IOCG systems being formed from cooling hydrothermal fluids of lower temperature than those involved in IOA formation.

5.3. Igneous and hydrothermal magnetite: V-Ti and V/Ti -Fe plots

Experimental studies have demonstrated that the incorporation of trace elements in igneous magnetite depends mostly on temperature, host rock/melt composition, elemental availability, and oxygen (fO_2) and sulfur (fS_2) fugacity (Toplis and Corgne, 2002; Sievwright et al., 2017; Sossi et al., 2018). Magnetite/melt partition coefficients for trace elements vary by several orders of magnitude for igneous magnetite (Dare et al., 2012; Nadoll et al., 2014), whereas there are no available experimental data that constrain the partitioning of trace elements between magnetite and hydrothermal fluid. Acknowledging the lack of partitioning data for hydrothermal magnetite, Nadoll et al. (2014) pointed out that the chemical composition of hydrothermal magnetite would be controlled by the composition of the aqueous fluids, temperature, fO_2, fS_2 and host rock buffering.

Discrimination diagrams based on trace elements have been proposed to distinguish between igneous and hydrothermal magnetite, e.g., Sn versus Ga (Nadoll et al., 2014), Ti versus Ni/Cr (Dare et al., 2014), Ti versus V (Nadoll et al., 2015), and V/Ti versus Fe (wt%) (Wen et al., 2017).

Tin is below or close to the detection limit of the LA-ICP-MS technique in the studied IOA deposits (Tables SM5, SM6), therefore, the Sn versus Ga plot was not used here.

The Ti versus V and V/Ti versus Fe (wt%) diagrams in Figs. 12 and 13, respectively, present new and previously published magnetite analyses from Andean IOAs. In addition, geochemical analyses of magnetite from layered mafic–ultramafic, anorthosite and granitic complexes (Liu et al., 2014; He et al., 2016; Polivchuk, 2017; Wen et al., 2017), and magnetite data from the Candelaria IOCG deposit (Huang and Beaudoin, 2019), are presented as a reference. Fig. 12A and C show the Ti and V concentrations in magnetite for each deposit from the Chilean Iron Belt (CIB) and El Laco, respectively. Titanium vs. V diagrams for each magnetite type are shown in Fig. 12B.

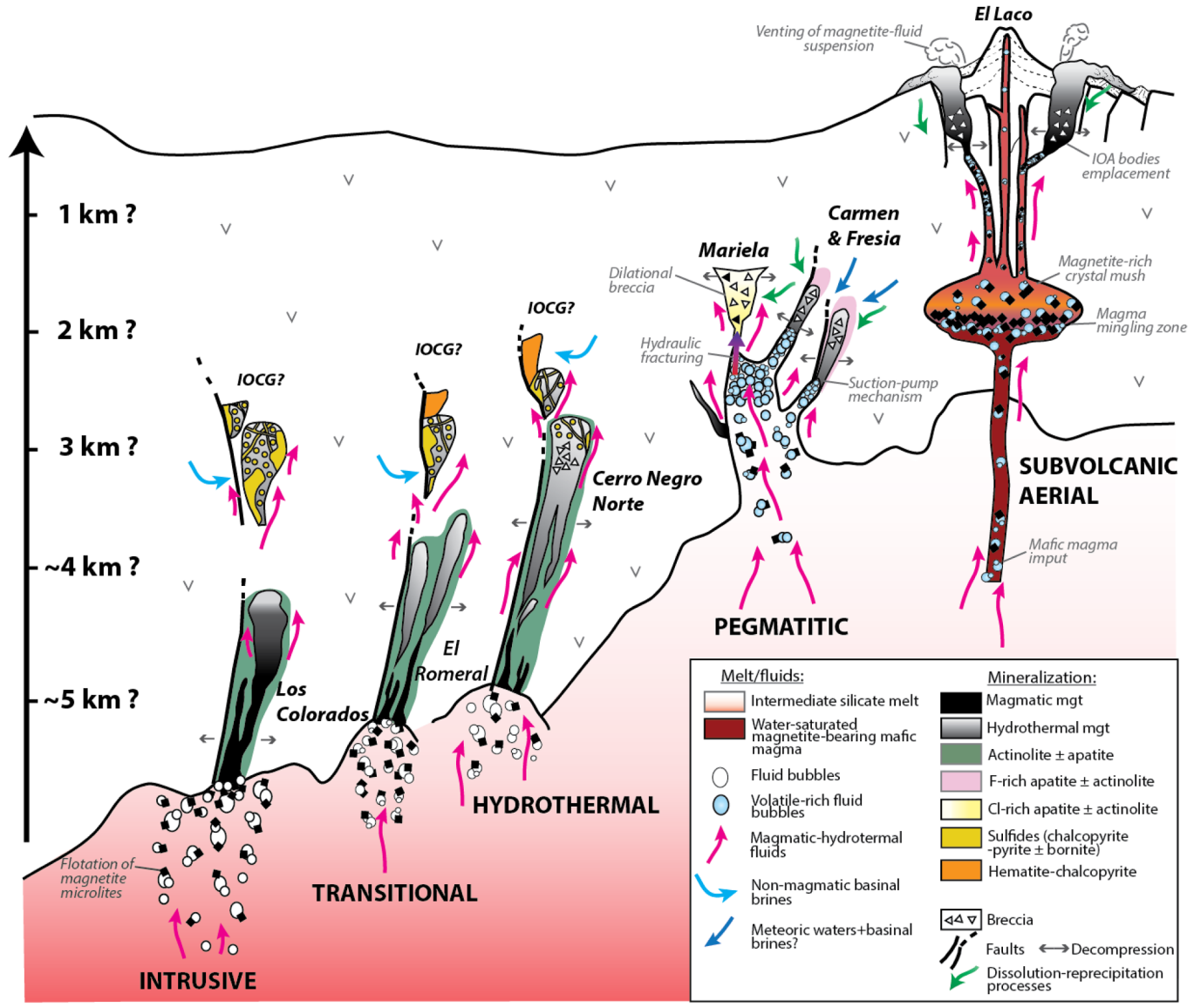

Fig. 18. Schematic genetic model for the formation of Chilean IOA deposits from the Chilean Iron Belt and El Laco. The figure shows different styles or subtypes of IOA mineralization depending on the depth of emplacement: deep, intrusive-like (e.g., Los Colorados); transitional (e.g., El Romeral); intermediate, hydrothermal-like (e.g., Cerro Negro Norte); pegmatitic, apatite-rich (Carmen, Fresia and Mariela); and shallow, subvolcanic/subaerial (e.g., El Laco) deposits. These different IOA subtypes are controlled fundamentally by the depth of formation, the presence of structures/faults that cause decompression, the composition of the host rock, the source and flux rate of hydrothermal fluids, and the infiltration of non-magmatic fluids such as meteoric waters and possible basinal brines. The *flotation model* (Knipping et al., 2015a, 2015b) provides a general framework to explain the origin of Chilean IOA subtypes and the observed genetic link between IOA and IOCG mineralization. See text for discussion.

Data for Carmen and El Romeral plot mostly in the overlapping area between both fields (Fig. 12A). In addition, some data points from Carmen plot in the *igneous field*. Notably, three data clusters are observed for El Romeral. The deep cluster (this study) has higher Ti and V concentrations (average values: 803 and 342 ppm Ti; 2,489 and 2,683 ppm V for Type-I and -II, respectively; Fig. 12B Table 4) than the shallow cluster (this study; average: 571 and 222 ppm Ti; 1,261 and 1,277 ppm V for Type-I and -II, respectively; Fig. 12B). Magnetite Type-I from both clusters have higher Ti and V concentrations than Type- II (Fig. 12B; Table 4). A third cluster comprises data from Huang and Beaudoin (2019) with slightly higher concentrations of Ti and V that plot mostly at the top of the *igneous field* (Fig. 12A).

Data from Fresia are scattered within this plot displaying three groups or clusters. The first cluster consists mostly of magnetite Type-B (Fig. 12B) and plots at the overlapping area between the *igneous* and *hydrothermal field* and in the *igneous field*, similar to the data from Carmen. It follows that magnetite from Carmen (magnetite Type -I, -II and -III) and Type-B from Fresia were formed under similar conditions (Fig. 12B). A second cluster composed of magnetite Type-A plots at the overlapping area between both fields and in the *igneous field* (Fig. 12B). The third cluster (Type-C) shows V concentrations consistent with a hydrothermal composition, but with lower Ti concentrations (Fig. 12B).

Magnetite from Mariela plot above the *igneous field* and have similar V concentrations but lower concentrations of Ti compared to magmatic magnetite (Fig. 12A,B). The few data points from the Candelaria IOCG deposit plot in the overlapping area and in the *hydrothermal field* (Fig. 12A).

Most of the data from Los Colorados plot in the overlapping area between igneous and hydrothermal magnetite and in the *igneous field*, whereas magnetite from Cerro Negro Norte plot mostly in the overlapping area between igneous and hydrothermal magnetite (Type-I, -II and –III; Fig. 12B). However, Type-IV magnetite plots mostly outside of

the hydrothermal field, similarly to Fresia's Type-C (Fig. 12B).

The chemistry of El Laco magnetites reveal a trend from magmatic (high Ti and V concentrations; drill core data) to hydrothermal signatures (low Ti and V concentrations; surface data) (Fig. 12C). Most of the drill core data plot in the igneous field with only a few data points in the overlapping area. Moreover, Magnetite-β and -α plot above the *igneous field* showing high Ti and V concentrations. On the other hand, most of the data from surface (outcrop) samples (Magnetite-S) plot in the overlapping area with some points plotting outside of this area with lower Ti concentrations (Fig. 12C).

Fig. 13 shows the Fe concentration (wt%) versus the V/Ti ratio discrimination diagram proposed by Wen et al. (2017). This plot was constructed based on the observation that igneous and hydrothermal magnetites have different V/Ti ratios, and variable Fe concentrations (Wen et al., 2017). Fig. 13A and B show the data from IOA deposits from the CIB and El Laco, respectively. All data from the Andean IOA deposits (CIB and El Laco) plot in the *hydrothermal field* (Fig. 13A,B), and a re-equilibration trend is only observed for magnetite from Los Colorados (Deditius et al., 2018). Based on our analysis, we conclude that the V/Ti ratio should be used with caution because of re-equilibration or post-crystallization processes that can modify the original Ti concentration in magnetite. On the other hand, V appears to be a better discriminant element in magnetite because it is less susceptible to chemical re-equilibration or remobilization and it is more homogeneously distributed in magnetite grains (Rojas et al., 2018b; this study).

Mariela and Los Colorados data show slightly lower Fe concentrations than other IOA deposits from the CIB, pointing to a more magmatic character (Fig. 13A). Most of the magnetite drill core data from El Laco present lower V/Ti ratio (V/Ti $<$ 1 on average) than the surface data (V/Ti $>$ 1 on average), however, there is some overlap between drill core and surface data (Fig. 13B).

5.4. Temperature and fO_2 trends: Ga vs. V plots

Recently, the Ga versus V plot was used to trace the chemical evolution of magnetite from the Cerro Negro Norte deposit (Salazar et al., 2020). This diagram was proposed after observations that Ga concentrations, as well as V, are consistently higher in magmatic magnetite than in hydrothermal occurrences (Nadoll et al., 2014). Vanadium is preferentially incorporated into magnetite at high temperature and more reducing (low fO_2) conditions (Toplis and Corgne, 2002; Nadoll et al., 2014). The data plotted in Fig. 14 show the Ga and V signature of magnetite from the studied deposits. Fig. 14A shows that IOA deposits from the Chilean Iron Belt are characterized by variable Ga and V concentrations in magnetite. A more detailed plot for all magnetite types for each deposit from the Chilean Iron Belt is shown in Fig. 14B. Data for Mariela, for instance, show a distinctive high-temperature magmatic character and highly reduced formation conditions, with relatively high Ga (21.7–68.3 ppm) and very high V (4,760–16,800 ppm) concentrations in magnetite (Table 4 and Table SM5).

Magnetite from Carmen (Type-I, -II, -III) and Fresia (Type-B) reflect similar conditions of magnetite formation, but at Fresia temperatures would reach lower values (Type-B and Type-C; Fig. 14A,B) probably related to the infiltration of late oxidized fluids. The three clusters observed for Fresia are consistent with the observed clusters in Fig. 12A and 12B, in which Type-B has the highest V concentrations (average 1,756 ppm; Table 4) respect Type-A (average 595 ppm V) and Type-C (average 146 ppm V), whereas Ga concentrations are similar between Type-A and Type-B (average: 35 and 31.9 ppm, respectively) and lower in Type-C (average 14.9 ppm Ga).

Magnetite chemistry from Los Colorados indicate a relatively high-temperature magmatic character and highly reduced formation conditions, but with higher Ga (50–73 ppm) and lower V (1,368–6,435 ppm) concentrations than data from Mariela. Data from El Romeral obtained in this study indicate a decreasing temperature trend from high-temperature magmatic-hydrothermal conditions (intermediate area between high-temperature magmatic and high-temperature hydrothermal; Fig. 14A,B) to relative low-temperature hydrothermal conditions from bottom to top of the deposit (Rojas et al., 2018b; this study; Fig. 14A,B).

Cerro Negro Norte magnetites reflect a continuous decreasing temperature trend from high-temperature hydrothermal conditions and relatively low fO_2 (Type-I and -II; Fig. 14A,B), to low-temperature conditions (Fig. 14A,B) probably related to changes in the composition of the fluid as it ascended and cooled (Type-III; Fig. 14B; Salazar et al., 2020). The precipitation of magnetite veinlets (Type-IV, Fig. 14B) at even lower temperatures (~200–300 °C) would be related to a late metasomatic event and more oxidized hydrothermal fluids (Fig. 14A,B; Salazar et al., 2020).

For El Laco, a transition from high-temperature magmatic-hydrothermal and relative low fO_2 conditions observed in drill core magnetites (Magnetite-α and -β), to high-temperature hydrothermal and relative intermediate fO_2 conditions (Magnetite-Z), to low-temperature and relative high fO_2 conditions is observed in surface samples (Magnetite-S) (Fig. 14C).

5.5. Other discrimination diagrams: the Ni-V and Cr-V plots

Figs. 15 and 16 show the V versus Cr (Knipping et al., 2015b) and Ni versus V (Loberg and Horndahl, 1983) plots, respectively, for magnetite from the Chilean Iron Belt and El Laco. The V versus Cr plot is used to discriminate Kiruna-type IOA deposits from other high-temperature deposits including porphyry, IOCG and Fe-Ti,V deposits (Nyström and Henríquez, 1994). Chromium (Cr^{3+}) is highly compatible in magmatic magnetite; however, it may be depleted in magnetite from IOA deposits either due to the preferred incorporation of Cr into augite or more probably to the high mobility of Cr^{6+} in fluids (James, 2003). Chromium is below detection limits in Cerro Negro Norte, Carmen and Fresia (Table 4). Data from Mariela, El Romeral, Los Colorados and El Laco plot in the *Kiruna field* ($<$ 100 ppm Cr and $>$ 500 ppm V; Knipping et al., 2015b). It should be noted that the V concentration in magnetite from Mariela (average 9,547 ppm) is similar to values reported for magmatic magnetite (Fig. 15); however, they show a lower Cr concentration (~15 ppm). Kiruna-type deposits present higher V concentrations than IOCG and iron skarn deposits, but lower Cr concentrations than porphyry deposits (Fig. 15).

Previous studies have shown that the transition metals including Co and Ni are strongly compatible (Ni $>$ Co) in igneous magnetite (D_{Co} = 7.5 and D_{Ni} = 30; Dare et al., 2012), but are incompatible relative to co-precipitating hydrothermal sulfides such as pyrite and chalcopyrite. Hence, hydrothermal magnetite in porphyry systems, IOCG and IOA deposits is commonly depleted in Co and Ni. Fig. 16 shows a trend from high to low Ni and V concentrations. For the CIB, the high V (average ~9,547 ppm) and Ni (average ~250 ppm) concentrations in magnetite from Mariela are similar to those reported for igneous magnetite (Fig. 16A). Relatively similar Ni concentrations in magnetite from Carmen and Fresia (Carmen: 299 ppm; Fresia: 189 ppm on average) are consistent with the presence of scarce sulfides. In addition, the low Ni concentration in hydrothermal magnetite from Cerro Negro Norte (average 83 ppm; Type-III and -IV) and Candelaria are consistent with the abundant presence of sulfides in these deposits.

In the El Laco deposit, the highest Ni concentrations are found at depth (Magnetite-α and -β; average: 440 and 392 ppm, respectively), whereas superficial magnetite (Magnetite-S) has a lower Ni ($<$ 300 ppm) concentration, probably related to pyrite mineralization found in the Pasos Blancos area, near the Pico Laco (Naranjo et al., 2010).

5.6. Principal Component analysis (PCA): A statistical overview of magnetite trace element geochemistry

The magnetite trace element dataset was further evaluated by performing a Principal Component Analysis (PCA), which provides a general multivariable overview of the compositional variability of magnetite. This statistical approach has been used to better understand trace element concentrations in magnetite from volcanogenic massive sulfide, porphyry Cu-Mo-Au and skarn deposits (Makvandi et al., 2016; Canil et al., 2016; Huang et al., 2016) and also in other "fingerprint" minerals such as pyrite (e.g., Gregory et al., 2015, Román et al., 2019). In this analysis, we considered LA-ICP-MS magnetite trace element data (Fig. 9), including: Mg, Al, Ti, V, Mn, Co, Ni, Zn and Ga. Chromium, Cu and Sn were discarded due to the large number of analyses below detection limit (Cr ~20%, Cu ~42% and Sn ~76%). A brief description of the PCA methodology and biplots are presented in the Supplementary Material file.

Two PCA procedures were carried out (Fig. 17). The first PCA (PCA I) includes surface and drill core data from Laco Norte and Laco Sur, in addition to surface data from San Vicente Alto, Rodados Negros and Cristales Grandes (Fig. 17A,B); whereas the second PCA (PCA II) considers only drill core data (shallow, intermediate and deep) from Laco Norte and Laco Sur (Fig. 17C,D). Data from the Cretaceous IOA deposits are considered in both PCA procedures. PCA I and PCA II were performed to evaluate the effects of the large amount of surface data from El Laco. In both cases, around a 75% of the variance can be explained by the extraction of three Principal Components (PC).

Principal Component 1 (PC1) and PC2 explain ~60% of the total variance of the dataset in PCA I and PCA II. Both PCAs yielded similar results, where biplots show an evident clustering of data by deposit and along the Co, Mg, Zn arrows (Fig. 17A,C). In general, magnetite from El Laco is more enriched in Co, Mg and Zn, while magnetite from Mariela is depleted in these elements (Fig. 17A,C). In addition, the data for each deposit closely follows the direction of the Ti, Al, Ga and V arrows (Fig. 17A) and the Ga and V arrows (Fig. 17C). A similar behavior was determined in drill core samples from Cerro Negro Norte, El Romeral and El Laco (dashed arrows in Fig. 17A). Particularly, deep magnetite from these deposits is relatively enriched in Ti-Al-Ga-V when compared to shallow magnetite from the same deposit. Moreover, Fig. 17C clearly shows two groups (Group 1 and Group 2) after PCA analysis. Group 1 includes most of the dataset and is relatively more enriched in Ga-V compared to Group 2. It follows that the different trends from relatively high Ti, Al, Ga, and V to relatively low concentration of these elements (Fig. 17A) are consistent with the different temperature and/or fO_2 trends observed in the [Ti + V] versus [Al + Mn] (Fig. 11) and Ga versus V (Fig. 14) plots. Similarly, Group 2 data is consistent with low-temperature hydrothermal magnetite from Cerro Negro Norte (Type-IV), Fresia (Type-C) and El Laco (shallow depth) (Figs. 11, 14, 17).

Principal Component 3 (PC3), which represents ~14% (PCA1) of total variance is closely related to Ni in PCA 1 (Fig. 17B). However, this element is not correlated to any other studied element. Furthermore, Fig. 17B shows that Candelaria, Los Colorados, El Romeral, much of the surface data from Cristales Grandes and Rodados Negros (El Laco) and low-temperature hydrothermal magnetite from Cerro Negro Norte (Type-IV) and Fresia (Type-C), plot in the opposite direction of the Ni trend and reflect a Ni-depleted magnetite geochemistry. These observations are consistent with our interpretations suggesting that Ni could be used as a tracer for the presence of sulfides micro to nano-inclusions in magnetite.

5.7. A genetic model for Andean IOA deposits

The data presented here provide new insights on the evolution of Cretaceous IOA deposits from the Chilean Iron Belt and the Pliocene El Laco deposit in Chilean Altiplano of northern Chile. These deposits were formed and later modified by different processes under varied conditions, which are recorded in microtextures and the geochemistry of magnetite.

Based on our observations and data from the CIB and El Laco, different styles or subtypes of IOA mineralization were identified (Fig. 18). These IOA subtypes reflect formation at different crustal depths, e.g., deep, intrusive-like (e.g., Los Colorados); transitional (e.g., El Romeral); intermediate, hydrothermal (e.g., Cerro Negro Norte); pegmatitic, apatite-rich (Carmen, Fresia and Mariela); and shallow, subvolcanic/aerial (e.g., El Laco) deposits. In addition to the depth of formation, Andean IOA deposits are fundamentally controlled by: (i) cooling, reflected in magnetite trace element geochemistry and microtextures, which also depend of the source and flux rate of hydrothermal fluids and even the infiltration of meteoric waters or basinal brines; and (ii) decompression, related to the presence of structures and faults, which entails classifying IOA deposits based on subtypes.

Knipping et al. (2015a) and Knipping et al. (2015b) explained the presence of a distinct textural and chemical variation between cores (Type-1) and rims (Type-2 and -3) in the intrusive-like Los Colorados by a transition from igneous to magmatic-hydrothermal conditions. In this novel genetic model, i.e., the *flotation model*, microlites of magmatic magnetite (Type-1) crystallize from an intermediate to mafic silicate melt and later ascend by coupling with bubbles of fluids exsolved from the magma. As the magmatic magnetite suspensions ascend, they coalesce and the modal abundance of magnetite increases by further precipitation of hydrothermal magnetite as overgrowths (Type-2 and -3) on primary magnetite filling interstitial spaces at the level of neutral buoyancy. The rapid ascent of the bubble-magnetite suspensions through structures or faults resulted in the formation of these magnetite-rich ore bodies (Fig. 18). The transtensional, strike-slip, crustal scale Atacama Fault System (AFS) provides and optimum, structurally-controlled, permeable conduit that allowed the magnetite-rich suspensions to ascend from the source magma (Knipping et al., 2015a, 2015b; Simon et al., 2018).

Considering that most IOA deposit in the Chilean Iron Belt are genetically related to major transtensional fault systems, the effect of pressure on magnetite solubility is likely a crucial control on magnetite mineralization (Simon et al., 2004; Rojas et al., 2018b). Iron solubility modeling, as a function of pressure and temperature, was performed by Rojas et al. (2018b) considering for $FeCl_2$ solubility and magnetite precipitation a fluid salinity of 35 wt% NaCleq and a temperature and pressure range of 380–620 °C and 60–200 MPa, respectively. The model supports that structures favor the emplacement of ore bodies and that the consequent pressure drop decreases the solubility of $FeCl_2$ in aqueous fluids and triggers magnetite precipitation. Moreover, the rate of decompression affects the efficiency of magnetite precipitation such that rapid decompression favors formation of large magnetite ore bodies. Thus, a $FeCl_2$ bearing hydrothermal fluid at 600 °C will precipitate 50% more magnetite at 100 MPa compare with the mass of magnetite at 120 MPa (Rojas et al., 2018b).

The mineralogical, microtextural and geochemical data from Los Colorados (Knipping et al., 2015a, 2015b; Bilenker et al., 2016; Deditius et al., 2018), El Romeral (Rojas et al., 2018b; this study) and Cerro Negro Norte (Salazar et al., 2020) deposits are consistent with a combined igneous/magmatic-hydrothermal model, in agreement with deposits from the Kiruna district in Sweden (Jonsson et al., 2013; Weis et al., 2013; Westhues et al., 2016, 2017b; Westhues et al, 2017a). However, in both the transitional El Romeral and the hydrothermal-like Cerro Negro Norte (Fig. 18), high-temperature, magmatic magnetite (> 600 °C) was not identified (Figs. 11, 12, 14). This suggests that the magnetite ore bodies in both deposits could extend to deeper levels.

The Carmen, Fresia and Mariela pegmatitic IOA deposits are genetically and spatially related to extensional strike-slip duplexes in which IOA mineralization is located at or close to intersecting faults (Treloar and Colley, 1993, 1996; Bonson et al., 1997; Río Tinto internal report, 2001; Table 1). These fault configurations coupled with transtensional displacement created localized dilational zones that act as

tectonic traps for the formation of IOA with abundant F-rich apatite in comb textures (Carmen and Fresia) or Cl-rich apatite in dilational breccias (Mariela) (Palma et al., 2019). In here, the crystallization of apatite was controlled by the fracture opening velocity, crystal growth rate and fluid saturation (Chauvet, 2019). These vein systems characterized by comb textures and relatively large crystals reported at the Caleta Coloso strike-slip duplex (~24°S) developed along the Atacama Fault System (AFS) during the Early Cretaceous (Herrera et al., 2005; Olivares et al., 2010). These fluid-filled open fractures formed under sub-hydrostatic pressures suggesting that mineral precipitation was triggered by a pressure drop at shallow crustal levels (< 4 km) through suction-pump mechanism (Olivares et al., 2010). In this fluid-fracture relationship, the migration of fluids would be triggered by fracturing of the rock associated with the activity of the fault and not by fluid overpressure (Herrera et al., 2005). The abrupt pressure drop within the fracture triggers fluid injection into dilatation zones (Sibson et al., 1975; Sibson, 2001; Cox et al., 2001) causing the immediate filling of the fracture by fluids coming from areas of higher pressure (pressure gradient), and the consequent precipitation of ore minerals (Olivares et al., 2010). The suction-pump mechanism could explain the formation of pegmatite-like IOA deposits such as Carmen and Fresia, and of comb textures where the rate of crystallization is lower than the fracture opening rate (Chauvet, 2019). Thus, crystallization only covers the fracture/vein wall and crystals grow larger during multiple stages of growth, sometimes associated with a change in the fluid composition (Dowling and Morrison 1990). The fracture is sealed by mineral precipitation until a new seismic rupture can cause brecciation, as observed in Carmen and Fresia. On the other side, the Cl-rich apatite dilational breccias from Mariela formed by cracking due to fluid overpressure or hydraulic fracturing (Chauvet, 2019). The space created by fragmentation of the intrusive host rock affected by the strike-slip duplex formation, and the dilational breccias texture could have formed at the initiation of the process when rates of aperture are weak (Chauvet, 2019). Therefore, fragments derived from a much greater depth, evidenced by the purely magmatic magnetite signature from Mariela, were emplaced at shallow levels. This could suggest the occurrence of a much larger massive magnetite body at depth and is consistent with the high and restricted εNd values (+5.5 to +6.0) and low $^{87}Sr/^{86}Sr$ initial ratios of Cl-rich apatite from Mariela (0.70390–0.70407) that support crystallization from a high-temperature, saline magmatic-hydrothermal fluid exsolved from a primitive magmatic source (Palma et al., 2019).

On the other hand, magnetite from the different ore bodies from El Laco recorded both purely igneous and magmatic-hydrothermal signatures (Ovalle et al., 2018). Ovalle et al. (2018) proposed that El Laco formed as a result of an optimal convergence of common subaerial volcanic processes in arc volcanoes (Fig. 18). In the early stages, Ti-rich igneous magnetite (Magnetite-α and -β) crystallized at near liquidus conditions within the andesitic magma chamber beneath the volcanic complex (Fig. 18). The periodic injections of crystal-bearing, vapor-saturated mafic magma into the base of the magma chamber could lead to rapid decompression and volatile exsolution (i.e., bubbles of supercritical fluid), which increases the magnetite budget. The consequent ascent, growth, coalescence and accumulation of the magnetite-fluid-bubble pairs form a magnetite-rich, hypersaline suspension that continues ascending and becomes Fe-rich by scavenging Fe (Cl and other metals) from the magma. During the collapse of the El Laco volcanic edifice, the hydraulic injection of the magnetite-fluid suspension via collapse-related fissures, ring structures and secondary craters on the flanks of the El Laco volcano form the hydrothermal breccia bodies at depth observed in the drill core samples from deeper levels in the deposit. The Fe-rich magmatic-hydrothermal fluid continues ascending to shallow levels and crystallizes hydrothermal magnetite (Magnetite-X, -Y and -Z) during progressive cooling until it reached the surface where magnetite-S is subject to weathering. The surface venting of the hydrothermal magnetite suspension may formed the Fe-rich lava-like flows and dike-like bodies that outcrop around the Pico Laco resurgent dome (Fig. 18).

Overall, the IOA deposits from the Chilean Iron Belt and El Laco deposit are consistent with a model wherein a magnetite-apatite fluid suspension evolves from an intermediate to mafic silicate magma and ascend towards the surface along preexisting crustal faults (Chilean Iron Belt), and alternative, fissures formed during the collapse of a volcanic structure (El Laco). However, where in the CIB volatile-rich fluids are exsolved directly from intermediate to mafic magmas in El Laco volatile-rich fluids are exsolved from a mafic magma underplating the andesitic magma body and then transferred to the overlaying magma chamber (Fig. 18). It should be noted that there is abundant evidence that magnetite segregation is a common process in arc magmas (Edmonds et al., 2014). The *flotation model* allows a variation and the definition of different styles or subtypes of IOA mineralization and provides a new general framework to understand the formation of Andean IOA deposit. It is clear though, that as new data become available from other IOA deposits around the world, the model could be modified to accommodate these new observations and further variations of the general model are likely to be presented.

5.8. The IOA and IOCG connection

The oscillatory zoning, crustiform-colloform banding and re-equilibration textures observed in several magnetite types, as well as a low concentration of compatible (e.g., Ti, V, Ga, Cr) and a high concentration of incompatible and fluid mobile elements (e.g., Si, Ca, Pb, Cu), support formation at moderate to low-temperatures (< 600 °C). On the other hand, the magnetite chemistry of the Candelaria and Mantoverde IOCGs reflects a continuum from high-temperature magmatic, to magmatic-hydrothermal magnetite, to shallow IOCG magnetite mineralization formed from cooling hydrothermal fluids (Fig. 11D). The genetic model described above (Fig. 18), allows for a vertical continuum or transition from a deep-seated IOA (e.g., Los Colorados, El Romeral and Cerro Negro Norte) to shallow IOCG mineralization.

Geochemical data and field observations in IOA deposits from the CIB are consistent with a continuum from deep IOA to shallow IOCG hydrothermal mineralization. This is evidenced by the change in magnetite chemistry and the ubiquitous presence of sulfides in IOA deposits (e.g., Cerro Negro Norte; Fig. 18), some of which could be related to late superimposed hydrothermal events (Knipping et al., 2015a, 2015b; Barra et al., 2017; Rojas et al., 2018b). According to Raab (2001) the minor Cu-Au mineralization at Cerro Negro Norte is predominantly associated with pyrite ± chalcopyrite veinlets and to the tourmaline–quartz alteration. Previously, Vivallo et al. (1995) documented Au grades up to 1 ppm in pyrite and < 100 ppb in magnetite. Those authors concluded that a late hydrothermal event characterized by a high fS_2 remobilized Au from the Fe ore (Vivallo et al., 1995; Raab, 2001). Evidence of pyrite and Cu oxide mineralization and significant concentrations of Cu in both apatite (Palma et al., 2019) and magnetite (Table 5; Fig. 9) further support this transition of mineralization styles. In addition, the Mariela and Carmen deposits are spatially related to IOCG mineralization zones. Specifically, the Barreal Seco (Teresa de Colmo) IOCG hematite breccias (Correa and Hopper, 2000) are located ~3 km south of the Mariela. This spatial relation supports a possible genetic connection between IOA and IOCG mineralization.

According to Knipping et al. (2015a) and Knipping et al. (2015b), during the formation of the IOA mineralization, the exsolved bubbles, i.e., the high-Cl magmatic-hydrothermal fluid, would efficiently scavenge metals (Fe, Cu, Au, S and others) from the silicate melt due to the high fluid/melt partition coefficients for these element (Chou and Eugster, 1977; Boctor et al., 1980; Simon et al., 2004; Williams-Jones and Heinrich, 2005; Simon and Ripley, 2011; Zajacz et al., 2012a, 2012b). Thus, the hydrothermal fluids have the ability to transport these elements into more distal or shallow levels in the crust where they

precipitate their chemical load as oxides ± sulfides ± phosphates, either through cooling (T < 400 °C; Hezarkhani et al., 1999; Ulrich et al., 2001; Hurtig and Williams-Jones, 2014; Williams-Jones and Migdisov, 2014) or possibly by mixing with meteoric fluids (Barton, 2014; Monteiro et al., 2008a, 2008b) forming IOCG mineralization. Experimental data reveal that the maximum solubility for Cu is reached at ~600 °C and drops abruptly as the fluid cools (Migdisov et al., 2014; Williams-Jones and Migdisov, 2014). The solubility of Cu in the cooling-magmatic hydrothermal fluid also increases with increasing fO_2 (Williams-Jones and Migdisov, 2014). On the other hand, the maximum solubility of Au in a cooling magmatic-hydrothermal fluid shifts to lower temperatures with decreasing density of the fluid (Hurtig and Williams-Jones, 2014). Those authors determined experimentally that the Au solubility reaches a maximum at ~500 °C in an intermediate density fluid and at ~400 °C for a low density fluid. The fact that some Au-rich deposits are magnetite-rich suggests that high fO_2/fS_2 ratios favor the deposition of large amount of magnetite under feldspar-stable conditions and important amounts of gold (Sillitoe, 1979; Simon et al., 2004). Thus, as the fluid ascends and migrates from the deep, IOA environment its chemical composition will change increasing its metal (e.g., Fe, Cu, Au) and salinity content. Late sulfide (chalcopyrite, pyrite and bornite) precipitation occurs at lateral or upper crustal levels upon cooling under ~400 °C (Simon et al., 2018).

5.9. Implications for exploration of Andean IOA-IOCG deposits

The refinement of ore deposit models is critical for the development of exploration strategies. During the last few years, our knowledge of IOA deposits has increased significantly. Multiple studies carried out on several Cretaceous IOA deposits from the Coastal Cordillera of northern Chile have resulted in a new genetic model, i.e., the *flotation model*, as an alternative to the traditional liquid immiscibility and metasomatic models (Knipping et al., 2015a, 2015b, 2019a; Bilenker et al., 2016; Reich et al., 2016; Barra et al., 2017; Deditius et al., 2018; Rojas et al., 2018a, 2018b; Simon et al., 2018; La Cruz et al., 2019, 2020; Palma et al., 2019; Salazar et al., 2020).

These recent studies have changed our vision of Andean IOA deposits. Iron ore bodies were considered as simple accumulations of massive magnetite ± apatite–actinolite. In addition, magnetite mineralization was thought to be identical in all IOA deposits from the Chilean Iron Belt. The large geochemical database generated during these last few years and summarized in this study, shows that magnetite chemistry is far from simple. In particular, the study of drill core samples from several IOA deposits has allowed the determination and evaluation of the geochemical nature of the iron ore at depth. The wide diversity of microtextures and variable geochemistry of magnetite reflect different and complex formation conditions including depth of emplacement, temperature, redox and fluid/rock ratio. The interplay of these factors produces different styles of IOA mineralization, i.e., the "IOA clan" (Fig. 18), which involved a combination of igneous, magmatic-hydrothermal and reequilibration processes (Fig. 10). The recognition of these IOA sub-types is relevant in exploration strategies and mining planning.

In addition, several authors have proposed an upward zonation from magnetite-actinolite-apatite (IOA) to magnetite-sulfide (IOCG) mineralization (Espinoza et al., 1996; Sillitoe, 2003; Barra et al., 2017). The presence of abundant sulfides (pyrite, chalcopyrite) in IOA deposits, e.g., Cerro Negro Norte (Raab, 2001; Salazar et al., 2020), could represent the transition from IOA to IOCG with two main exploration implications: (i) the probable occurrence of a large, massive iron ore body at a depth with a more magmatic signature (Figs. 10 and 18), and (ii) the possible presence of distal IOCG mineralization spatially related to the IOA mineralization.

On a more regional scale, the tectono-magmatic processes involved in the formation of IOA-IOCG deposits in the Coastal Cordillera of northern Chile have been discussed by Sillitoe (2003) and Richards et al. (2017). Both IOCG and IOA deposits were emplaced during regional extension or transtension in the mid-Cretaceous. Mineralization occurs in close spatial and temporal association with ductile to brittle faults and fractures of varied strike or at strike-slip duplex configurations (Table 1). The genetic relation between iron bodies and structures has been further supported by recent studies that show the effect of pressure on both magnetite and chlorapatite solubility (Rojas et al., 2018b; Palma et al., 2019). On the other hand, the genetic relation of IOA mineralization to dioritic intrusions has been demonstrated for El Romeral (Rojas et al., 2018a) and Carmen (Gelcich et al., 2005; Zhang et al., 2017). Overall, it appears that optimal magnetite accumulation/precipitation conditions were attained in more immature magmatic arcs, characterized by crust thinning and mafic-to-intermediate magmatism, such as in the Chilean Iron Belt of the Coastal Cordillera, northern Chile.

In summary, the recent *flotation model* has provided an elegant explanation not only for the formation of Chilean IOA deposits but also for the possible genetic relation with IOCG mineralization. The model has been supported by recent studies on the large El Romeral, Cerro Negro Norte El Laco, and other smaller deposits such as Carmen, Fresia and Mariela. Furthermore, the present study describes different subtypes of IOA deposits based on mineralogical, textural and geochemical data, which reflect a combination of formation processes. The identification of these different IOA subtypes and their formation processes are critical in successful exploration programs.

6. Concluding remarks

The new data presented here coupled to previous studies on the microtextures and chemistry of magnetite from Andean IOA deposits located in the Cretaceous Iron Belt (CIB), Coastal Cordillera (25-31°S), and the Pliocene El Laco volcanic complex (~23°S), Central Volcanic Zone of the Chilean Altiplano, provide new constraints on the formation of this ore deposit type.

The different magnetite identified in Los Colorados, Cerro Negro Norte, El Romeral, Carmen, Fresia and Mariela types display a broad spectrum of microtextures (e.g., oscillatory zoning, colloform banding, re-equilibration textures, exsolution lamellae and symplectite) and mineral inclusions randomly distributed in magnetite cores, arranged following crystallographic planes or in trace element-rich bands. Each of these textures provide information on the formation processes, i.e., igneous, magmatic-hydrothermal, metasomatic or re-equilibration processes. Overall, these microtextures coupled with the magnetite chemical composition reveal that IOA deposits formed by a combination of magmatic and hydrothermal processes, and that magnetite is susceptible to multiple textural and compositional re-equilibrium events during the formation and evolution of IOA deposits. The chemistry of magnetite reflects variable conditions/events of formation for each of the deposits under study (Fig. 18). These conditions range from purely magmatic, high-temperature (> 600 °C) and reduced (low-fO_2) conditions; to moderate, low-temperature magmatic-hydrothermal and intermediate-fO_2; to low-temperature (200–300 °C) and more oxidized (high-fO_2) hydrothermal conditions. A clear continuous transition from high-temperatures, low fO_2 conditions in the deepest portions of the deposits to low-temperature, high fO_2 conditions towards shallow levels are recognized in El Laco. Trace elements, such as Al, Ti, V, Cr, Mn, Ni, Cu and Ga are incorporated into both magmatic and hydrothermal magnetite. The concentration of these elements in magnetite are a function of element availability (source), oxygen and sulfur fugacity, co-precipitation of competing mineral phases, fluid-rock interaction, the occurrence of nano- to micron-scale inclusions and most importantly, temperature. Moreover, the observation of re-equilibration textures in magnetite suggest that the primary composition of magnetite can be modified complicating the use and interpretation of different discrimination diagrams. In particular, a high Ti concentration in magnetite has been used extensively as an indicator of a magmatic

origin, however, Ti appears to be mobile during hydrothermal alteration and/or re-equilibration processes. In addition, the presence of Fe-Ti oxides exsolution lamellae and symplectite formed by oxy-exsolution processes and decompression, respectively, requires complex re-calculations to determine the original composition of magnetite. Therefore, both V and Ga are better discriminant elements to determine the temperature and fO_2 conditions of magnetite crystallization.

The microtextural and geochemical data in magnetite from IOA deposits from both the Chilean Iron Belt and El Laco, can be explained by the *flotation model*. In this model a magnetite-apatite-fluid suspension evolves from an intermediate/mafic silicate magma and ascends towards the surface along preexisting crustal faults (Chilean Iron Belt) or alternatively, through fissures formed during the collapse of the volcanic structure (El Laco). As exemplified by El Laco (Ovalle et al., 2018) and Cerro Negro Norte (Salazar et al., 2020), the *flotation model* allows a variation within its general framework to accommodate different styles or subtypes of IOA mineralization within upper crustal levels. The variations observed in Andean IOA deposits suggest that these deposits comprise a group or clan of deposits with variable degrees of magmatic and hydrothermal signatures from deep, intrusive-like (e.g., Los Colorados); transitional (e.g., El Romeral); intermediate, hydrothermal-like (e.g., Cerro Negro Norte); pegmatite, apatite-rich (Carmen, Fresia and Mariela); and, shallow, subvolcanic/aerial (e.g., El Laco) deposits. These different IOA subtypes are controlled fundamentally by the depth of formation, the presence of structures/faults for decompression, the composition of the host rock, the source and flux rate of hydrothermal fluids, and even the infiltration of non-magmatic fluids such as meteoric waters and possible basinal brines. The proposed formation model also supports the observed genetic link between IOA and IOCG mineralization in which a continuum from deep, sulfide-free, magnetite-apatite (IOA) mineralization to shallow magnetite + sulfide-rich (IOCG) mineralization is supported by magnetite geochemical data and field observations in the Andean IOA-IOCG province.

In addition, pegmatite-like apatite-rich IOA deposits, characterized by macroscopic comb-like textures and breccias, support the fact that the structural configuration and decompression are first order control factors in the formation of Andean IOA deposits. These deposits would be formed by a drop in pressure caused by fracturing (suction pump mechanism; Carmen and Fresia) or by the hydraulic injection of high-temperature and high-salinity magmatic-hydrothermal fluids, respectively, that lead to the precipitation of pressure-dependent solubility mineral phases such as magnetite and apatite.

Declaration of Competing Interest

The authors declare that they have no known competing financial interests or personal relationships that could have appeared to influence the work reported in this paper.

Acknowledgments

This research was funded by ANID-FONDECYT grants 1190105 and 1140780. The authors acknowledge the support of the Millennium Nucleus for Metal Tracing Along Subduction. The LA-ICP-MS analytical work was funded by ANID-FONDEQUIP instrumentation grant EQM120098. G.Palma thanks financial support provided by ANID-PFCHA/Doctorado Nacional/2016-2116003, through a PhD scholarship. We thank Nelson Román for his help with Principal Component Analysis (PCA). We also thank Dr. Xiao-Wen Huang, Ms. Joanna Chaves Araújo and editor Huayong Chen for their reviews and comments that helped improved this manuscript.

Appendix A. Supplementary data

Supplementary data to this article can be found online at https://doi.org/10.1016/j.oregeorev.2020.103748.

References

Araújo, J.C.S., Lobato, L.M., 2019. Depositional model for banded iron formation host to gold in the Archean Rio das Velhas greenstone belt, Brazil, based on geochemistry and LA-ICP-MS magnetite analyses. J. S. Am. Earth Sci. 94, 102205.
Angerer, T., Hagemann, S.G., Danyushevsky, L.V., 2012. Geochemical evolution of the banded iron formation-hosted high-grade iron ore system in the Koolyanobbing Greenstone Belt, Western Australia. Econ. Geol. 107, 599–644.
Apukhtina, O.B., Kamenetsky, V.S., Ehrig, K., Kamenetsky, M.B., Maas, R., Thompson, J., Cook, N.J., 2017. Early, deep magnetite-fluorapatite mineralization at the Olympic Dam Cu-U-Au-Ag deposit, South Australia. Econ. Geol. 112, 1531–1542.
Audétat, A., Keppler, H., 2005. Solubility of rutile in subduction zone fluids, as determined by experiments in the hydrothermal diamond anvil cell. Earth Planet. Sci. Lett. 232, 393–402.
Barra, F., Reich, M., Selby, D., Rojas, P., Simon, A., Salazar, E., Palma, G., 2017. Unraveling the origin of the Andean IOCG clan: a Re-Os isotope approach. Ore Geol. Rev. 81, 62–78.
Barton, M.D., Johnson, D.A., 1996. Evaporitic-source model for igneous-related Fe oxide–(REE-Cu-Au-U) mineralization. Geology 24, 259–262.
Barton, M.D., Johnson, D.A., 2004. In: Footprints of Fe-oxide (-Cu-Au) Systems. University of Western Australia Sp. Pub., pp. 112–116.
Barton, M.D., 2014. In: Iron Oxide (–Cu–Au–REE–P–Ag–U–Co) Systems. Treatise on Geochemistry, second ed. Elsevier, Amsterdam, pp. 515–541.
Benavides, J., Kyser, T.K., Clark, A.H., Oates, C.J., Zamora, R., Tarnovschi, R., Castillo, B., 2007. The Mantoverde iron oxide-copper-gold district, III Región, Chile: the role of regionally derived, nonmagmatic fluids in chalcopyrite mineralization. Econ. Geol. 102, 415–440.
Bilenker, L.D., Simon, A.C., Reich, M., Lundstrom, C.C., Gajos, N., Bindeman, I., Munizaga, R., 2016. Fe–O stable isotope pairs elucidate a high-temperature origin of Chilean iron oxide-apatite deposits. Geochim. Cosmochim. Acta 177, 94–104.
Boctor, N.Z., Popp, R.K., Frantz, J.D., 1980. Mineral-solution equilibria—IV. Solubilities and the thermodynamic properties of FeCl20 in the system Fe2O3-H2-H2O-HCl. Geochim. Cosmochim. Acta 44, 1509–1518.
Bonson, C., Grocott, J., Rankin, A., 1997. In: A Structural Model for the Development of Fe–Cu Mineralisation Coastal Cordillera, Northern Chile (25815VS–27815VS). Congreso Geológico Chileno. Universidad Católica del Norte, Antofagasta, Chile, pp. 1608–1612.
Broughm, S.G., Hanchar, J.M., Tornos, F., Westhues, A., Attersley, S., 2017. Mineral chemistry of magnetite from magnetite-apatite mineralization and their host rocks: examples from Kiruna, Sweden, and El Laco, Chile. Miner. Deposita 52, 1223–1244.
Brown, M., 1995. P-T–t evolution of orogenic belts and the causes of regional metamorphism. J. Geol. Soc. London 150, 227–241.
Brown, M., Diáz, F., Grocott, J., 1993. Displacement history of the Atacama fault system 25°00′S-27° 00′S, northern Chile. GSA Bull. 105 (9), 1165–1174.
Buddington, A.F., Lindsley, D.H., 1964. Iron-titanium oxide minerals and synthetic equivalents. J. Petrol. 5, 310–357.
CAP Minería Annual Report 2016 < http://www.capmineria.cl/wp-content/uploads/2017/03/cap_mineria_memoria_2016.pdf > .
Canil, D., Grondahl, C., Lacourse, T., Pisiak, L., 2016. Trace elements in magnetite from porphyry Cu–Mo–Au deposits in British Columbia, Canada. Ore Geol. Rev. 72 (1), 1116–1128.
Cembrano, J., González, G., Arancibia, G., Ahumada, I., Olivares, V., Herrera, V., 2005. Fault zone development and strain partitioning in an extensional strike-slip duplex: a case study from the Mesozoic Atacama fault system, Northern Chile. Tectonophysics 400, 105–125.
Charrier, R., Pinto, L., Rodríguez, M.P., 2007. Tectonostratigraphic evolution of the Andean Orogen in Chile. In: The Geology of Chile, pp. 21-114.
Chauvet, A., 2019. Structural control of ore deposits: the role of pre-existing structures on the formation of mineralised vein systems. Minerals 9, 56.
Chen, H., Clark, A.H., Kyser, T.K., 2010. The Marcona magnetite deposit, Ica, south-central Peru: a product of hydrous, iron oxide-rich melts? Econ. Geol. 105, 1441–1456.
Chen, H., Cooke, D.R., Baker, M.J., 2013. Mesozoic iron oxide copper-gold mineralization in the Central Andes and the Gondwana supercontinent Breakup. Econ. Geol. 108, 37–44.
Childress, T., Simon, A., Day, W.C., Lundstrom, C.C., Bindeman, I., 2016. Iron and oxygen isotope signatures of the Pea Ridge and Pilot Knob magnetite-apatite deposits, southeast Missouri, USA. Econ. Geol. 111, 2033–2044.
Childress, T., Simon, A.C., Reich, M., Barra, F., Arce, M., Lundstrom, C.C., Bindeman, I., 2020. Formation of the Mantoverde iron oxide - copper - gold deposit, Chile: Insights from Fe and O stable isotopes and comparisons to iron oxide - apatite deposits. Miner. Deposita. https://doi.org/10.1007/s00126-019-00936-x.
Chou, I.M., Eugster, H.P., 1977. Solubility of magnetite in supercritical chloride solutions. Am. J. Sci. 277, 1296–1314.
Ciobanu, C.L., Cook, N.J., 2004. Skarn textures and a case study: the Ocna de Fier-Dognecea orefield, Banat, Romania. Ore Geol. Rev. 24, 315–370.
Claeson, D.T., 1998. Coronas, reaction rims, symplectites and emplacement depth of the Rymmen gabbro, Transscandinavian Igneous Belt, southern Sweden. Miner. Mag. 62, 743–757.

Core, D.P., 2004. Oxygen and sulfur fugacities of granitoids: Implications for ore-forming processes. Ph.D. thesis. Ann Arbor, University of Michigan, pp. 245 p..
Correa, A., Hopper, D., 2000. The Panulcillo and Teresa de Colmo copper deposits: two contrasting examples of Fe-ox Cu-Au mineralization from the Coastal Cordillera of Chile. In: Porter, T.M. (Ed.), 2000 Hydrothermal Iron Oxide Copper-Gold & Related Deposits: A Global Perspective. PGC Publishing, Adelaide, pp. 177–189.
Cox, S.F., Knackstedt, M.A., Braun, J., 2001. Principles of structural control on permeability and fluid flow in hydrothermal systems. SEG Rev. 14, 1–24.
Craig, J.R., Vaughan, D.J., 1981. In: Ore Microscopy and Ore Petrography. Wiley, New York, pp. 434.
Dallmeyer, R.D., Brown, M., Grocott, J., Taylor, G.K., Treloar, P.J., 1996. Mesozoic magmatic and tectonic events within the Andean plate boundary zone, 26–27 30'S, north Chile: constraints from 40Ar/39Ar mineral ages. J. Geol. 104, 19–40.
Dare, S.A., Barnes, S.-J., Beaudoin, G., 2012. Variation in trace element content of magnetite crystallized from a fractioning sulfide liquid, Sudbury, Canada: Implications for provenance discrimination. Geochim. Cosmochim. Acta 88, 27–50.
Dare, S.A., Barnes, S.-J., Beaudoin, G., Méric, J., Boutroy, E., Potvin-Doucet, C., 2014. Trace elements in magnetite as petrogenetic indicators. Miner. Deposita 49, 785–796.
Dare, S.A., Barnes, S.-J., Beaudoin, G., 2015. Did the massive magnetite "lava flows" of El Laco (Chile) form by magmatic or hydrothermal processes? New constraints from magnetite composition by LA-ICP-MS. Miner. Deposita 50, 607–617.
Day, W.C., Slack, J.F., Ayuso, R.A., Seeger, C.M., 2016. Regional geologic and petrologic framework for iron oxide ± apatite ± rare earth element and iron oxide copper-gold deposits of the Mesoproterozoic St. Francois Mountains terrane, southeast Missouri, USA. Econ. Geol. 111, 1825–1858.
De Melo, G.H.C., Monteiro, L.V.S., Xavier, R.P., Moreto, C.P.N., Santiago, E.S.B., Dufrane, S.A., Aires, B., Santos, A.F.F., 2017. Temporal evolution of the giant Salobo IOCG deposit, Carajás Province (Brazil): constraints from paragenesis of hydrothermal alteration and U-Pb geochronology. Miner. Deposita 52, 709–732.
Deditius, A.P., Utsunomiya, S., Ewing, R.C., Chryssoulis, S.L., Venter, D., Kesler, S.E., 2009. Decoupled geochemical behavior of As and Cu in hydrothermal systems. Geology 37, 707–710.
Deditius, A.P., Reich, M., Simon, A.C., Suvorova, A., Knipping, J., Roberts, M.P., Saunders, M., 2018. Nanogeochemistry of hydrothermal magnetite. Contrib. Miner. Petrol. 173, 46.
Dégi, J., Abart, R., Török, K., Bali, E., Wirth, R., Rhede, D., 2010. Symplectite formation during decompression induced garnet breakdown in lower crustal mafic granulite xenoliths: mechanisms and rates. Contrib. Miner. Petrol. 159, 293–314.
Del Real, I., Thompson, F.H., Carriedo, J., 2018. Lithological and structural controls on the genesis of the Candelaria-Punta del Cobre Iron Oxide Copper Gold district, Northern Chile. Ore Geol. Rev. 102, 106–153.
Dowling, K., Morrison, G., 1990. Application of quartz textures to the classification of gold deposits using North Queensland examples. Econ. Geol. Monogr. 6, 342–1255.
Dupuis, C., Beaudoin, G., 2011. Discriminant diagrams for iron oxide trace element fingerprinting of mineral deposit types. Miner. Deposita 46, 319–335.
Edmonds, M., Brett, A., Herd, R.A., Humphreys, M.C.S., Woods, A., 2014, Magnetite-bubble aggregates at mixing interfaces in andesite magma bodies: Geol. Soc. London Sp. Pub. 410.
Elardo, S.M., McCubbin, F.M., Shearer Jr., C.K., 2012. Chromite symplectites in Mg-suite troctolite 76535 as evidence for infiltration metasomatism of a lunar layered intrusion. Geochim. Cosmochim. Acta 87, 154–177.
Espinoza, R.S., Véliz, G.H., Esquivel, L.J, Arias, F.J., Moraga, B.A., 1996. The cupriferous province of the Coastal Range, northern Chile. Andean copper deposits: New discoveries, mineralization, styles and metallogeny, SEG Sp. Pub. 5, pp. 19–32.
Field, S., 2008. Diffusion, discontinuous precipitation, metamorphism, and metasomatism: the complex history of South African upper-mantle symplectites. Am. Mineral. 93, 618–631.
Frost, B.R., Lindsley, D., 1991. Oxide minerals: petrologic and magnetic significance. Rev. Mineral. Soc. Am. 25, 509.
Frutos, J., Oyarzún, M.J., 1975. Tectonic and geochemical evidence concerning the genesis of El Laco magnetite lava flow deposits, Chile. Econ. Geol. 70, 988–990.
Gelcich, S., David, D., Spooner, E., 2005. Testing the apatite-magnetite geochronometer: UPb and 40Ar/ 39Ar geochronology of plutonic rocks, massive magnetite-apatite tabular bodies, and IOCG mineralization in Northern Chile. Geochim. Cosmochim. Acta 69, 3367–3384.
Gelcich, S., Davis, D., Spooner, E., 2002. New U-Pb ages from host rocks, mineralization and alteration of iron oxide (Cu-Au) deposits in the Coastal Cordillera of Northern Chile. In: IV South American Symposium on Isotope Geology, Salvador de Bahia, Brazil 63–65.
Gregory, D., Large, R., Halpin, J., Baturina, E., Lyons, T., Wu, S., Danyushevsky, L., Sack, P., Chappaz, A., Maslennikov, V., Bull, S., 2015. Trace element content of sedimentary pyrite in black shales. Econ. Geol. 110, 1389–1410.
Grocott, J., Taylor, G.K., 2002. Magmatic arc fault systems, deformation partitioning and emplacement of granitic complexes in the Coastal Cordillera, north Chilean Andes (25 30′ S to 27 00′ S). J. Geol. Soc. London 159, 425–443.
Groves, D.I., Bierlein, F.P., Meinert, L.D., Hitzman, M.W., 2010. Iron oxide copper-gold (IOCG) deposits through Earth history: Implications for origin, lithospheric setting, and distinction from other epigenetic iron oxide deposits. Econ. Geol. 105, 641–654.
He, H.L., Song, Y.Y., Song, Y.X., Du, Z.S., Dai, Z.H., Zhou, T., Xie, W., 2016. Origin of nelsonite and Fe–Ti oxides ore of the Damiao anorthosite complex, NE China: evidence from trace element geochemistry of apatite, plagioclase, magnetite and ilmenite. Ore Geol. Rev. 79, 367–381.
Heidarian, H., Lentz, D., Alirezaei, S., Peighambari, S., Hall, D., 2016. Using the chemical analysis of magnetite to constrain various stages in the formation and genesis of the Kiruna-type chadormalu magnetite-apatite deposit, Bafq district, Central Iran. Miner. Petrol. 110, 927–942.
Herrera, V., Cembrano, J., Olivares, V., Kojima, S., Arancibia, G., 2005. Precipitación por despresurización y ebullición en vetas hospedadas en un dúplex de rumbo extensional: evidencias microestructurales y microtermométricas. Rev. Geol. de Chile 32, 207–228.
Hezarkhani, A., Williams-Jones, A.E., Gammons, C.H., 1999. Factors controlling copper solubility and chalcopyrite deposition in the Sungun porphyry copper deposit, Iran. Miner. Deposita 34, 770–783.
Hippertt, J.F., Valarelli, J.V., 1998. Myrmekite: constraints on the available models and a new hypothesis for its formation. Eur. J. Mineral. 317–332.
Hitzman, M.W., Oreskes, N., Einaudi, M.T., 1992. Geological characteristics and tectonic setting of proterozoic iron oxide (Cu U Au REE) deposits. Precambr. Res. 58, 241–287.
Holten, T., Jamtveit, B., Meakin, P., 2000. Noise and oscillatory zoning of minerals. Geochim. Cosmochim. Acta 64, 1893–1904.
Huberty, J.M., Konishi, H., Heck, P.R., Fournelle, J.H., Valley, J.W., Xu, H., 2012. Silician magnetite from the Dales Gorge Member of the Brockman Iron Formations, Hamersley Group, Western Australia. Am. Mineral. 97, 26–37.
Hu, H., Li, J.W., Lentz, D., Ren, Z., Zhao, X., Deng, X.D., Hall, D., 2014. Dissolution-reprecipitation process of magnetite from the Chengchao iron deposit: insights into ore genesis and implication for in-situ chemical analysis of magnetite. Ore Geol. Rev. 57, 393–405.
Hu, H., Lentz, D., Li, J.W., McCarron, T., Zhao, X.F., Hall, D., 2015. Reequilibration processes in magnetite from iron skarn deposits. Econ. Geol. 111, 1–8.
Huang, X.W., Gao, J.F., Qi, L., Meng, Y.M., Wang, Y.C., Dai, Z.H., 2016. In-situ LA-ICP-MS trace element analysis of magnetite: The Fenghuangshan Cu-Fe-Au deposit, Tongling, Eastern China. Ore Geol. Rev. 72, 746–759.
Huang, X.W., Zhou, M.F., Beaudoin, G., Gao, J.F., Qi, L., Lyu, C., 2018. Origin of the volcanic-hosted Yamansu Fe deposit, Eastern Tianshan, NW China: constraints from pyrite Re-Os isotopes, stable isotopes, and in situ magnetite trace elements. Miner. Deposita 53, 1039–1060.
Huang, X.W., Beaudoin, G., 2019. Textures and chemical compositions of magnetite from iron oxide copper-gold (IOCG) and Kiruna-type iron oxide-apatite (IOA) deposits and their implications for ore genesis and magnetite classification schemes. Econ. Geol. 114, 1–74.
Huang, W.W., Sappin, A.A., Boutroy, E., Beaudoin, G., Makvandi, S., 2019. Trace Element Composition of Igneous and Hydrothermal Magnetite from Porphyry Deposits: Relationship to Deposit Subtypes and Magmatic Affinity. Econ. Geol. 114, 917–952.
Hurtig, N.C., Williams-Jones, A.E., 2014. An experimental study of the transport of gold through hydration of AuCl in aqueous vapour and vapour-like fluids. Geochim. Cosmochim. Acta 127, 305–325.
Ilton, E.S., Eugster, H.P., 1989. Base metal exchange between magnetite and a chloride-rich hydrothermal fluid. Geochim. Cosmochim. Acta 53, 291–301.
James, B.R., 2003. Chromium. In Encyclopedia of Water Science. In: B.A. Stewart and T. A. Howell (Eds.). Marcel Dekker Inc, pp.77-82.
Jenkins, D.M., 1983. Stability and composition relations of calcic amphiboles in ultramafic rocks. Contrib. Miner. Petrol. 83, 375–384.
Jochum, K.P., Willbold, M., Raczek, I., Stoll, B., Herwig, K., 2005. Chemical characterisation of the USGS reference glasses GSA-1G, GSC-1G, GSD-1G, GSE-1G, BCR-2G, BHVO-2G and BIR-1G using EPMA, ID-TIMS, ID-ICP-MS and LA-ICP-MS. Geostand. Geoanal. Res. 29, 285–302.
Jonsson, E., Troll, V.R., Högdahl, K., Harris, C., Weis, F., Nilsson, K.P., Skelton, A., 2013. Magmatic origin of giant 'Kiruna-type'apatite-iron-oxide ores in Central Sweden. Sci. Rep. 3, 1644.
Knipping, J.L., Bilenker, L.D., Simon, A.C., Reich, M., Barra, F., Deditius, A.P., Munizaga, R., 2015a. Giant Kiruna-type deposits form by efficient flotation of magmatic magnetite suspensions. Geology 43, 591–594.
Knipping, J.L., Bilenker, L.D., Simon, A.C., Reich, M., Barra, F., Deditius, A.P., Munizaga, R., 2015b. Trace elements in magnetite from massive iron oxide-apatite deposits indicate a combined formation by igneous and magmatic-hydrothermal processes. Geochim. Cosmochim. Acta 171, 15–38.
Knipping, J.L., Fiege, A., Simon, A.C., Oeser-Rabe, M., Reich, M., Bilenker, L., 2019a. In-situ iron isotope analyses reveal igneous and magmatic-hydrothermal growth of magnetite at the Los Colorados Kiruna-type iron oxide-apatite deposit, Chile. Am. Mineral. 104, 471–484.
Knipping, J., Webster, J.D., Simon, A.C., Holtz, F., 2019b. Accumulation of magnetite by flotation on bubbles during decompression of silicate magma. Sci. Rep. 9, 3852.
La Cruz, N.L., Simon, A.C., Wolf, A.S., Reich, M., Barra, F., Gagnon, J.E., 2019. The geochemistry of apatite from the Los Colorados iron oxide–apatite deposit, Chile: implications for ore genesis. Miner. Deposita 54, 1143–1156.
La Cruz, N.L., Ovalle, J.T., Simon, A.C., Konecke, B.A., Barra, F., Leisen, M., Reich, M., Childress, T.M., 2020. The geochemistry of magnetite and apatite from the El Laco iron oxide-apatite deposit, Chile: Implications for ore genesis: Econ. Geol. https://doi.org/10.5382/econgeo.4753.
Lattard, D., 1995. Experimental evidence for the exsolution of ilmenite from titaniferous spinel. Am. Mineral. 80, 968–981.
Liu, W., Zhang, J., Sun, T., Wang, J., 2014. Application of apatite U-Pb and fission-track double dating to determine the preservation potential of magnetite–apatite deposits in the Luzong and Ningwu volcanic basins, eastern China. J. Geochem. Explor. 138, 22–32.
Liu, P.P., Zhou, M.F., Chen, W.T., Gao, J.F., Huang, X.W., 2015. In situ LA-ICP-MS trace elemental analyses of magnetite: Fe-Ti-(V) oxide-bearing mafic-ultramafic layered intrusions of the Emeishan Large Igneous Province, SW China. Ore Geol. Rev. 65, 853–871.
Loberg, B.E., Horndahl, A.K., 1983. Ferride geochemistry of Swedish Precambrian iron ores. Miner. Deposita 18, 487–504.
Longerich, H.P., Günther, D., Jackson, S.E., 1996. Elemental fractionation in laser

ablation inductively coupled plasma mass spectrometry. Fresenius' J. Analyt. Chem 355, 538–542.
Maksaev, V., Gardeweg, M., Ramírez, C.F.,. Zentilli, M., 1988. Aplicación del método trazas de fisión (fission track) a la datación de cuerpos de magnetita de El Laco e Incahuasi en el altiplano de la Región de Antofagasta. In: Congreso Geológico Chileno, No. 5, v. 1: B1–B23.
Makvandi, S., Ghasemzadeh-Barvarz, M., Beaudoin, G., Grunsky, E.C., McClenaghan, M.B., Duchesne, C., 2016. Principal component analysis of magnetite composition from volcanogenic massive sulfide deposits: case studies from the Izok Lake (Nunavut, Canada) and Halfmile Lake (New Brunswick, Canada) deposits. Ore Geol. Rev. 72, 60–85.
Marschik, R., Leveille, R.A., Martin, W., 2000. La Candelaria and the Punta del Cobre district, Chile: Early Cretaceous iron-oxide Cu-Au (-Zn-Ag) mineralization. In: Porter, T.M. (Ed.), Hydrothermal Iron Oxide Copper-Gold & Related Deposits: A Global Perspective. PGC Publishing, Adelaide, pp. 163–175.
Marschik, R., Fontboté, L., 2001. The Candelaria-Punta del Cobre iron oxide Cu-Au (-Zn-Ag) deposits, Chile. Econ. Geol. 96, 1799–1826.
Mathur, R., Marschick, R., Ruiz, J., Munizaga, F., Leveille, R., Martin, W., 2002. Age of Mineralization of the Candelaria Fe Oxide Cu-Au Deposit and the Origin of the Chilean Iron Belt, Based on Re-Os Isotopes. Econ. Geol. 97 (1), 59–71.
Migdisov, A.A., Bychkov, A.Y., Williams-Jones, A.E., van Hinsberg, V.J., 2014. A predictive model for the transport of copper by HCl-bearing water vapour in ore-forming magmatic-hydrothermal systems: Implications for copper porphyry ore formation. Geochim. Cosmochim. Acta 129, 33–53.
Moncada, D., Mutchler, S., Nieto, A., Reynolds, T.J., Rimstidt, J.D., Bodnar, R.J., 2012. Mineral textures and fluid inclusion petrography of the epithermal Ag–Au deposits at Guanajuato, Mexico: Application to exploration. J. Geochem. Explor. 114, 20–35.
Mongkoltip, P., Ashworth, J.R., 1983. Quantitative estimation of an open-system symplectite-forming reaction: restricted diffusion of Al and Si in coronas around olivine. J. Petrol. 24, 635–661.
Monteiro, L.V.S., Xavier, R.P., Carvalho, E.R., Hitzman, M.W., Johnson, C.A., Souza Filho, C.R., Torresi, I., 2008a. Spatial and temporal zoning of hydrothermal alteration and mineralization in the Sossego iron oxide-copper-gold deposit, Carajás Mineral Province, Brazil: Paragenesis and stable isotope constraints. Miner. Deposita 43, 129–159.
Monteiro, L.V.S., Xavier, R.P., Hitzman, M.W., Juliani, C., Souza Filho, C.R., Carvalho, E.R., 2008b. Mineral chemistry of ore and hydrothermal alteration at the Sossego iron oxide–copper–gold deposit, Carajás Mineral Province. Brazil. Ore Geol. Rev. 34, 317–336.
Morrison, G.W., Teale, G.S., Hodkinson, I., 1990. Geology and gold mineralisation at Mount Leyshon, north Queensland. In: Gold update 89-90, course manual. Gold bearing breccias: Characteristics, genesis and exploration, pp. 71-74.
Moseley, D., 1984. Symplectic exsolution in olivine. Am. Mineral. 69, 139–153.
Mpodozis, C., Ramos, V., 1989. The Andes of Chile and Argentina. In: Geology of the Andes and its relation to hydrocarbon and mineral resources; Ericksen, G.E., Cañas M. T. and Reinemund, J.A. (Eds), Houston, Texas, Circum-Pacific Council for Energy and Mineral Resources, Earth Science Series, vol. 11, pp. 59-90.
Mücke, A., 2003. General and comparative considerations of whole-rock and mineral compositions of Precambrian iron-formations and their implications. Neues Jahrbuch für Mineralogie-Abhandlungen. J. Mineral. Geochem. 179, 175–219.
Mumin, A.H., Corriveau, L., Somarin, A.K., Ootes, L., 2007. Iron oxide copper-gold-type polymetallic mineralization in the Contact Lake belt, Great Bear magmatic zone, Northwest Territories, Canada: Explor. Min. Geol. 16, 187–208.
Nadoll, P., Mauk, J.L., Hayes, T.S., Koenig, A.E., Box, S.E., 2012. Geochemistry of magnetite from hydrothermal ore deposits and host rocks of the Mesoproterozoic Belt Supergroup. USA. Econ. Geol. 107, 1275–1292.
Nadoll, P., Angerer, T., Mauk, J.L., French, D., Walshe, J., 2014. The chemistry of hydrothermal magnetite: a review. Ore Geol. Rev. 61, 1–32.
Nadoll, P., Mauk, J.L., Leveille, R.A., Koenig, A.E., 2015. Geochemistry of magnetite from porphyry Cu and skarn deposits in the southwestern United States. Miner. Deposita 50, 493–515.
Naranjo, J.A., Henríquez, F., Nyström, J.O., 2010. Subvolcanic contact metasomatism at El Laco volcanic complex, central Andes. Andean Geol. 37, 110–120.
Naslund, H.R., Henríquez, F., Nyström, J.O., Vivallo, W., Dobbs, F.M., 2002. Magmatic iron ores and associated mineralisation: examples from the Chilean high Andes and coastal Cordillera. In: Hydrothermal Iron Oxide-Copper-Gold: A Global Perspective. T.M. Porter (Ed.), PGC Publishing, Adelaide, Australia, vol. 2, pp. 207-226.
Newberry, N.G., Peacor, D.R., Essene, E.J., Geissman, J.W., 1982. Silicon in magnetite: high resolution microanalysis of magnetite-ilmenite intergrowths. Contrib. Miner. Petrol. 80, 334–340.
Nold, J.L., Davidson, P., Dudley, M.A., 2013. The Pilot Knob magnetite deposit in the Proterozoic St. Francois Mountains terrane, southeast Missouri, USA: A magmatic and hydrothermal replacement iron deposit. Ore Geol. Rev. 53, 446–469.
Nyström, J.O., Henríquez, F., 1994. Magmatic features of iron ores of the Kiruna-type in Chile and Sweden: ore textures and magnetite geochemistry. Econ. Geol. 89, 820–839.
Olivares, V., Cembrano, J., Arancibia, G., Reyes, N., Herrera, V., Faulkner, D., 2010. Significado tectónico y migración de fluidos hidrotermales en una red de fallas y vetas de un Dúplex de rumbo: un ejemplo del Sistema de Falla de Atacama. Andean Geol. 37, 473–497.
Oliveros, V., Féraud, G., Aguirre, L., Fornari, M., Morata, D., 2006. The Early Andean Magmatic Province (EAMP): 40Ar/39Ar dating on Mesozoic volcanic and plutonic rocks from the Coastal Cordillera, northern Chile. J. Volcanol. Geoth. Res. 157, 311–330.
Ovalle, J.T., La Cruz, N.L., Reich, M., Barra, F., Simon, A.C., Konecke, B.A., Morata, D., 2018. Formation of massive iron deposits linked to explosive volcanic eruptions. Sci. Rep. 8, 14855.
Oyarzún, J., Frutos, J., 1984. Tectonic and petrological frame of the Cretaceous iron deposits of north Chile. Min. Geol. 34, 21–31.
Oyarzún, R., Oyarzún, J., Ménard, J.J., Lillo, J., 2003. The Cretaceous iron belt of northern Chile: role of oceanic plates, a superplume event, and a major shear zone. Miner. Deposita 38, 640–646.
Palma, G., Barra, F., Reich, M., Valencia, V., Simon, A.C., Vervoort, J., Romero, R., 2019. Halogens, trace element concentrations, and Sr-Nd isotopes in apatite from iron oxide-apatite (IOA) deposits in the Chilean iron belt: Evidence for magmatic and hydrothermal stages of mineralization. Geochim. Cosmochim. Acta 246, 515–540.
Pang, K.N., Li, C., Zhou, M.F., Ripley, E.M., 2008. Abundant Fe–Ti oxide inclusions in olivine from the Panzhihua and Hongge layered intrusions, SW China: evidence for early saturation of Fe–Ti oxides in ferrobasaltic magma. Contrib. Miner. Petrol. 156, 307–321.
Pang, K.N., Zhou, M.F., Qi, L., Shellnutt, G., Wang, C.Y., Zhao, D., 2010. Flood basalt-related Fe–Ti oxide deposits in the Emeishan large igneous province, SW China. Lithos 119, 123–136.
Paton, C., Hellstrom, J., Paul, B., Woodhead, J., Hergt, J., 2011. Iolite: Freeware for the visualization and processing of mass spectrometric data. J. Anal. At. Spectrom. 26, 2508–2518.
Peterson, E.C., Mavrogenes, J.A., 2014. Linking high-grade gold mineralization to earthquake-induced fault-valve processes in the Porgera gold deposit, Papua New Guinea. Geology 42, 383–386.
Pichon, R., 1981. Ph.D. thesis, Univ. Paris Xl (Orsay).
Pincheira, M., Thiele, R., Fontbote, L., 1990. Tectonic transpression along the southern segment of the Atacam Fault-Zone, Chile. in Proceedings, Symposium International "Géodynamique Andine", Grenoble, 15–17 May (Colloques et Seminaires): Paris, ORSTOM 133–136.
Polivchuk, M., 2017. The Formation of Vanadium Deposits in the Archean Rivière Bell Complex, Quebec: Insights from Fe-Ti Oxide Chemistry. PhD thesis. Univ. of Ottawa.
Pollard, P.J., 2006. An intrusion-related origin for Cu–Au mineralization in iron oxide–copper–gold (IOCG) provinces. Miner. Deposita 41, 179.
Putnis, A., 2009. Mineral replacement reactions. Rev. Mineral. Geochem. 70, 87–124.
Raab, A., 2001. Geology of the Cerro Negro Norte Fe-oxide (Cu-Au) District. MSc thesis. Oregon State Univ, Coastal Cordillera, northern Chile, pp. 273 p..
Ramos, V.A., 2010. The tectonic regime along the Andes: Present day and Mesozoic regimes. Geol. J. 45, 2–25.
Regan, S., Lupulescu, M., Jercinovic, M., Chiarenzelli, J., Williams, M., Singer, J., Bailey, D., 2019. Age and Origin of Monazite Symplectite in an Iron Oxide-Apatite Deposit in the Adirondack Mountains, New York, USA: Implications for Tracking Fluid Conditions. Minerals 9, 65.
Reich, M., Deditius, A., Chryssoulis, S., Li, J.W., Ma, C.Q., Parada, M.A., Mittermayr, F., 2013. Pyrite as a record of hydrothermal fluid evolution in a porphyry copper system: A SIMS/EMPA trace element study. Geochim. Cosmochim. Acta 104, 42–62.
Reich, M., Simon, A.C., Deditius, A., Barra, F., Chryssoulis, S., Lagas, G., Roberts, M.P., 2016. Trace element signature of pyrite from the Los Colorados iron oxide-apatite (IOA) deposit, Chile: A missing link between Andean IOA and iron oxide copper-gold systems? Econ. Geol. 111, 743–761.
Rhodes, A.L., Oreskes, N., 1995. Magnetite deposition at El Laco, Chile: implications for Fe-oxide formation in magmatic-hydrothermal systems. In: Giant ore deposits-II: Controls on the scale of orogenic magmatic-hydrothermal mineralization. Clark, A.H. (Ed.), Proceedings of the Second Giant Ore Deposits Workshop, Queen's University: 582-622. Kingston, Ontario, Canada.
Rhodes, A.L., Oreskes N., 1999. Oxygen isotope composition of magnetite deposits at El Laco, Chile: Evidence of formation from isotopically heavy fluids. In: Geology and Ore Deposits of the Central Andes, B.J. Skinner (Ed.) SEG Sp. Pub. 7, 333-351.
Rhodes, A.L., Oreskes, N., Sheets, S., 1999. Geology and rare earth element geochemistry of magnetite deposits at El Laco, Chile. SEG Sp. Pub. 7, 299–332.
Richards, J.P., López, G.P., Zhu, J.-J., Creaser, R.A., Locock, A.J., Mumim, A.H., 2017. Constrasting tectonic setting and sulfur contents of magmas associated with Cretaceous Porphyry Cu ± Mo ± Au and intrusion-related Iron Oxide Cu-Au deposits in northern Chile. Econ. Geol. 112, 295–318.
Rieger, A.A., Marschik, R., Díaz, M., Hölzl, S., Chiaradia, M., Akker, B., Spangenberg, J.E., 2010. The hypogene iron oxide copper-gold mineralization in the Mantoverde district, northern Chile. Econ. Geol. 105, 1271–1299.
Rieger, A.A., Marschik, R., Díaz, M., 2012. The evolution of the hydrothermal IOCG system in the Mantoverde district, northern Chile: new evidence from microthermometry and stable isotope geochemistry. Miner. Deposita 47, 359–369.
Río Tinto internal report., 2001. Sofía Prospect Final Report , Region II, Antofagasta, Chile.
Rodriguez-Mustafa, M.A., Simon, A.C., Del Real, I., Thompson, J.F.H., Bilenker, L.D., Barra, F., Bindeman, I. 2020, A Continuum from Iron Oxide-Copper-Gold (IOCG) to Iron Oxide-Apatite (IOA) Deposits: Evidence from Fe and O Stable Isotopes and Trace Element Chemistry of Magnetite, Econ. Geol. doi:10.5382/econgeo.4752.
Rojas, P., Barra, F., Reich, M., Deditius, A., Simon, A., Uribe, F., Romero, R., Rojo, M., 2018a. A genetic link between magnetite mineralization and diorite intrusion at the El Romeral iron oxide-apatite deposit, northern Chile. Miner. Deposita 53, 947–966.
Rojas, P., Barra, F., Deditius, A., Reich, M., Simon, A., Roberts, M., Rojo, M., 2018b. New contributions to the understanding of Kiruna-type iron oxide-apatite deposits revealed by magnetite ore and gangue mineral geochemistry at the El Romeral deposit. Chile. Ore Geol. Rev. 93, 413–435.
Rusk, B., Oliver, N., Cleverley, J., Blenkinsop, T., Zhang, D., Williams, P., Habermann, P., 2010. Physical and chemical characteristics of the Ernest Henry iron oxide copper gold deposit, Australia; implications for IOGC genesis. In Implications for IOGC Genesis; PGC Publishing: Adelaide, Australia.
Román, N., Reich, M., Leisen, M., Morata, D., Barra, F., 2019. Geochemical and micro-

textural fingerprints of boiling in pyrite. Geochim. Cosmochim. Acta 246, 60–85.
Sanchez-Alfaro, P., Reich, M., Arancibia, G., Driesner, T., Pérez-Flores, P., Cembrano, J., Heinrich, C., Rowland, J., Tardani, D., Campos, E., 2016. The optimal windows for seismically-enhanced gold precipitation in the epithermal environment. Ore Geol. Rev. 79, 463–473.
Salazar, E., Barra, F., Reich, M., Simon, A., Leisen, M., Palma, G., Rojo, M., 2020. Trace element geochemistry of magnetite from the Cerro Negro Norte iron oxide − apatite deposit, northern Chile. Miner. Deposita, 55, 409-428 (2020). doi:10.1007/s00126-019-00879-3.
Scheuber, E., Andriessen, P.A., 1990. The kinematic and geodynamic significance of the Atacama fault zone, northern Chile. J. Struct. Geol. 12, 243–257.
Scheuber, E., Bogdanic, T., Jensen, A., Reutter, K.J., 1994. Tectonic development of the north Chilean Andes in relation to plate convergence and magmatism since the Jurassic. In: Tectonics of the southern central Andes. Springer, Berlin, Heidelberg, pp. 121–139.
Scheuber, E., González, G., 1999. Tectonics of the Jurassic-Early Cretaceous magmatic arc of the north Chilean Coastal Cordillera (22°-26° S): a story of crustal deformation along a convergent plate boundary. Tectonics 18, 859–910.
Shimazaki, H., 1998. On the occurrence of silician magnetites. Resour. Geol. 48, 23–29.
Shore, M., Fowler, A.D., 1996. Oscillatory zoning in minerals; a common phenomenon. Can. Mineral. 34, 1111–1126.
Sibson, R.H., Moore, J.M.M., Rankin, A.H., 1975. Seismic pumping—a hydrothermal fluid transport mechanism. J. Geol. Soc. London 1316, 653–659.
Sibson, R.H., 2001. Seismogenic framework for hydrothermal transport and ore deposition. Rev. Econ. Geol. 14, 25–50.
Sievwright, R.H., Wilkinson, J.J., O'Neill, H.S.C., Berry, A.J., 2017. Thermodynamic controls on element partitioning between titanomagnetite and andesitic–dacitic silicate melts. Contrib. Miner. Petrol. 172, 62.
Sillitoe, R., 1979. Some thoughts on gold-rich porphyry copper deposits. Miner. Deposita 14, 161–174.
Sillitoe, R., Burrows, D., 2002. New field evidence bearing on the origin of the El Laco magnetite deposit, northern Chile. Econ. Geol. 97, 1101–1109.
Sillitoe, R., 2003. Iron oxide–copper–gold deposits: An Andean view. Miner. Deposita 38, 787–812.
Simon, A.C., Pettke, T., Candela, P.A., Piccoli, P.M., Heinrich, C.A., 2004. Magnetite solubility and iron transport in magmatic-hydrothermal environments. Geochim. Cosmochim. Acta 68, 4905–4914.
Simon, A.C., Ripley, E.M., 2011. The role of magmatic sulfur in the formation of ore deposits. Rev. Mineral. Geochem. 73, 513–578.
Simon, A.C., Kniping, J., Reich, M., Barra, F., Deditius, A.P., Bilenker, L., Childress, T., 2018. Kiruna-Type Iron Oxide-Apatite (IOA) and Iron Oxide Copper-Gold (IOCG) Deposits form by a combination of igneous and magmatic-hydrothermal processes: evidence from the Chilean Iron Belt. SEG Sp. Pub. 21, 89–114.
Song, X.Y., Qi, H.W., Hu, R.Z., Chen, L.M., Yu, S.Y., Zhang, J.F., 2013. Formation of thick stratiform Fe-Ti oxide layers in layered intrusion and frequent replenishment of fractionated mafic magma: Evidence from the Panzhihua intrusion. SW China. Geochem Geophys. 14, 712–732.
Sossi, P.A., Prytulak, J., O'Neill, H.S.C., 2018. Experimental calibration of vanadium partitioning and stable isotope fractionation between hydrous granitic melt and magnetite at 800 C and 0.5 GPa. Contrib. Miner. Petrol. 173, 27.
Staudigel, H., Schreyer, W., 1977. The upper thermal stability of clinochlore, $Mg_5Al[AlSi_3O_{10}](OH)_8$, at 10–35 kb PH_2O. Contrib. Miner. Petrol. 61, 187–198.
Tan, W., Wang C,Y., He, H., Xing, C., Liang, X.L., Dong, H. 2015. Magnetite-rutile symplectite derived from ilmenite-hematite solid solution in the Xinjie Fe-Ti oxide-bearing, mafic-ultramafic layered intrusion (SW China) Am. Mineral., 100, 2348–2351.
Tan, W., Liu, P., 2016. Mineralogy and origin of exsolution in ti-rich magnetite from different magmatic fe-ti oxide-bearing intrusions. Can. Mineral. 54, 539–553.
Tanis, E.A., Simon, A.C., Zhang, Y., Chow, P., Xiao, Y., Hanchar, J.M., Tschauner, O., Shen, G., 2016. Rutile solubility in NaF-NaCl-KCl-bearing aqueous fluids at 0.5-2.79 GPa and 250–650°C. Geochim. Cosmochim. Acta 177, 170–181.
Tardani, D., Reich, M., Deditius, A.P., Chryssoulis, S., Sánchez-Alfaro, P., Wrage, J., Roberts, M.P., 2017. Copper–arsenic decoupling in an active geothermal system: A link between pyrite and fluid composition. Geochim. Cosmochim. Acta 204, 179–204.
Toplis, M.J., Corgne, A., 2002. An experimental study of element partitioning between magnetite, clinopyroxene and iron-bearing silicate liquids with particular emphasis on vanadium. Contrib. Miner. Petrol. 144, 22–37.
Tornos, F., Velasco, F., Hanchar, J.M., 2016. Iron-rich melts, magmatic magnetite, and superheated hydrothermal systems: The El Laco deposit, Chile. Geology 44, 427–430.
Treloar P.J., Colley, H., 1993. Magnetite-apatite ores in the Atacama Fault Zone, El Salvador Region, northern Chile. Second ISAG, Oxford (UK), 21-23/9/1993.
Treloar, P.J., Colley, H., 1996. Variations in F and Cl contents in apatites from magnetite-apatite ores in northern chile, and their ore-genetic implications. Mineral. Mag. 60, 285–301.
Ulrich, T., Gunther, D., Heinrich, C.A., 2001. The evolution of a porphyry Cu-Au deposit, based on LA-ICP-MS analysis of fluid inclusions: Bajo de la Alumbrera, Argentina: Econ. Geol. 96, 1743–1774.
Uyeda, S., Kanamori, H., 1979. Back-arc opening and the mode of subduction. J. Geophys. Res. 84, 1049–1061.
Velasco, F., Tornos, F., Hanchar, J.M., 2016. Immiscible iron-and silica-rich melts and magnetite geochemistry at the El Laco volcano (northern Chile): Evidence for a magmatic origin for the magnetite deposits. Ore Geol. Rev. 79, 346–366.
Vivallo, W., Henríquez, F., Espinoza, S., 1994. Oxygen and sulfur isotopes in hydrothermally altered rocks and gypsum deposits at El Laco mining district, northern Chile. Comunicaciones [Departamento de Geología, Universidad de Chile] n 45, 93–100.
Vivallo, W., Espinoza, S., Henriquez, F., 1995. Metasomatismo y alteración hidrotermal en el distrito ferrífero Cerro Negro Norte, Copiapó, Chile. Andean Geol. 22, 75–88.
Von Gruenewaldt, G., Sharpe, M.R., Hatton, C.J., 1985. The Bushveld Complex; introduction and review. Econ. Geol. 80, 803–812.
Wang, C.Y., Zhou, M.F., Zhao, D.G., 2008. Fe-Ti-Cr oxides from the Permian Xinjie mafic-ultramafic layered intrusion in the Emeishan large igneous province, SW China: crystallization from Fe- and Ti-rich basaltic magmas. Lithos 102, 198–217.
Weis, F., Troll, V., Jonsson, E., Högdahl, K., Barker, A., Harris, C., Nilsson, K.P., 2013. Iron and oxygen isotope characteristics of apatite-iron-oxide ores from central Sweden. In: Mineral deposit research for a high-tech world, pp. 1675-1678.
Wen, G., Li, J.W., Hofstra, A.H., Koenig, A.E., Lowers, H.A., Adams, D., 2017. Hydrothermal reequilibration of igneous magnetite in altered granitic plutons and its implications for magnetite classification schemes: Insights from the Handan-Xingtai iron district. North China Craton. Geochim. Cosmochim. Acta 213, 255–270.
Westhues, A., Hanchar, J.M., Whitehouse, M.J., Martinsson, O., 2016. New constraints on the timing of host-rock emplacement, hydrothermal alteration, and iron oxide-apatite mineralization in the Kiruna district, Norrbotten. Sweden. Econ. Geol. 111, 1595–1618.
Westhues, A., Hanchar, J.M., LeMessurier, M.J., Whitehouse, M.J., 2017a. Evidence for hydrothermal alteration and source regions for the Kiruna iron oxide–apatite ore (northern Sweden) from zircon Hf and O isotopes. Geology 45, 571–574.
Westhues, A., Hanchar, J.M., Voisey, C.R., Whitehouse, M.J., Rossman, G.R., Wirth, R., 2017b. Tracing the fluid evolution of the Kiruna iron oxide apatite deposits using zircon, monazite, and whole rock trace elements and isotopic studies. Chem. Geol. 466, 303–322.
Williams, P.J., Barton, M.D., Fontbote, L., de Haller, A., Johnson, D.A., Mark, G., Marschik, R., Oliver, N.H.S., 2005. Iron oxide-copper-gold deposits: Geology, space-time distribution, and possible modes of origin. Econ. Geol. 100th Anniv. Vol, 371–406.
Williams-Jones, A.E., Heinrich, C.A., 2005. Vapor transport of metals and the formation of magmatic-hydrothermal ore deposits. Econ. Geol. 100th Anniv. Vol, 1287–1312.
Williams-Jones, A.E., Migdisov, A.A., 2014. Experimental constraints on the transport and deposition of metals in ore-forming hydrothermal systems: SEG Sp. Pub. 18, 77–95.
Yin, S., Ma, C., Robinson, P.T., 2017. Textures and high field strength elements in hydrothermal magnetite from a skarn system: Implications for coupled dissolution-re-precipitation reactions. Am. Mineral. 102, 1045–1056.
Zajacz, Z., Candela, P.A., Piccoli, P.M., Sanchez-Valle, C., 2012a. The partitioning of sulfur and chlorine between andesite melts and magmatic volatiles and the exchange coefficients of major cations. Geochim. Cosmochim. Acta 89, 81–101.
Zajacz, Z., Candela, P.A., Piccoli, P.M., Wälle, M., Sanchez-Valle, C., 2012b. Gold and copper in volatile saturated mafic to intermediate magmas: Solubilities, partitioning, and implications for ore deposit formation. Geochim. Cosmochim. Acta 91, 140–159.
Zhang, C., Vervoort, J., Barra, F., Palma, G., 2017. ICPMS Lu-Hf Geochronology of Apatite from Iron-Oxide Apatite (IOA) Deposits, Northern Chilean Iron Belt. VOlcanology, Geochemistry, and Petrology General contributionsAGU Fall Meeting (Abstract #236799).
Zhou, M.F., Robinson, P.T., Lesher, C.M., Keays, R.R., Zhang, C.J., Malpas, J., 2005. Geochemistry, petrogenesis and metallogenesis of the Panzhihua gabbroic layered intrusion and associated Fe–Ti–V oxide deposits, Sichuan Province, SW China. J. Petrol. 46, 2253–2280.